6. Time-Resolved Laser Spectroscopy

The investigation of fast processes, such as electron motions in atoms or molecules, radiative or collision-induced decays of excited levels, isomerization of excited molecules, or the relaxation of an optically pumped system toward thermal equilibrium, opens the way to study in detail the dynamic properties of excited atoms and molecules. A thorough knowledge of dynamical processes is of fundamental importance for many branches of physics, chemistry, or biology. Examples are predissociation rates of excited molecules, femtosecond chemistry, or the understanding of the visual process and its different steps from the photoexcitation of rhodopsin molecules in the retina cells to the arrival of electrical nerve pulses in the brain.

In order to study these processes experimentally, one needs a sufficiently good time resolution, which means that the resolvable minimum time interval Δt must still be shorter than the time scale T of the process under investigation. While the previous chapters emphasized the high *spectral* resolution, this chapter concentrates on experimental techniques that allow high *time* resolution.

The development of ultrashort laser pulses and of new detection techniques that allow a very high time resolution has brought about impressive progress in the study of fast processes. The achievable time resolution has been pushed recently into the attosecond range ($1\,\text{as} = 10^{-18}\,\text{s}$). Spectroscopists can now quantitatively follow up ultrafast processes, which could not be resolved ten years ago.

The *spectral* resolution $\Delta\nu$ of most time-resolved techniques is, in principle, confined by the Fourier limit $\Delta\nu = a/\Delta T$, where ΔT is the duration of the short light pulse and the factor $a \simeq 1$ depends on the profile $I(t)$ of the pulse. The spectral bandwidth $\Delta\nu$ of such *Fourier-limited pulses* is still much narrower than that of light pulses from incoherent light sources, such as flashlamps or sparks. Some time-resolved coherent methods based on regular trains of short pulses even circumvent the Fourier limit $\Delta\nu$ of a single pulse and simultaneously reach extremely high spectral and time resolutions (Sect. 7.4).

We will at first discuss techniques for the generation and detection of short laser pulses before their importance for different applications is demonstrated by some examples. Methods for measuring lifetimes of excited atoms or molecules and of fast relaxation phenomena are presented. These applications illustrate the relevance of pico- and femtosecond molecular physics and chemistry for our understanding of fundamental dynamical processes in molecules.

The special aspects of time-resolved coherent spectroscopy are covered in Sects. 7.2, 7.4. For a more extensive representation of the fas-

cinating field of time-resolved spectroscopy some monographs [6.1–6.4], reviews [6.5–6.8], and conference proceedings [6.9–6.11] should be mentioned.

6.1 Generation of Short Laser Pulses

For incoherent, pulsed light sources (for example, flashlamps or spark discharges) the duration of the light pulse is essentially determined by that of the electric discharge. For a long time, microsecond pulses represented the shortest available pulses. Only recently could the nanosecond range be reached by using special discharge circuits with low inductance and with pulse-forming networks [6.12, 6.13].

For laser pulses, on the other hand, the time duration of the pulse is not necessarily limited by the duration of the pump pulse, but may be much shorter. Before we present different techniques to achieve ultrashort laser pulses, we will discuss the relations between the relevant parameters of a laser that determine the time profile of a laser pulse.

6.1.1 Time Profiles of Pulsed Lasers

In active laser media pumped by pulsed sources (for example, flashlamps, electron pulses, or pulsed lasers), the population inversion necessary for oscillation threshold can be maintained only over a time interval ΔT that depends on the duration and power of the pump pulse. A schematic time diagram of a pump pulse, the population inversion, and the laser output is shown in Fig. 6.1. As soon as threshold is reached, laser emission starts. If the pump power is still increasing, the gain becomes high and the laser power rises faster than the inversion, until the increasingly induced emission reduces the inversion to the threshold value.

The time profile of the laser pulse is not only determined by the amplification per round trip $G(t)$ (Vol. 1, Sect. 5.2) but also by the relaxation times τ_i, τ_k of the upper and lower laser levels. If these times are short compared to the rise time of the pump pulse, quasi-stationary laser emission is reached, where the inversion $\Delta N(t)$ and the output power $P_L(t)$ have a smooth time profile, determined by the balance between pump power $P_p(t)$, which creates the inversion, and laser output power $P_L(t)$, which decreases it. Such a time behavior, which is depicted in Fig. 6.1a, can be found, for instance, in many pulsed gas lasers such as the excimer lasers (Vol. 1, Sect. 5.7).

In some pulsed lasers (for example, the N_2 laser) the lower laser level has a longer effective lifetime than the upper level [6.14]. The increasing laser power $P_L(t)$ decreases the population inversion by stimulated emission. Since the lower level is not sufficiently quickly depopulated, it forms a bottleneck for maintaining threshold inversion. The laser pulse itself limits its duration and it ends before the pump pulse ceases (self-terminating laser, Fig. 6.1b).

If the relaxation times τ_i, τ_k are long compared to the rise time of the pump pulse, a large inversion ΔN may build up before the induced emission

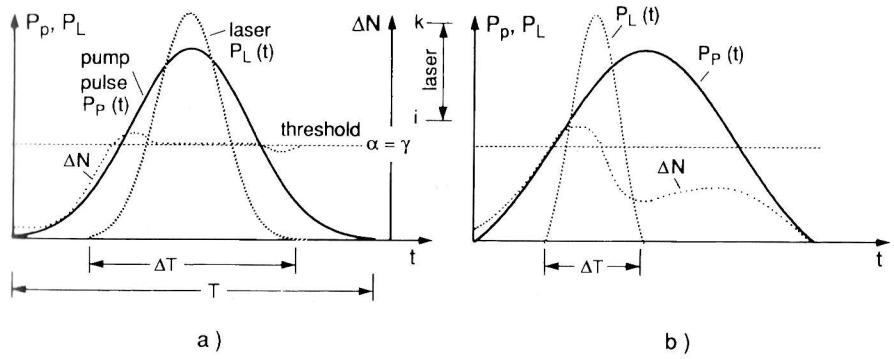

Fig. 6.1a,b. Time profiles of the pump power $P_p(t)$, the inversion density $\Delta N(t)$, and laser output power $P_L(t)$: (**a**) for sufficiently short lifetime τ_i of the lower laser level; and (**b**) for a self-terminating laser with $\tau_i^{\text{eff}} > \tau_k^{\text{eff}}$

is strong enough to deplete the upper level. The corresponding high gain leads to a large amplification of induced emission and the laser power P_L may become so high that it depletes the upper laser level faster than the pump can refill it. The inversion ΔN drops below threshold and the laser oscillation stops long before the pump pulse ends. When the pump has again built up a sufficiently large inversion, laser oscillations starts again. In this case, which is, for instance, realized in the flashlamp-pumped ruby laser, the laser output consists of a more or less irregular sequence of "spikes" (Fig. 6.2) with a duration of $\Delta T \simeq 1\,\mu s$ for each spike, which is much shorter than the pump–pulse duration $T \simeq 100\,\mu s$ to 1 ms [6.15, 6.16].

For time-resolved laser spectroscopy, pulsed dye lasers are of particular relevance due to their continuously tunable wavelength. They can be pumped by flashlamps ($T \simeq 1\,\mu s$ to 1 ms), by other pulsed lasers, for example, by copper-vapor lasers ($T \simeq 50$ ns), excimer lasers ($T \simeq 15$ ns), nitrogen lasers ($T = 2-10$ ns), or frequency-doubled Nd:YAG lasers ($T = 5-15$ ns). Because of the short relaxation times τ_i, $\tau_k (\simeq 10^{-11}\,s)$, no spiking occurs and the situation of Fig. 6.1a is realized (Vol. 1, Sect. 5.7). The dye laser pulses have durations between 1 ns to 500 μs, depending on the pump pulses; typical peak powers range from 1 kW to 10 MW and pulse repetition rates from 1 Hz to 15 kHz [6.17].

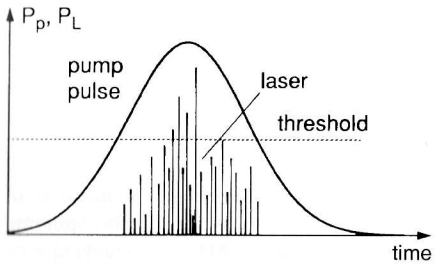

Fig. 6.2. Schematic representation of spikes in the emission of a flashlamp-pumped solid-state laser with long relaxation times τ_i, τ_k

6.1.2 Q-Switched Lasers

In order to obtain a single, powerful pulse of a flashlamp-pumped laser instead of the irregular sequence of many spikes, the technique of Q-switching was developed. Q-switching is based on the following principle:

Until a selected time t_0 after the start of the pump pulse at $t = 0$, the cavity losses of a laser are kept so high by a closed "optical switch" inside the laser resonator that the oscillation threshold cannot be reached. Therefore a large inversion ΔN is built up by the pump (Fig. 6.3). If the switch is opened at $t = t_0$ the losses are suddenly lowered (that is, the quality factor or Q-value of the cavity (Vol. 1, Sect. 5.1) jumps from a low to a high value). Because of the large amplification $G \propto B_{ik}\rho\Delta N$ for induced emission, a quickly rising intense laser pulse develops, which depletes in a very short time the whole inversion that had been built up during the time interval t_0. This converts the energy stored in the active medium into a giant light pulse [6.16, 6.18, 6.19]. The time profile of the pulse depends on the rise time of Q-switching. Typical durations of these giant pulses are 1–20 ns and peak powers up to 10^9 W are reached, which can be further increased by subsequent amplification stages.

Such an optical switch can be realized, for instance, if one of the resonator mirrors is mounted on a rapidly spinning motor shaft (Fig. 6.4). Only at that time t_0 where the surface normal of the mirror coincides with the resonator axis is the incident light reflected back into the resonator, giving a high Q-value of the laser cavity [6.20]. The optimum time t_0 can be selected by imaging the beam of a light-emitting diode (LED) after reflection at the spinning mirror onto the detector D, which provides the trigger signal for the flashlamp of the Q-switched laser. This technique, however, has some disadvantages: the spinning mirror is not very stable and the switching time is not sufficiently short. Therefore other Q-switching methods have been developed that are based on electro-optical or acousto-optical modulators [6.21].

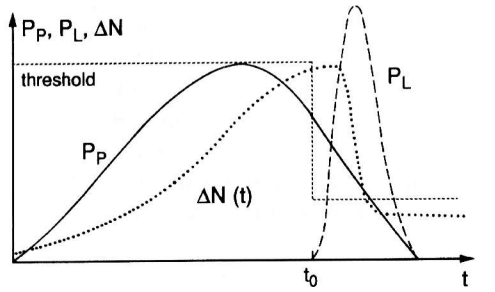

Fig. 6.3. Pump power $P_p(t)$, resonator losses $\gamma(t)$, inversion density $\Delta N(t)$, and laser output power $P_L(t)$ for a Q-switched laser

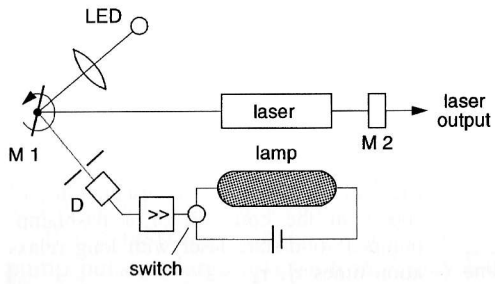

Fig. 6.4. Experimental realization of Q-switching by a rapidly spinning cavity mirror M1

One example is given in Fig. 6.5, where a Pockels cell between two crossed polarizers acts as a Q-switch [6.22]. The Pockels cell consists of an optically anisotropic crystal that turns the plane of polarization of a transmitted, linearly polarized wave by an angle $\theta \propto |E|$ when an external electric field $\boldsymbol{E}$ is applied. Since the transmittance of the system is $T = T_0(1 - \cos^2\theta)$, it can be changed by the voltage U applied to the electrodes of the Pockels cell. If for times $t < t_0$ the voltage is $U = 0$, the crossed polarizers have the transmittance $T = 0$ for $\theta = 0$. When at $t = t_0$ a fast voltage pulse $U(t)$ is applied to the Pockels cell, which causes a rotation of the polarization plane by $\theta = 90°$, the transmittance rises to its maximum value T_0. The linearly polarized lightwave can pass the switch, is reflected back and forth between the resonator mirrors M1 and M2, and is amplified until the inversion ΔN is depleted below threshold. The experimental arrangement shown in Fig. 6.5d works differently and needs only one polarizer P1, which is used as polarizing beam splitter. For $t < t_0$ a voltage U is kept at the Pockels cell, which causes circular polarization of the transmitted light. After reflection at M1 the light again passes the Pockels cell, reaches P1 as linearly polarized light with the plane of polarization turned by $\theta = 90°$, and is totally reflected by P1 and therefore lost for further amplification. For $t > t_0$ U is switched off, P1 now transmits, and the laser output is coupled out through M2.

The optimum choice of t_0 depends on the duration T of the pump pulse $P_p(t)$ and on the effective lifetime τ_k of the upper laser level. If $\tau_k \gg T \approx t_0$, only a small fraction of the energy stored in the upper laser

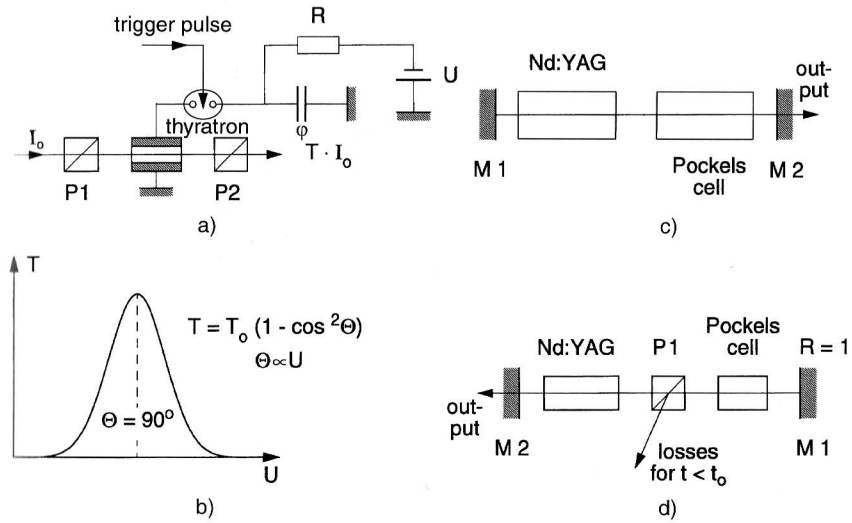

Fig. 6.5a–d. Q-switching with a Pockels cell inside the laser resonator: (**a**) Pockel's cell between two crossed polarizers, (**b**) transmission $T(\theta) \propto U$; (**c**),(**d**) possible experimental arrangements

level is lost by relaxation and the giant pulse can extract nearly the whole energy. For example, with the ruby laser ($\tau_k \approx 3$ ms) the switching time t_0 can be chosen close to the end of the pump pulse ($t_0 = 0.1-1$ ms), while for Nd:YAG-lasers ($\tau_k \approx 0.2$ ms) the optimum switching time t_0 lies before the end of the pump pulse. Therefore only part of the pump energy can be converted into the giant pulse [6.16, 6.19, 6.23].

6.1.3 Cavity Dumping

The principle of Q-switching can also be applied to cw lasers. Here, however, an inverse technique, called *cavity dumping*, is used. The laser cavity consists of highly reflecting mirrors in order to keep the losses low and the Q-value high. The intracavity cw power is therefore high because nearly no power leaks out of the resonator. At $t = t_0$ an optical switch is activated that couples a large fraction of this stored power out of the resonator. This may again be performed with a Pockels cell (Fig. 6.5d), where now M1 and M2 are highly reflecting, and P1 has a large transmittance for $t < t_0$, but reflects the light out of the cavity for a short time Δt at $t = t_0$.

Often an acousto-optic switch is used, for example, for argon lasers and cw dye lasers [6.24]. Its basic principle is explained in Fig. 6.6. A short ultrasonic pulse with acoustic frequency f_s and pulse duration $T \gg 1/f_s$ is sent at $t = t_0$ through a fused quartz plate inside the laser resonator. The acoustic wave produces a time-dependent spatially periodic modulation of the refractive index $n(t, z)$, which acts as a Bragg grating with the grating constant $\Lambda = c_s/f_s$, equal to the acoustic wavelength Λ where c_s is the sound velocity. When an optical wave $E_0 \cos(\omega t - \boldsymbol{k}\cdot\boldsymbol{r})$ with the wavelength $\lambda = 2\pi/k$ passes through the Bragg plate, the fraction η of the incident intensity I_0 is diffracted

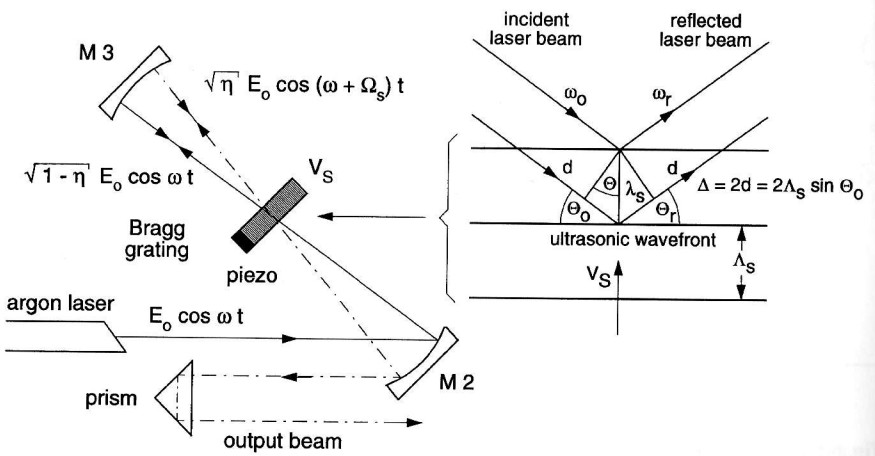

Fig. 6.6. Cavity dumping of a cw argon laser by a pulsed acoustic wave. The insert shows the Bragg reflection of an optical wave at a running ultrasonic wave with wavelength Λ_s

by an angle θ determined by the Bragg relation:

$$2\Lambda \sin\theta = \lambda/n \,. \tag{6.1}$$

The fraction η depends on the modulation amplitude of the refractive index and thus on the power of the ultrasonic wave.

When the optical wave is reflected at an acoustic wave front moving with the velocity v_s, its frequency ω suffers a Doppler shift, which is, according to (6.1) with $c = \lambda \cdot \omega/2\pi$ and $v_s = \Lambda\Omega/2\pi$

$$\Delta\omega = 2\frac{n v_s}{c}\omega \sin\theta = 2n\frac{\Lambda\Omega}{\lambda\omega}\omega \sin\theta = \Omega \,, \tag{6.2}$$

and turns out to be equal to the acoustic frequency $\Omega = 2\pi f_s$. The amplitude of the deflected fraction is $E_1 = \sqrt{\eta}E_0 \cos(\omega+\Omega)t$, that of the unaffected transmitted wave $E_2 = \sqrt{1-\eta}E_0 \cos\omega t$. After reflection at the mirror M3 the fraction $\sqrt{1-\eta}E_1$ is transmitted and the fraction $\sqrt{\eta}E_2$ is deflected by the Bragg plate into the direction of the outcoupled beam. This time, however, the reflection occurs at receding acoustic wavefronts and the Doppler shift is $-\Omega$ instead of $+\Omega$. The total amplitude of the extracted wave is therefore

$$\begin{aligned} E_c &= \sqrt{\eta}\sqrt{1-\eta}E_0[\cos(\omega+\Omega)t + \cos(\omega-\Omega)t] \\ &= 2\sqrt{\eta(1-\eta)}E_0 \cos\Omega t \cos\omega t \,. \end{aligned} \tag{6.3}$$

The average output power $P_c \propto E_c^2$ of the light pulse is then with $\omega \gg \Omega$ and $\langle\cos^2\omega t\rangle = 0.5$:

$$P_c(t) = \eta(t)[1-\eta(t)]P_0 \cos^2\Omega t \,, \tag{6.4}$$

where the time-dependent efficiency $\eta(t)$ is determined by the time profile of the ultrasonic pulse (Fig. 6.7) and P_0 is the intracavity power. During the ultrasonic pulse the fraction $2\eta(1-\eta)$ of the optical power $\frac{1}{2}\epsilon_0 E_0^2$, stored within the laser resonator, can be extracted in a short light pulse, which is still modulated at twice the acoustic frequency Ω. With $\eta = 0.3$ one obtains an extraction efficiency of $2\eta(1-\eta) = 0.42$.

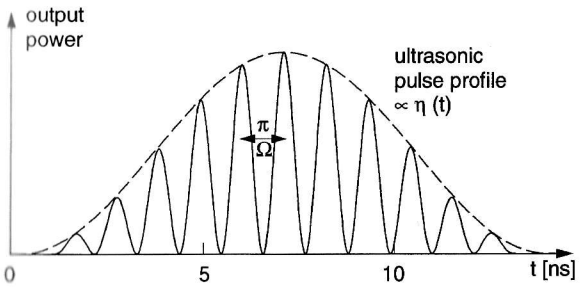

Fig. 6.7. Intensity profile of a cavity-dumped laser pulse, showing the intensity modulation at twice the ultrasonic frequency Ω

The repetition rate f of the extracted pulses can be varied within wide limits by choosing the appropriate repetition rate of the ultrasonic pulses. Above a critical frequency f_c, which varies for the different laser types, the peak power of the extracted pulses decreases if the time between two successive pulses is not sufficiently long to recover the inversion and to reach sufficient intracavity power.

The technique of cavity dumping is mainly applied to gas lasers and cw dye lasers. One achieves pulse durations $\Delta T = 10-100$ ns, pulse-repetition rates of 0–4 MHz, and peak powers that may be 10–100 times higher than for normal cw operation with optimized transmission of the output coupler. The average power depends on the repetition rate f. Typical values for $f = 10^4-4\times10^6$ Hz are 0.1–40% of the cw output power. The disadvantage of the acoustic cavity dumper compared to the Pockels cell of Fig. 6.5 is the intensity modulation of the pulse at the frequency 2Ω.

Example 6.1.

With an argon laser, which delivers 3-W cw power at $\lambda = 514.5$ nm, the cavity dumping yields a pulse duration $\Delta T = 10$ ns. At a repetition rate $f = 1$ MHz peak powers of 60 W are possible. The on/off ratio is then $f\Delta T = 10^{-2}$ and the average power $P \approx 0.6$ W is 20% of the cw power.

6.1.4 Mode Locking of Lasers

Without frequency-selective elements inside the laser resonator, the laser generally oscillates simultaneously on many resonator modes within the spectral gain profile of the active medium (Vol. 1, Sect. 5.3). In this "multimode operation" no definite phase relations exist between the different oscillating modes, and the laser output equals the sum $\sum_k I_k$ of the intensities I_k of all oscillating modes, which are more or less randomly fluctuating in time (Vol. 1, Sect. 5.3.4).

If coupling between the phases of these simultaneously oscillating modes can be established, a coherent superposition of the mode *amplitudes* may be reached, which leads to the generation of short output pulses in the picosecond range. This mode coupling or *mode locking* has been realized by optical modulators inside the laser resonator (*active* mode locking) or by saturable absorbers (*passive* mode locking) or by a combined action of both locking techniques [6.16, 6.25–6.29].

a) Active Mode Locking

When the intensity of a monochromatic lightwave

$$E = A_0 \cos(\omega_0 t - kx) ,$$

is modulated at the frequency $f = \Omega/2\pi$ (for example, by a Pockels cell or an acousto-optic modulator), the frequency spectrum of the optical wave contains, besides the carrier at $\omega = \omega_0$, sidebands at $\omega = \omega_0 \pm \Omega$ (that is, $\nu = \nu_0 \pm f$) (Fig. 6.8).

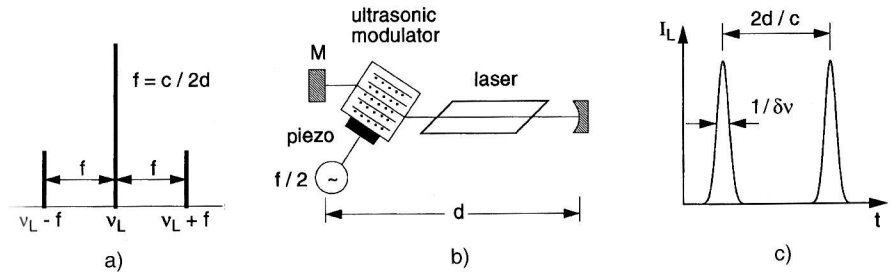

Fig. 6.8a–c. Active mode locking: (**a**) sideband generation; (**b**) experimental arrangement with a standing ultrasonic wave inside the laser resonator; (**c**) idealized output pulses

If the modulator is placed inside the laser resonator with the mirror separation d and the mode frequencies $\nu_m = \nu_0 \pm m \cdot c/2d$ ($m = 0, 1, 2, \ldots$), the sidebands coincide with resonator mode frequencies if the modulation frequency f equals the mode separation $\Delta\nu = c/2d$. The sidebands can then reach the oscillation threshold and participate in the laser oscillation. Since they pass the intracavity modulator they are also modulated and new sidebands $\nu = \nu_0 \pm 2f$ are generated. This continues until all modes inside the gain profile participate in the laser oscillation. There is, however, an important difference from normal multimode operation: the modes do not oscillate independently, but are phase-coupled by the modulator. At a certain time t_0, the amplitudes of all modes have their maximum at the location of the modulator and this situation is repeated after each cavity round-trip time $T = 2d/c$ (Fig. 6.8c). We will discuss this in more detail:

The modulator has the time-dependent transmission

$$T = T_0[1 - \delta(1 - \cos\Omega t)] = T_0[1 - 2\delta \sin^2(\Omega/2)t] , \tag{6.5}$$

with the modulation frequency $f = \Omega/2\pi$ and the modulation amplitude $2\delta \leq 1$. Behind the modulator the field amplitude A_k of the kth mode becomes

$$A_k(t) = TA_{k0} \cos\omega_k t = T_0 A_{k0}[1 - 2\delta \sin^2(\Omega/2)t] \cos\omega_k t . \tag{6.6}$$

This can be written with $\sin^2 x/2 = \frac{1}{2}(1 - \cos x)$ as

$$A_k(t) = T_0 A_{k0}\left[(1-\delta)\cos\omega_k t + \tfrac{1}{2}\delta[\cos(\omega_k + \Omega)t + \cos(\omega_k - \Omega)t]\right] . \tag{6.7}$$

For $\Omega = \pi c/d$, the sideband $\omega_k + \Omega$ corresponds to the next resonator mode and generates the amplitude

$$A_{k+1} = \tfrac{1}{2}A_0 T_0 \delta \cos\omega_{k+1} ,$$

which is further amplified by stimulated emission, as long as ω_{k+1} lies within the gain profile above threshold. Since the amplitudes of all three modes in (6.7) achieve their maxima at times $t = q2d/c$ ($q = 0, 1, 2, \ldots$), their phases are coupled by the modulation. A corresponding consideration applies to all other sidebands generated by modulation of the sidebands in (6.7).

Within the spectral width $\delta\nu$ of the gain profile

$$N = \frac{\delta\nu}{\Delta\nu} = 2\delta\nu\frac{d}{c} ,$$

oscillating resonator modes with the mode separation $\Delta\nu = c/2d$ can be locked together. The superposition of these N phase-locked modes results in the total amplitude

$$A(t) = \sum_{k=-m}^{+m} A_k \cos(\omega_0 + k\Omega)t , \quad \text{with} \quad N = 2m+1 . \tag{6.8}$$

For equal mode amplitudes $A_k = A_0$, (6.8) gives the total time-dependent intensity

$$I(t) \propto A_0^2 \frac{\sin^2(\frac{1}{2}N\Omega t)}{\sin^2(\frac{1}{2}\Omega t)} \cos^2\omega_0 t . \tag{6.9}$$

If the amplitude A_0 is time independent (cw laser), this represents a sequence of equidistant pulses with the separation

$$T = \frac{2d}{c} = \frac{1}{\Delta\nu} , \tag{6.10}$$

which equals the round-trip time through the laser resonator. The pulse width

$$\Delta T = \frac{2\pi}{(2m+1)\Omega} = \frac{2\pi}{N\Omega} = \frac{1}{\delta\nu} , \tag{6.11}$$

is determined by the number N of phase-locked modes and is inversely proportional to the spectral bandwidth $\delta\nu$ of the gain profile above threshold (Fig. 6.9).

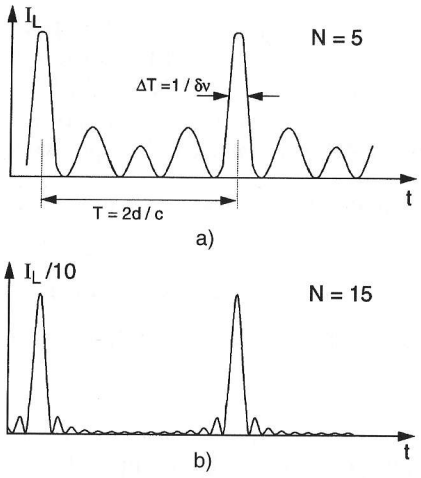

Fig. 6.9a,b. Schematic profile of the output of a mode-locked laser: (**a**) with 5 modes locked; (**b**) with 15 modes locked

The peak power of the pulses, which can be derived from the intensity maxima in (6.9) at times $t = 2\pi q/\Omega = q(2d/c)$ $(q = 0, 1, 2, \ldots)$, is proportional to N^2. The pulse energy is therefore proportional to $N^2\Delta T \propto N$. In between the main pulses $(N-2)$ small maxima appear, which decrease in intensity as N increases.

Note: For equal amplitudes $A_k = A_0$ the time-dependent intensity $I(t)$ in (6.9) corresponds exactly to the spatial intensity distribution $I(x)$ of light diffracted by a grating with N grooves that are illuminated by a plane wave. One has to replace Ωt by the phase difference ϕ between neighboring interfering partial waves, see (4.28) in Vol. 1, Sect. 4.1.3 and compare Figs. Vol. 1, 4.21 and 6.9.

In real mode-locked lasers the amplitudes A_k are generally not equal. Their amplitude distribution A_k depends on the form of the spectral gain profile. This modifies (6.9) and gives slightly different time profiles of the mode-locked pulses, but does not change the principle considerations.

For *pulsed* mode-locked lasers the envelope of the pulse heights follows the time profile $\Delta N(t)$ of the inversion, which is determined by the pump power $P_p(t)$. Instead of a continuous sequence of equal pulses one obtains a finite train of pulses (Fig. 6.10).

For many applications a single laser pulse instead of a train of pulses is required. This can be realized with a synchronously triggered Pockels cell outside the laser resonator, which transmits only one selected pulse out of the pulse train. It is triggered by a mode-locked pulse just before the maximum of the train envelope, then it opens for a time $\Delta t < 2d/c$ and transmits only the next pulse following the trigger pulse [6.30]. Another method of single-pulse selection is cavity dumping of a mode-locked laser [6.31]. Here the trigger signal for the intracavity Pockels cell (Fig. 6.5) is synchronized by the mode-locked pulses and couples just one mode-locked pulse out of the cavity (Fig. 6.10b).

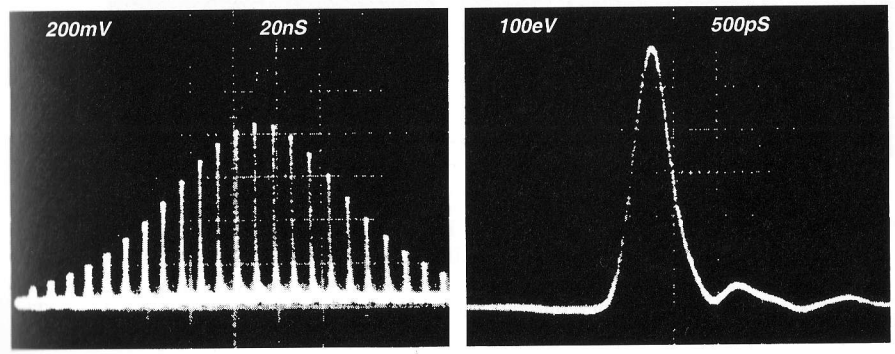

Fig. 6.10. (**a**) Pulse train of a mode-locked pulsed Nd:YAG laser; and (**b**) single pulse selected by a Pockel's cell. Note the different time scales in (a) (2 ns/div) and (b) (500 ps/div) [6.30]

Example 6.2.

(a) The Doppler-broadened gain profile of the HeNe laser at $\lambda = 633\,\text{nm}$ has the spectral bandwidth $\delta\nu \approx 1.5\,\text{GHz}$. Therefore, mode-locked pulses with durations down to $\Delta T \approx 500\,\text{ps}$ can be generated.

(b) Because of the higher temperature in the discharge of an argon-ion laser the bandwidth at $\lambda = 514.5\,\text{nm}$ is about $\delta\nu = 5-7\,\text{GHz}$ and one would expect pulses down to 150 ps. Experimentally, 200-ps pulses have been achieved. The apparently longer pulse width in Fig. 6.11 is limited by the time resolution of the detectors.

(c) The actively mode-locked Nd:glass laser [6.27, 6.28] delivers pulses at $\lambda = 1.06\,\mu\text{m}$ with durations down to 5 ps with high peak power ($\geq 10^{10}\,\text{W}$), which can be frequency doubled or tripled in nonlinear optical crystals with high conversion efficiency. This yields powerful short light pulses in the green or ultraviolet region.

(d) Because of the large bandwidth $\delta\nu$ of their spectral gain profile, dye lasers, Ti:sapphire, and color-center lasers (Sect. 5.7) are the best candidates for generating ultrashort light pulses. With $\delta\nu = 3 \times 10^{13}\,\text{Hz}$ (this corresponds to $\delta\lambda \sim 30\,\text{nm}$ at $\lambda = 600\,\text{nm}$), pulse widths down to $\Delta T = 3 \times 10^{-14}\,\text{s}$ should be possible. This can, indeed, be realized with special techniques (Sect. 6.1.5). With active mode locking, however, one only reaches $\Delta T \geq 10-50\,\text{ps}$ [6.29]. This corresponds to the transit time of a light pulse through the modulator, which imposes a lower limit, unless new techniques are used.

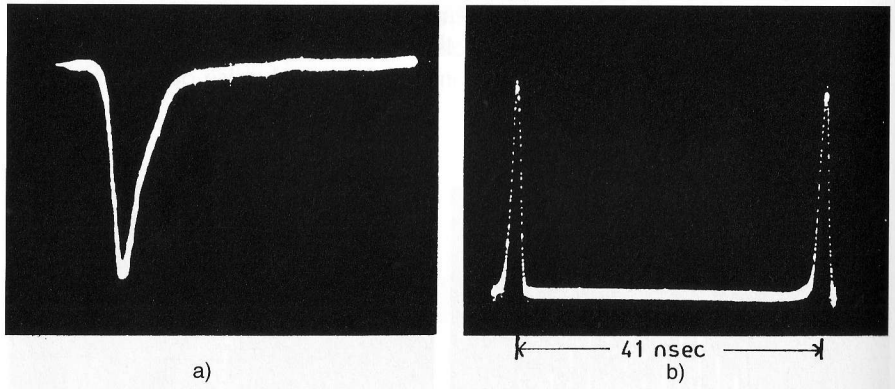

Fig. 6.11a,b. Measured pulses of a mode-locked argon laser at $\lambda = 488\,\text{nm}$: (**a**) monitored with a fast photodiode and a sampling oscilloscope (500 ps/div). The small oscillations after the pulse are cable reflections. (**b**) The attenuated scattered laser light was detected by a photomultiplier (single-photon counting) and stored in a multichannel analyzer. The time resolution is limited by the pulse rise times of the photodiode and photomultiplier, respectively [6.32]

b) Passive Mode Locking

Passive mode locking is a technique that demands less experimental effort than active mode-locking; it can be applied to pulsed as well as to cw lasers. Pulse widths below 1 ps have been realized. Its basic principles can be understood as follows:

Instead of the active modulator, a saturable absorber is put inside the laser resonator, close to one of the end mirrors (Fig. 6.12). The absorbing transition $|k\rangle \leftarrow |i\rangle$ takes place between the levels $|i\rangle$ and $|k\rangle$ with short relaxation times τ_i, τ_k. In order to reach oscillation threshold in spite of the absorption losses the gain of the active medium must be correspondingly high. In the case of a pulsed pump source, the emission of the active laser medium at a time shortly before threshold is reached consists of fluorescence photons, which are amplified by induced emission. The peak power of the resulting photon avalanches (Vol. 1, Sect. 5.2) fluctuates more or less randomly. Because of nonlinear saturation in the absorber (Sect. 2.1), the most intense photon avalanche suffers the lowest absorption losses and thus experiences the largest net gain. It therefore grows faster than other competing weaker avalanches, saturates the absorber more, and increases its net gain even more. After a few resonator round trips this photon pulse has become so powerful

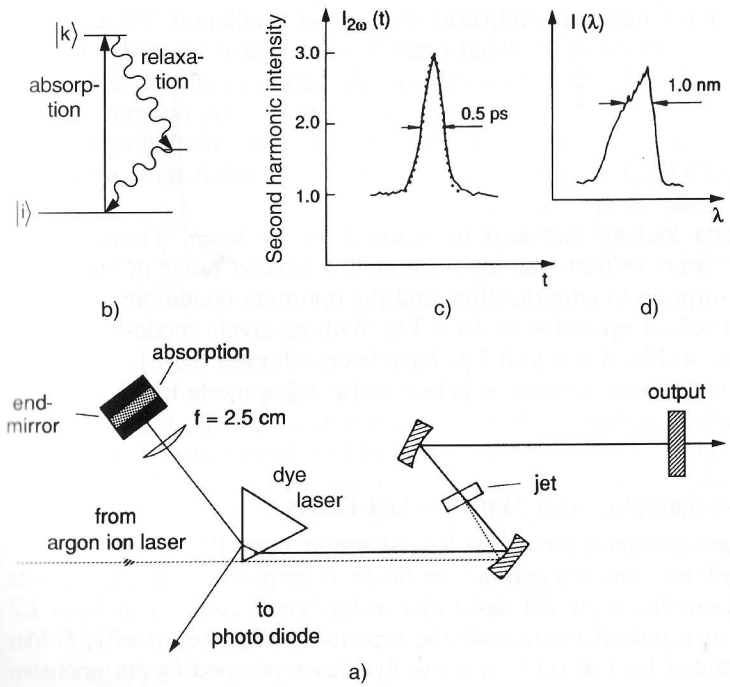

Fig. 6.12a–d. Passive mode locking of a cw dye laser: (**a**) experimental arrangement; (**b**) level scheme of absorber; (**c**) time profile; and (**d**) spectral profile of a mode-locked pulse [6.28]

that it depletes the inversion of the active laser medium nearly completely and therefore suppresses all other avalanches.

This nonlinear interaction of photons with the absorbing and the amplifying media leads under favorable conditions to mode-locked laser operation starting from a statistically fluctuating, unstable threshold situation. After this short unstable transient state the laser emission consists of a stable, regular train of short pulses with the time separation $T = 2d/c$, as long as the pump power remains above threshold (which is now lower than at the beginning because the absorption is saturated).

This more qualitative representation illustrates that the time profile and the width ΔT of the pulses is determined by the relaxation times of absorber and amplifier. In order to suppress the weaker photon avalanches reliably, the relaxation times of the absorber must be short compared with the resonator round-trip time. Otherwise, weak pulses, which pass the absorber shortly after the stronger saturating pulse, would take advantage of the saturation and would experience smaller losses. The recovery time of the amplifying transition in the active laser medium, on the other hand, should be comparable to the round-trip time in order to give maximum amplification of the strongest pulse, but minimum gain for pulses in between. A more thorough analysis of the conditions for stable passive mode locking can be found in [6.16, 6.33, 6.34].

The Fourier analysis of the regular pulse train yields again the mode spectrum of all resonator modes participating in the laser oscillation. The coupling of the modes is achieved at the fixed times $t = t_0 + q2d/c$ when the saturating pulse passes the absorber. This explains the term *passive mode locking*. Different dyes can be employed as saturable absorbers. The optimum choice depends on the wavelength. Examples are methylene blue, diethyloxadicarbocyanine iodide DODCI, or polymethinpyrylin [6.35], which have relaxation times of 10^{-9}–10^{-11} s.

Passive mode locking can also be realized in cw lasers. However, the smaller amplification restricts stable operation to a smaller range of values for the ratio of absorption to amplification, and the optimum conditions are more critical than in pulsed operation [6.36, 6.37]. With passively mode-locked cw dye lasers pulse widths down to 0.5 ps have been achieved [6.38].

More detailed representations of active and passive mode locking can be found in [6.16, 6.39, 6.40].

c) Synchronous Pumping with Mode-Locked Lasers

For synchronous pumping the mode-locked pump laser L1, which delivers short pulses with the time separation $T = 2d_1/c$, is employed to pump another laser L2 (for example, a cw dye laser or a color-center laser). This laser L2 then operates in a pulsed mode with the repetition frequency $f = 1/T$. An example, illustrated by Fig. 6.13, is a cw dye laser pumped by an acousto-optically mode-locked argon laser.

The optimum gain for the dye-laser pulses is achieved if they arrive in the active medium (dye jet) at the time of maximum inversion $\Delta N(t)$ (Fig. 6.14).

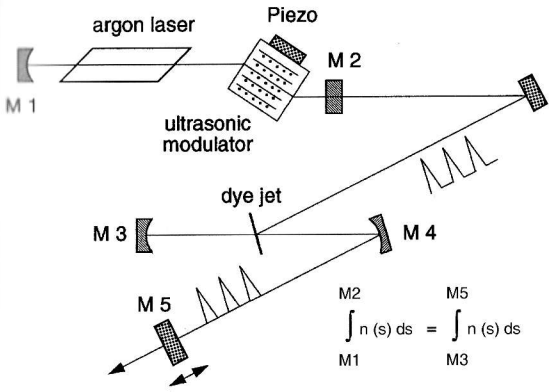

Fig. 6.13. Synchronously pumped cw dye laser

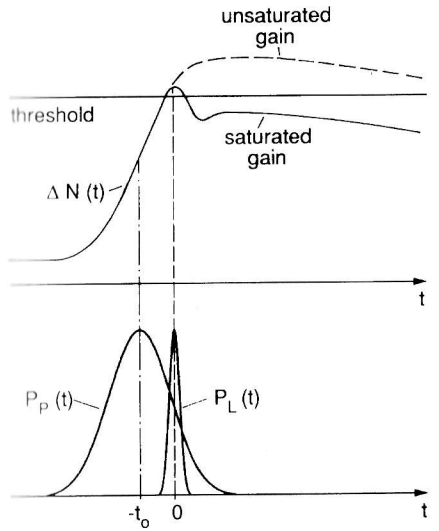

Fig. 6.14. Schematic time profiles of argon laser pump pulse $P_p(t)$, inversion $\Delta N(t)$ in the dye jet, and dye laser pulse $P_L(t)$ in a synchronously pumped cw dye laser

If the optical cavity length d_2 of the dye laser is properly matched to the length d_1 of the pump laser resonator, the round-trip times of the pulses in both lasers become equal and the arrival times of the two pulses in the amplifying dye jet are synchronized. Because of saturation effects, the dye-laser pulses become much shorter than the pump pulses, and pulse widths below 1 ps have been achieved [6.41–6.43]. For the experimental realization of accurate synchronization one end mirror of the dye-laser cavity is placed on a micrometer carriage in order to adjust the length d_2. The achievable pulse width ΔT depends on the accuracy $\Delta d = d_1 - d_2$ of the optical cavity length matching. A mismatch of $\Delta d = 1\,\mu$m increases the pulsewidth from 0.5 to 1 ps [6.44].

For many applications the pulse repetition rate $f = c/2d$ (which is $f = 150$ MHz for $d = 1$ m) is too high. In such cases the combination of syn-

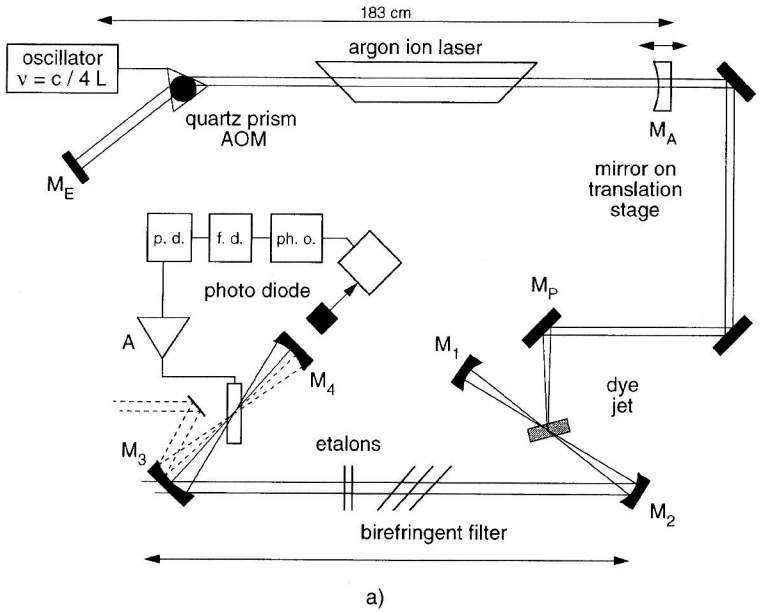

Fig. 6.15a,b. Cavity-dumped synchronously pumped dye laser system with synchronization electronics [Courtesy Spectra-Physics]: (**a**) experimental setup; (**b**) correct synchronization time of a mode-locked pulse with the time of maximum output coupling of the cavity dumping pulse

chronous pumping and cavity dumping (Sect. 6.1.2) is helpful, where only every kth pulse ($k \geq 10$) is extracted due to Bragg reflection by an ultrasonic pulsed wave in the cavity dumper. The ultrasonic pulse now has to be synchronized with the mode-locked optical pulses in order to assure that the ultrasonic pulse is applied just at the time when the mode-locked pulse passes the cavity dumper (Fig. 6.15b).

The technical realization of this synchronized system is shown in Fig. 6.15a. The frequency $\nu_s = \Omega/2\pi$ of the ultrasonic wave is chosen as an integer multiple $\nu_s = q \cdot c/2d$ of the mode-locking frequency. A fast photodiode, which detects the mode-locked optical pulses, provides the trigger signal for the RF generator for the ultrasonic wave. This allows the adjustment of the phase of the ultrasonic wave in such a way that the arrival time of the mode-locked pulse in the cavity dumper coincides with its maximum extraction efficiency. During the ultrasonic pulse only one mode-locked pulse is extracted. The extraction repetition frequency $\nu_e = (c/2d)/k$ can be chosen between 1 Hz to 4 MHz by selecting the repetition rate of the ultrasonic pulses [6.45].

Table 6.1. Summary of different mode-locking techniques. With active mode locking of cw lasers an average power of 1 W can be achieved

Technique	Mode locker	Laser	Typical pulse duration	Typical pulse energy
Active mode locking	Acousto-optic modulator	Argon, cw	300 ps	10 nJ
		HeNe, cw	500 ps	0.1 nJ
	Pockels cell	Nd:YAG, pulsed	100 ps	10 μJ
Passive mode locking	Saturable absorber	Dye, cw	1 ps	1 nJ
		Nd:YAG	1–10 ps	1 nJ
Synchronous pumping	Mode-locked pump laser and matching of resonator length	Dye, cw	1 ps	10 nJ
		Color center	1 ps	10 nJ
colliding pulse mode locking CPM	Passive mode locking and eventual synchronous pumping	Ring dye laser	< 100 fs	≈ 1 nJ
Kerr lens mode locking	optical Kerr effect	Ti:sapphire	< 10 fs	≈ 1–10 nJ

There are several versions of the experimental realizations of mode-locked or synchronously pumped lasers. Table 6.1 gives a short summary of typical operation parameters of the different techniques. More detailed representations of this subject can be found in [6.39–6.46].

6.1.5 Generation of Femtosecond Pulses

In the last sections it was shown that passive mode locking or synchronous pumping allows the generation of light pulses with a pulse width below 1 ps. Recently some new techniques have been developed that generate still shorter pulses. The shortest light pulses reported up to now are only 5-fs long [6.120]. At $\lambda = 600$ nm this corresponds to less than 3 oscillation periods of visible light! Generation of higher harmonics of such short pulses produces even shorter pulses in the VUV with pulsewidths of around 100 attoseconds (0.1 fs). We will now discuss some of these new techniques.

a) The Colliding Pulse Mode-Locked Laser

A cw ring dye laser pumped by an argon laser can be passively mode locked by an absorber inside the ring resonator. The mode-locked dye laser pulses travel into both directions in the ring, clockwise and counterclockwise (Fig. 6.16). If the absorber, realized by a thin dye jet, is placed at a location where the path length A1–A2 between the amplifying jet and the absorbing jet is just one-quarter of the total ring length L, the net gain per round-trip is maximum when the counterpropagating pulses collide within the absorber. This can be seen as follows:

For this situation the time separation $\Delta t = T/2$ between the passage of successive pulses (one clockwise and the next counter-clockwise) through the amplifier achieves the maximum value of one-half of the round-trip time T. This means that the amplifying medium has a maximum time to recover its inversion after it was depleted by the previous pulse.

The total pulse intensity in the absorber where the two pulses collide is twice that of a single pulse. This means larger saturation and less absorption. Both effects lead to a maximum net gain if the two pulses collide in the absorber jet.

At a proper choice of the amplifying gain and the absorption losses, this situation will automatically be realized in the passively mode-locked ring dye laser. It leads to an energetically favorable stable operation, which is called *colliding-pulse mode* (CPM) *locking*, and the whole system is termed a *CPM laser*. This mode of operation results in particularly short pulses down to 50 fs. There are several reasons for this pulse shortening:

(i) The transit time of the light pulses through the thin absorber jet ($d < 100\,\mu m$) is only about 400 fs. During their superposition in the absorber the two colliding light pulses form, for a short time, a standing wave, which generates, because of saturation effects, a spatial modulation $N_i(z)$ of the absorber density N_i and a corresponding refractive index grating with a period of $\lambda/2$ (Fig. 6.17). This grating causes a partial reflection of the two incident light pulses. The reflected part of one pulse superimposes and interferes with the oppositely traveling pulse, resulting in a coupling of the two pulses. At $t = t_0$ the constructive interference is maximized (additive-pulse mode locking)

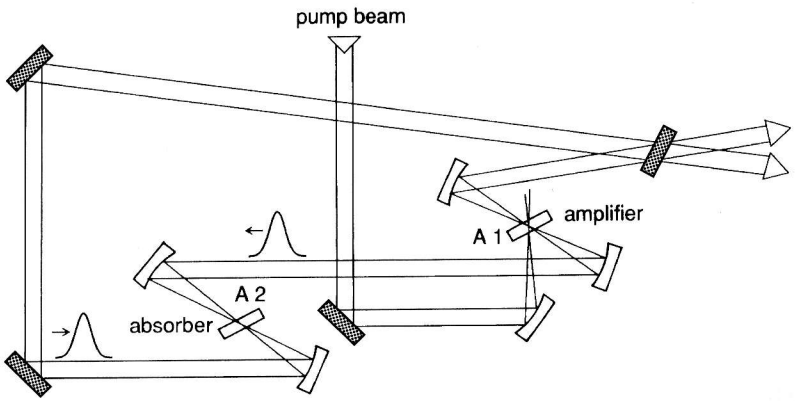

Fig. 6.16. CPM ring dye laser. The distance A1–A2 is one-quarter the total round-trip length L

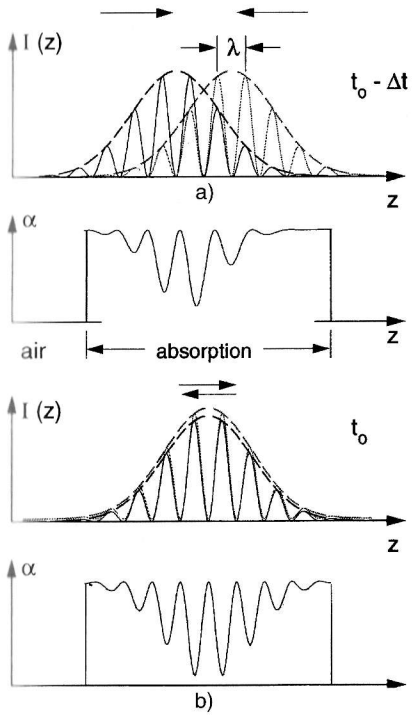

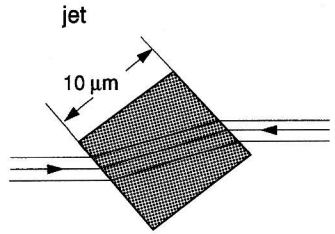

Fig. 6.17a,b. Density grating generated in the absorber jet by the colliding optical pulses at two different times: (**a**) partial overlap at time $t_0 - \Delta t$; (**b**) complete overlap at $t = t_0$

(ii) The absorption of both pulses has a minimum when the two pulse maxima just overlap. At this time the grating is most pronounced and the coupling is maximized. The pulses are therefore shortened for each successive round-trip until the shortening is compensated by other phenomena, which cause a broadening of the pulses. One of these effects is the dispersion due to the dielectric layers on the resonator mirrors, which causes a different round-trip time for the different wavelengths contained in the short pulse. The shorter the pulses the broader their spectral profile $I(\lambda)$ becomes and the more serious are dispersion effects.

The mirror dispersion can be compensated up to the first order by inserting into the ring resonator (Fig. 6.18) dispersive prisms, which introduce different optical path lengths $d_p n(\lambda)$ [6.48]. This dispersion compensation can be optimized by shifting the prisms perpendicularly to the pulse propagation, thus adjusting the optical path length $d_p n(\lambda)$ of the pulses through the prisms.

In principle, the lower limit ΔT_{min} of the pulse width is given by the Fourier limit $\Delta T_{min} = a/\delta\nu$, where $a \sim 1$ is a constant that depends on the

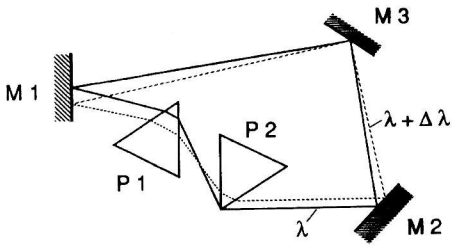

Fig. 6.18. Compensation of mirror dispersion by prisms within the cavity

time profile of the pulse (Sect. 6.2.2). The larger the spectral width $\delta\nu$ of the gain profile is, the smaller $\Delta T_{\min}$ becomes. In reality, however, the dispersion effects, which increase with $\delta\nu$, become more and more important and prevent reaching the principal lower limit of $\Delta T_{\min}$. In Fig. 6.19 the achievable limit $\Delta T_{\min}$ is plotted against the spectral bandwidth for different dispersions [fs/cm], where the dashed curve gives the dispersion-free Fourier limit of the pulse width ΔT [6.48, 6.49].

Pulse widths below 100 fs can be reached with this CMP technique [6.50, 6.51]. If the CPM ring dye laser is synchronously pumped by a mode-locked argon laser stable operation over many hours can be realized [6.52]. Using a novel combination of saturable absorber dyes and a frequency-doubled mode-locked Nd:YAG laser as a pump, pulse widths down to 39 ps at $\lambda = 815$ nm have been reported [6.53].

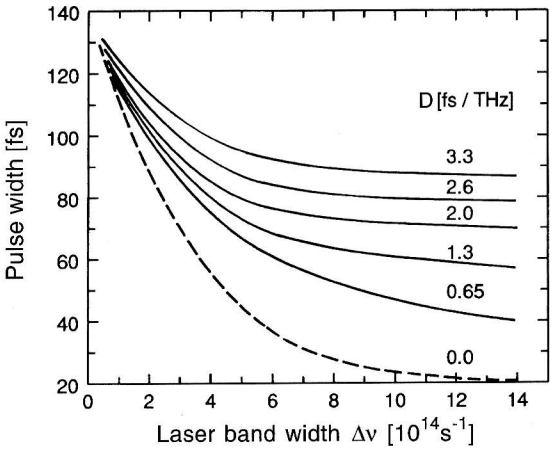

Fig. 6.19. Theoretical lower limit of pulse width ΔT as a function of the spectral bandwidth $\Delta\nu$ of a mode-locked laser for different values of the dispersion parameter D [fs/THz] [6.120]

b) Kerr Lens Mode Locking

For a long time dye solutions were the favorite gain medium for the generation of femtosecond pulses because of their broad spectral gain region.

Meanwhile, different solid state gain materials have been found with very broad fluorescence bandwidths, which allow, in combination with new nonlinear phenomena, the realization of light pulses down to 5 fs.

For solid-state lasers typical lifetimes of the upper laser level range from 10^{-6} s to 10^{-3} s. This is much longer than the time between successive pulses in a mode-locked pulse train, which is about 10–20 ns. Therefore the saturation of the amplifying medium cannot recover within the time between two pulses and the amplifying medium therefore cannot contribute to the mode locking by dynamic saturation as in the case of CPM mode locking discussed before. One needs a fast saturable absorber, where the saturation can follow the short pulse profile of the mode-locked pulses. Such passively mode-locked solid-state lasers might not be completely stable with regard to pulse stability and pulse intensities and they generally do not deliver pulses below 1 ps.

The crucial breakthrough for the realization of ultrafast pulses below 100 fs was the discovery of a fast pulse-forming mechanism in 1991, called *Kerr lens mode locking* (KLM), which can be understood as follows:

For large incident intensities I the refractive index n of a medium depends on the intensity. One can write

$$n(\omega, I) = n_0(\omega) + n_2(\omega) I \,.$$

This intensity-dependent change of the refractive index is caused by the nonlinear polarization of the electron shell induced by the electric field of the optical wave and is therefore called the optical Kerr effect.

Because of the radial intensity variation of a Gaussian laser beam, the refractive index of the medium under the influence of a laser beam shows a radial gradient with the maximum value of n at the central axis. This acts as a focusing lens and leads to focusing of the incident laser beam, where the focal length depends on the intensity. Since the central part of the pulse time-

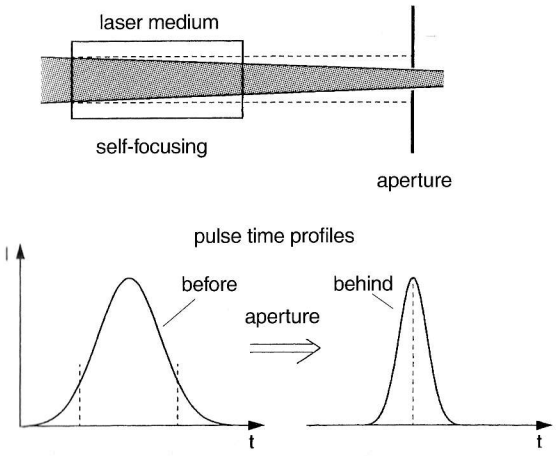

Fig. 6.20. Kerr lens mode locking

profile has the largest intensiy, it is also focused more strongly than the outer parts, where the intensity is lower. A circular aperture at the right place inside the laser resonator transmits only this central part, that is, it cuts away the leading and trailing edges and the transmitted pulse is therefore shorter than the incident pulse (Fig. 6.20).

Example 6.3.
For sapphire Al_2O_3 $n_2 = 3\times10^{-16}\,cm^2/W$. At the intensity of $10^{14}\,W/cm^2$ the refractive index changes by $\Delta n = 3\times10^{-2}\,n_0$. For a wave with $\lambda = 1000\,nm$ this leads to a phase shift of $\Delta\Phi = (2\pi/\lambda)\Delta n = 300\cdot 2\pi$ after a pathlength of 1 cm, which results in a radius of curvature of the phase-front $R = 4\,cm$ with the corresponding focal length of the Kerr lens.

Often the laser medium itself acts as Kerr medium and forms an additional lens inside the laser resonator. This is shown schematically in Fig. 6.21, where the lenses with focal lengths f_1 and f_2 are in practice curved mirrors [6.54]. Without the Kerr lens the resonator is stable if the distance between the two lenses is $f_1 + f_2$. With the Kerr lens this distance has to be modified to $f_1 + f_2 + \delta$, where the quantity δ depends on the focal length of the Kerr lens, and therefore on the pulse intensity. If the distance between the two lenses is $f_1 + f_2 + \delta$ the resonator is only stable for values of δ within the limits

$$0 < \delta < \delta_1\,, \quad \text{or} \quad \delta_2 < \delta < \delta_1 + \delta_2\,,$$

where

$$\delta_1 = \frac{f_2^2}{d_2 - f_2}\,, \quad \delta_2 = \frac{f_1^2}{d_1 - f_1} \tag{6.12}$$

Choosing the right value of δ makes the resonator stable only for the time interval around the pulse maximum.

In Fig. 6.22 the experimental setup for a femtosecond Ti:sapphire laser with Kerr lens mode locking is shown, where the amplifying laser medium acts simultaneously as a Kerr lens. The folded resonator is designed in such

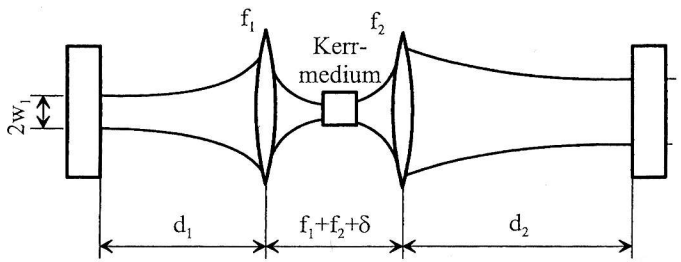

Fig. 6.21. Schematic illustration of Kerr lens mode locking inside the laser resonator [6.54]

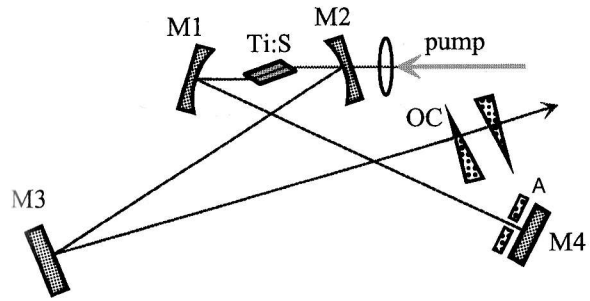

Fig. 6.22. Schematic diagram of the MDC Ti:sapphire oscillator used for soft-aperture and hard-aperture mode locking [6.54]

a way that only the most intense part of the pulse is sufficiently focused by the Kerr lens to always pass for every round-trip through the spatially confined active region pumped by the argon-ion laser. Here the active gain medium defined by the pump focus acts as spatial "soft aperture." A mechanical aperture A in front of mirror M4 in Fig. 6.22 realizes "hard aperture" Kerr lens mode locking. Output pulses with pulsewidths below 10 fs have been demonstrated with this design.

A Kerr-lens mode-locked Ti:Sapphire laser with a threshold that is ten times less than in conventional Kerr-lens lasers has been reported by Fujimoto and his group [6.54]. The schematic diagram of this design with an astigmatically compensated folded cavity is shown in Fig. 6.23. The dispersion of the cavity is compensated by a prism pair and the output coupler has a transmission of 1%. The low threshold permits the use of low-power inexpensive pump lasers.

An alternative method for the realization of KLM uses the birefringent properties of the Kerr medium, which turns the plane of polarization of the light wave passing through the Kerr medium. This is illustrated in Fig. 6.24. The incident wave passes through a linear polarizer and is then elliptically polarized by a $\lambda/4$-plate. The Kerr medium causes a time dependent nonlin-

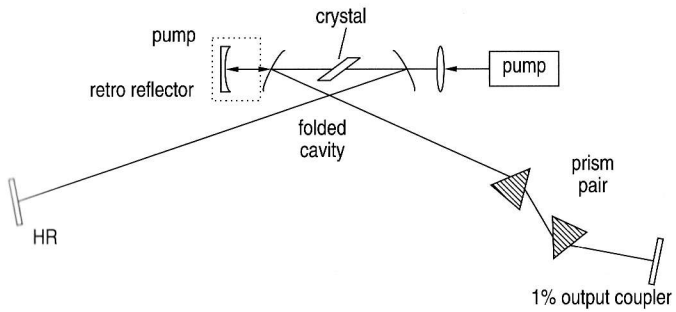

Fig. 6.23. Schematic diagram of the ultralow-threshold Ti:Al_2O_3 laser with Kerr-lens mode-locking [6.55]

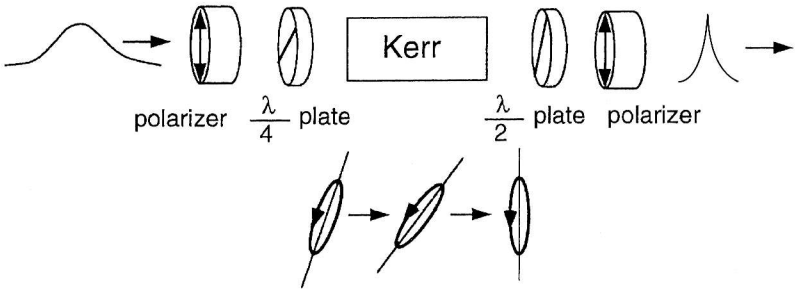

Fig. 6.24. Polarization-additive pulse mode-locking [6.56]

ear polarization rotation. A $\lambda/2$-plate and a linear polarizer behind the Kerr medium can be arranged in such a way that the pulse transmission reaches its maximum at the peak of the incident pulse, thus shortening the pulse width [6.56]. This device acts similarly to a passive saturable absorber and is particularly useful for fiber lasers with ultrashort pulses.

6.1.6 Optical Pulse Compression

Since the principle lower limit $\Delta T_{\min} = 1/\delta\nu$ of the optical pulse is given by the spectral bandwidth $\delta\nu$ of the gain medium, it is desirable to make $\delta\nu$ as large as possible. The idea of spectral broadening of optical pulses by *self-phase modulation* in optical fibers with subsequent pulse compression represented a breakthrough for achieving pulsewidths of only a few femtoseconds. The method is based on the following principle:

When an optical pulse with the spectral amplitude distribution $E(\omega)$ propagates through a medium with refractive index $n(\omega)$, its time profile will change because the group velocity

$$v_g = \frac{d\omega}{dk} = \frac{d}{dk}(v_{ph}k) = v_{ph} + k\frac{dv_{ph}}{dk}\,, \tag{6.13}$$

which gives the velocity of the pulse maximum, shows a dispersion

$$\frac{dv_g}{d\omega} = \frac{dv_g}{dk}\Big/\frac{d\omega}{dk} = \frac{1}{v_g}\frac{d^2\omega}{dk^2}\,. \tag{6.14}$$

For $d^2\omega/dk^2 \neq 0$, the velocity differs for the different frequency components of the pulse, which means that the shape of the pulse will change during its propagation through the medium (GVD = group velocity dispersion) (Fig. 6.25a). For negative dispersion ($dn/d\lambda < 0$), for example, the red wavelengths have a larger velocity than the blue ones, that is, the pulse becomes spatially broader.

If the optical pulse of a mode-locked laser is focused into an optical fiber, the intensity I becomes very high. The amplitude of the forced oscillations

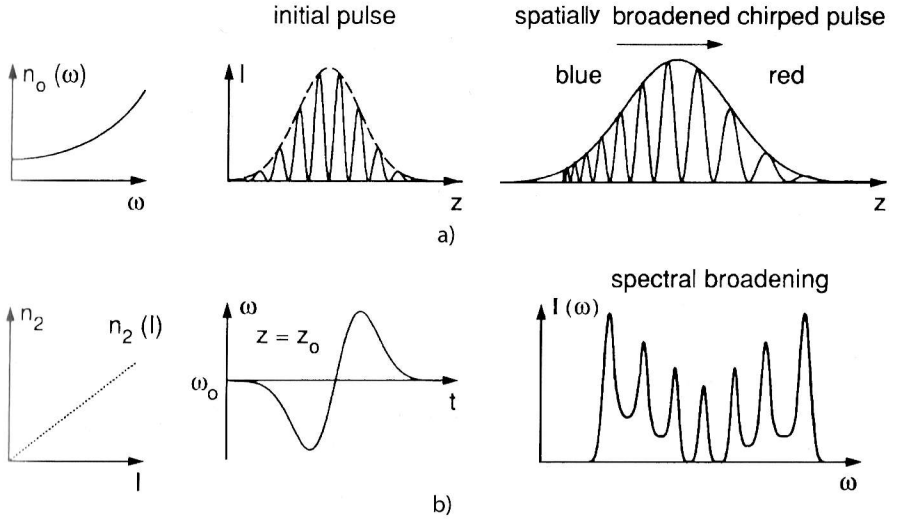

Fig. 6.25a,b. Spatial and spectral broadening of a pulse in a medium with normal linear (**a**) and nonlinear (**b**) refractive index

of the electrons in the fiber material under the influence of the optical field increases with the field amplitude and the refractive index becomes intensity dependent:

$$n(\omega, I) = n_0(\omega) + n_2 I(t)\,, \tag{6.15}$$

where $n_0(\omega)$ describes the linear dispersion (see Sect. 6.1.5). The phase $\phi = \omega t - kz$ of the optical wave $E = E_0\cos(\omega t - kz)$ with $k = n\omega/c$

$$\phi = \omega t - \omega n\frac{z}{c} = \omega\left(t - n_0\frac{z}{c}\right) - AI(t)\,, \quad \text{with} \quad A = n_2\omega\frac{z}{c}\,, \tag{6.16}$$

now depends on the intensity

$$I(t) = c\epsilon_0\int |E_0(\omega, t)|^2\cos^2(\omega t - kz)\,d\omega\,. \tag{6.17}$$

Since the momentary optical frequency

$$\omega = \frac{d\phi}{dt} = \omega_0 - A\frac{dI}{dt}\,, \tag{6.18}$$

is a function of the time derivative dI/dt, (6.18) illustrates that the frequency decreases at the leading edge of the pulse ($dI/dt > 0$), while at the trailing edge ($dI/dt < 0$) ω increases (*self-phase modulation*). The leading edge is red shifted, the trailing edge blue shifted. This frequency shift during the pulse time τ is called "chirp". The *spectral profile* of the pulse becomes broader (Fig. 6.25b).

The linear dispersion $n_0(\lambda)$ causes a *spatial* broadening, the intensity-dependent refractive index $n_2 I(t)$ a *spectral* broadening. The spatial broadening of the pulse (which corresponds to a broadening of its time profile) is proportional to the length of the fiber and depends on the spectral width $\Delta\omega$ of the pulse and on its intensity.

A quantitative description starts from the wave equation for the pulse envelope [6.57, 6.58]

$$\frac{\partial E}{\partial z}+\frac{1}{v_g}\frac{\partial E}{\partial t}+\frac{i}{2v_g^2}\frac{\partial v_g}{\partial \omega}\frac{\partial^2 E}{\partial t^2}=0\,, \tag{6.19}$$

which can be derived from the general wave equation with the slowly varying envelope approximation ($\lambda\partial^2 E/\partial z^2 \ll \partial E/\partial z$) [6.16].

For a pulse of initial width τ, which propagates with the group velocity v_g through a medium of length L, the solution of (6.19) yields the pulse width [6.59]

$$\tau' = \tau\sqrt{1+(\tau_c/\tau)^4}\,, \quad \text{with} \quad \tau_c = \sqrt{\frac{8L}{v_g^2}\cdot\frac{\partial v_g}{\partial\omega}}\,. \tag{6.20}$$

For $\tau = \tau_c$, the initial pulse width τ increases by a factor $\sqrt{2}$. Pulses that are shorter than the critical pulse width τ_c become broader. After the length

$$L = \sqrt{\frac{3}{2}}\frac{(\tau\cdot v_g/2)^2}{\partial v_g/\partial\omega}\,, \tag{6.21}$$

the pulse width has doubled. The relative pulse broadening sharply increases with decreasing width τ of the incident pulse.

The compression of this spectrally and spatially broadened pulse can now be achieved by a grating pair with the separation D that has a larger pathlength for red wavelengths than for blue ones and therefore delays the leading red edge of the pulse compared to its blue trailing edge. This can be seen as follows [6.60]: the optical pathlength $S(\lambda)$ between two phase-fronts of a plane wave before and after the grating is, according to Fig. 6.26

$$S(\lambda) = S_1 + S_2 = \frac{D}{\cos\beta}(1+\sin\gamma)\,, \quad \text{with} \quad \gamma = 90^\circ - (\alpha+\beta). \tag{6.22}$$

This transforms with $\cos(\alpha+\beta) = \cos\alpha\cos\beta - \sin\alpha\sin\beta$ into

$$S(\lambda) = D\left[\frac{1}{\cos\beta}+\cos\alpha-\sin\alpha\tan\beta\right].$$

With the grating equation $d(\sin\alpha-\sin\beta)=\lambda$ of a grating with groove separation d and its dispersion $\mathrm{d}\beta/\mathrm{d}\lambda = 1/(d\cos\beta)$ for a given angle of incidence α (Sect. 4.1.3), we obtain the spatial dispersion

$$\frac{\mathrm{d}S}{\mathrm{d}\lambda} = \frac{\mathrm{d}S}{\mathrm{d}\beta}\frac{\mathrm{d}\beta}{\mathrm{d}\lambda} = \frac{-D\lambda}{d^2\cos^3\beta} = \frac{-D\lambda}{d^2[1-(\lambda/d-\sin\alpha)^2]^{3/2}}\,. \tag{6.23}$$

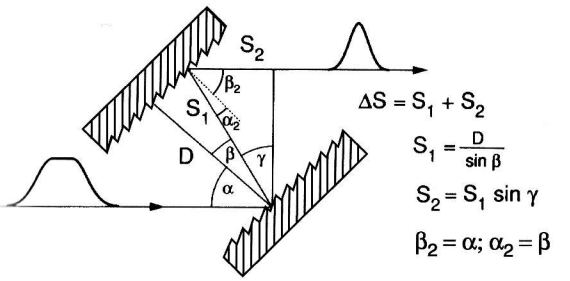

Fig. 6.26. Pulse compression by a grating pair

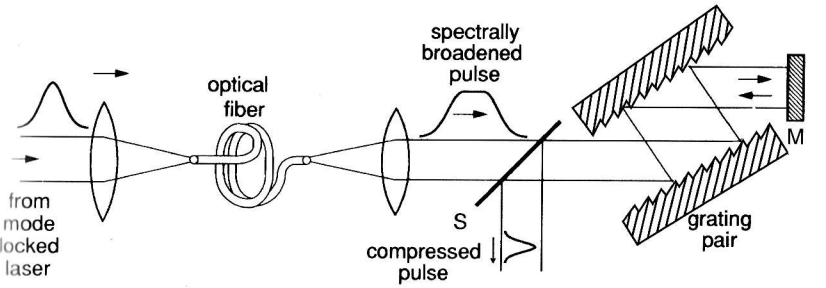

Fig. 6.27. Experimental arrangement for the generation of femtosecond pulses by self-phase-modulation with subsequent pulse compression by a grating pair [6.61]

This shows that the dispersion is proportional to the grating separation D and increases with λ. By choosing the correct value of D one can just compensate the chirp of the pulse generated in the optical fiber and obtain a compressed pulse.

A typical experimental arrangement is depicted in Fig. 6.27 [6.61]. The optical pulse from the mode-locked laser is spatially and spectrally broadened in the optical fiber and then compressed by the grating pair. The dispersion of the grating pair can be doubled if the pulse is reflected by the mirror M and passes the grating pair again. Pulse widths of 16 fs have been obtained with such a system [6.62].

With a combination of prisms and gratings (Fig. 6.28) not only the quadratic but also the cubic term in the phase dispersion

$$\phi(\omega) = \phi(\omega_0) + \left(\frac{\partial\phi}{\partial\omega}\right)_{\omega_0}(\omega-\omega_0) + \frac{1}{2}\left(\frac{\partial^2\phi}{\partial\omega^2}\right)_{\omega_0}(\omega-\omega_0)^2 + \frac{1}{6}\left(\frac{\partial^3\phi}{\partial\omega^3}\right)_{\omega_0}(\omega-\omega_0)^3\,, \tag{6.24}$$

can be compensated [6.63]. This allows one to reach pulsewidths of 6 fs.

More information and a detailed discussion of the different compression techniques can be found in [6.64].

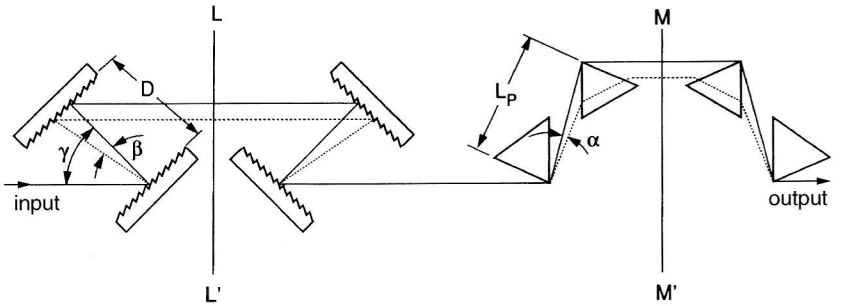

Fig. 6.28. Sequence of grating pairs and prism pairs for the compensation of quadratic and cubic phase dispersion. LL′ and MM′ are two phase-fronts. The solid line represents a reference path and the dashed line illustrates the paths for the wave of wavelength λ, which is diffracted by an angle β at the first grating and refracted by an angle α against the reference path in a prism [6.63]

6.1.7 Sub 10-fs Pulses with Chirped Laser Mirrors

The development of broadband saturable semiconductor absorber mirrors and of dispersion-engineered chirped multilayer dielectric mirrors has allowed the realization of self-starting ultrashort laser pulses, which routinely reach sub-10-fs pulsewidths and peak powers above the megawatt level.

Femtosecond pulse generation relies on a net negative intracavity group-delay dispersion (GDD). Since solid-state gain media introduce a frequency-dependent positive dispersion, this must be overcompensated by media inside the laser cavity that have a correspondingly large negative dispersion. We saw in Sect. 6.1.5 that intracavity prisms can be used as such compensators. However, here the GDD shows a large wavelength dependence and for very short pulses (with a corresponding broad spectral range) this results in asymmetric pulse shapes with broad pedestals in the time domain. The invention of chirped dielectric low-loss laser mirrors has brought a substantial improvement [6.65].

A chirped mirror is a dielectric mirror with many alternate layers with low and high indices of refraction. The reflectivity r at each boundary is $r = (n_r - n_l)/(n_r + n_l)$. If the optical thicknesses of these layers are always the same, we have the Bragg reflector shown in Fig. 6.29a. Such a mirror will, however, not generate a chirp in the reflected pulse. To achieve such a chirp the thicknesses of the layers must slowly vary from the first to the last layer, as shown in Fig. 6.29b. Two different wavelengths within the spectral bandwidth of the pulse now penetrate different path lengths into the stack and therefore suffer a different delay (positive group delay dispersion). When they are superimposed again after reflection, the reflected pulse has become broader because of the chirp. Proper engineering of the chirped mirror allows good compensation of the negative group dispersion of the laser cavity. In the mirror in Fig. 6.29a only the Bragg wavelength is linearly chirped. For the double-chirped mirror in Fig. 6.29b, the spectral width for which dispersion compensation can

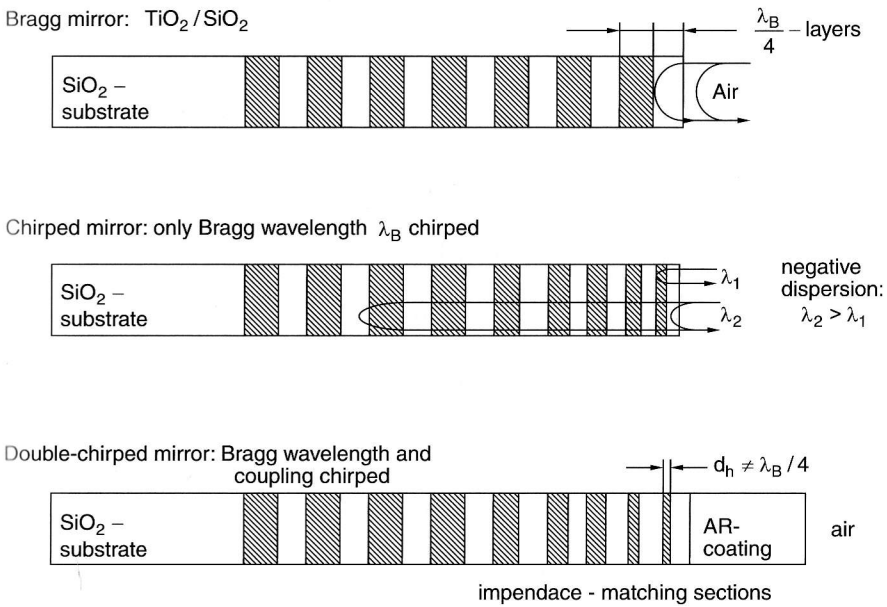

Fig. 6.29a–c. Chirped mirrors: (**a**) Bragg mirror with no chirp; (**b**) simple chirped mirror for one wavelength; (**c**) double-chirped mirror with matching sections to avoid residual reflections [6.68]

be reached is greatly increased. This also means that very short pulses can be properly chirped. In order to avoid undesired reflections from the front surface or from sections inside the mirror that cause oscillations in the group dispersion, an antireflection coating and matching sections between the Bragg layers are necessary [6.68].

Instead of varying the thicknesses of the layers, one can also produce chirped mirrors by smoothly altering the indices of refraction and the difference between them $(n_r - n_l)$ (Fig. 6.30).

These mirrors may be regarded as one-dimensional holograms that are generated when a chirped and an unchirped laser pulse from opposite directions are superimposed in a medium where they generate a refractive index pattern proportional to their total intensity [6.66]. When a chirped pulse is reflected by such a hologram, it becomes compressed, similar to the situation with phase-conjugated mirrors.

In practice, such mirrors are produced by evaporation techniques controlled by a corresponding computer program. In Fig. 6.30 the variation of the refractive index for the different dielectric layers is shown for a mirror with negative GDD, and in Fig. 6.31 the reflectivity and the group delay is plotted as a function of wavelength for mirrors with negatively and positively chirped graded-index profiles. In combination with Kerr lens mode locking such chirped mirrors allow the generation of femosecond pulses down to 4 fs [6.54].

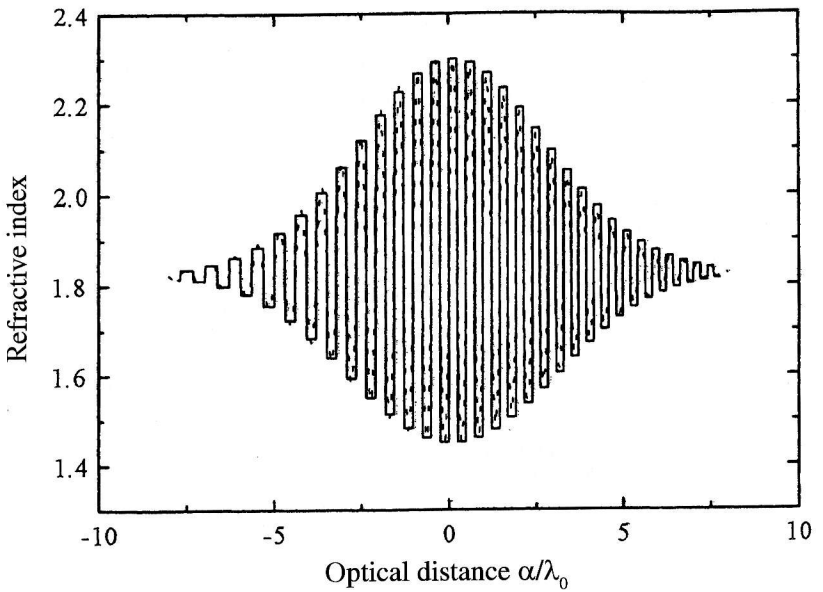

Fig. 6.30. Refractive index profile of a discrete-valued chirped dielectric mirror

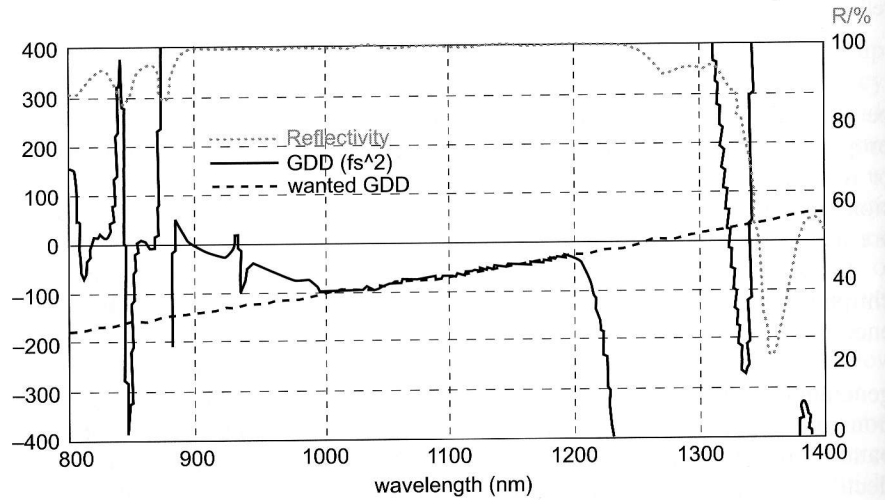

Fig. 6.31. Reflectivity R, realized GDD and wanted GDD as a function of λ for a chirped mirror [6.66b]

Another alternative for the generation of ultrafast pulses is the passive mode locking by fast semiconductor saturable absorbers in front of chirped mirrors (Fig. 6.31) in combination with Kerr lens mode locking [6.67]. The recovery time of the saturable absorber must be generally faster then the laser pulse width. This is provided by KLM, which may be regarded as artificial

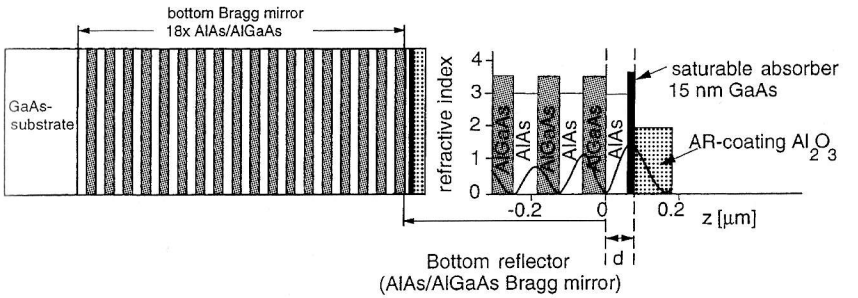

Fig. 6.32. Semiconductor Bragg mirror with a 15-nm saturable absorber layer of GaAs [6.67]

saturable absorber that is as fast as the Kerr nonlinearity following the laser intensity. Since the recovery time in a semiconductor material is given by the relaxation of the excited electrons into the initial state in the valence band, these materials represent fast saturable absorbers in the sub-picosecond range, but do not reach the 10-fs limit. Nevertheless, soliton-like pulses down to 13 fs have been achieved.

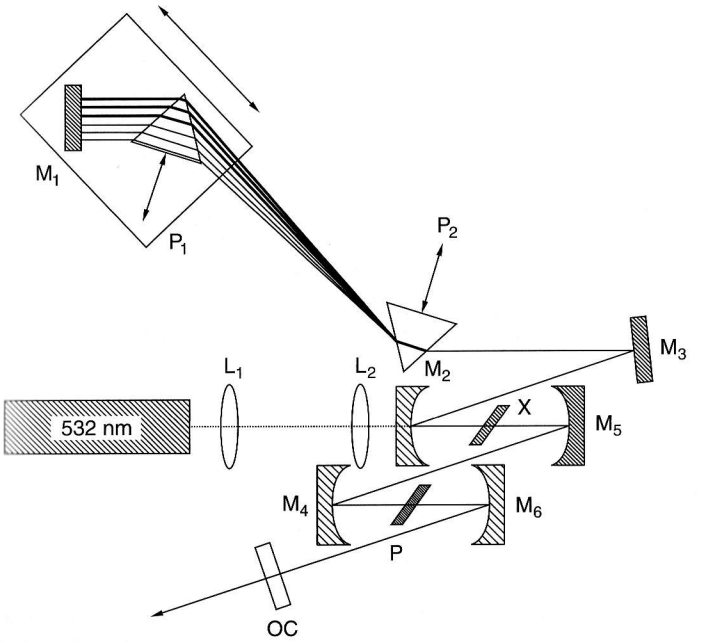

Fig. 6.33. Setup of the double-Z cavity for an ultrashort pulse Ti:sapphire laser. The two prisms P_1 and P_2 and eight bounces on double-chirped mirrors M_2–M_6 provide flat dispersion. A second focus in a BK7-plate (P) leads to enhanced SPM, and the laser generates significantly wider spectra [6.68]

A combination of saturable semiconductor media in front of a chirped mirror and KLM techniques can be used for reliable operation of sub-10-fs pulses.

A possible setup for generating the shortest pulses without pulse compression is shown in Fig. 6.33. It consists of five chirped mirrors M_2–M_6 and two prisms P_1, P_2. This setup provides a flat dispersion by the mirrors and dispersion compensation by the prisms. The curved mirrors focus the pump beam into the laser crystal X. The glass plate P in the second focus causes self-phase modulation which results in a significantly wider spectrum of the laser emission and thus a shorter pulse [6.68].

6.1.8 Fiber Lasers and Optical Solitons

In the Sect. 6.1.7 we discussed the self-phase modulation of an optical pulse in a fiber because of the intensity-dependent refractive index $n = n_0 + n_2 I(t)$. While the resultant spectral broadening of the pulse leads in a medium with normal negative dispersion ($dn_0/d\lambda < 0$) to a spatial broadening of the pulse, an anomalous linear dispersion ($dn_0/d\lambda > 0$) would result in a pulse compression. Such anomalous dispersion can be found in fused quartz fibers for $\lambda > 1.3\,\mu m$ [6.69, 6.70]. For a suitable choice of the pulse intensity the dispersion effects caused by $n_0(\lambda)$ and by $n_2 I(t)$ may cancel, which means that the pulse propagates through the medium without changing its time profile. Such a pulse is named a fundamental soliton [6.71, 6.72].

Introducing the refractive index $n = n_0 + n_2 I$ into the wave equation (6.19) yields stable solutions that are called *solitons* of order N. While the fundamental soliton ($N = 1$) has a constant time profile $I(t)$, the higher-order solitons show an oscillatory change of their time profile $I(t)$: the pulsewidth decreases at first and then increases again. After a path length z_0, which depends on the refractive index of the fiber and on the pulse intensity, the soliton recovers its initial form $I(t)$ [6.73, 6.74].

Optical solitons in fused quartz fibers can be utilized to achieve stable femtosecond pulses in broadband infrared lasers, such as the color-center laser or the Ti:sapphire laser. Such a system is called a *soliton laser* [6.75–6.82]. Its experimental realization is shown in Fig. 6.34.

A KCl:T1° color-center laser with end mirrors M_0 and M_1 is synchronously pumped by a mode-locked Nd:YAG laser. The output pulses of the color-center laser at $\lambda = 1.5\,nm$ pass the beam splitter S. A fraction of the intensity is reflected by S and is focused into an optical fiber where the pulses propagate as solitons, because the dispersion of the fiber at $1.5\,\mu m$ is $dn/d\lambda > 0$. The pulses are compressed, are reflected by M5, pass the fiber again, and are coupled back into the laser resonator. If the length of the fiber is adjusted properly, the transit time along the path M^0–S–M_5–S–M_0 just equals the round-trip time $T = 2d/c$ through the laser resonator M_0–M_1–M_0. In this case compressed pulses are always injected into the laser resonator at the proper times $t = t_0 + q2d/c$ ($q = 1, 2, \ldots$) to superimpose the pulses circulating inside the laser cavity. This injection of shortened pulses leads to

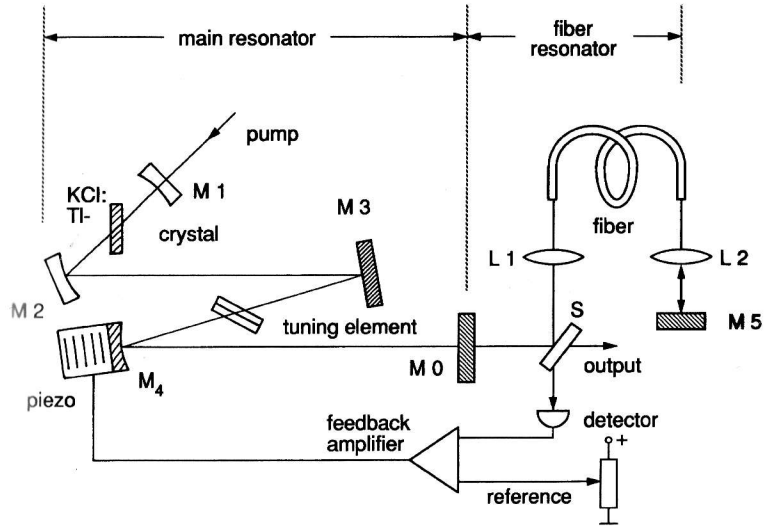

Fig. 6.34. Soliton laser [6.82]

a decrease of the laser pulse width until other broadening mechanisms, which increase with decreasing pulse width, compensate the pulse shortening.

In order to match the phase of the reflected fiber light pulse to that of the cavity internal pulse, the two resonator path lengths have to be equal within a small fraction of a wavelength. The output power, transmitted through S to the detector, critically depends on the proper matching of both cavity lengths and can therefore be used as feedback control for stabilizing the length of the laser resonator, which is controlled by the position of M4 mounted on a piezo cylinder. It turns out that the best stabilization can be achieved with solitons of order $N \geq 2$ [6.76].

With such a KCl:T1° color-center soliton laser, stable operation with pulse widths of 19 fs was demonstrated [6.81]. This corresponds at $\lambda = 1.5\,\mu m$ to only four oscillation periods of the infrared wave. More about soliton lasers can be found in [6.75–6.83].

The fabrication of rare-earth-doped optical fibers with a wide bandwidth gain have pushed the development of optical fiber amplifiers. This large bandwidth together with the low pump power requirements facilitated the realization of passively mode-locked femtosecond fiber lasers. The advantages of such fiber lasers are their compact setup with highly integrated optical components, their reliability, and their prealignment, which makes their daily operation more convenient [6.78].

The basic principle of a fiber ring laser is schematically shown in Fig. 6.35. The pump laser is coupled into the fiber ring laser through a fiber splice and the output power is extracted through a second splice. The fiber ring consists of negative ($-\beta_2$) and positive ($+\beta_2$) dispersion parts with an erbium amplifying medium where the dispersion can be controlled by small concentrations of dopants. The isolator enforces unidirectional operation and fiber loops pre-

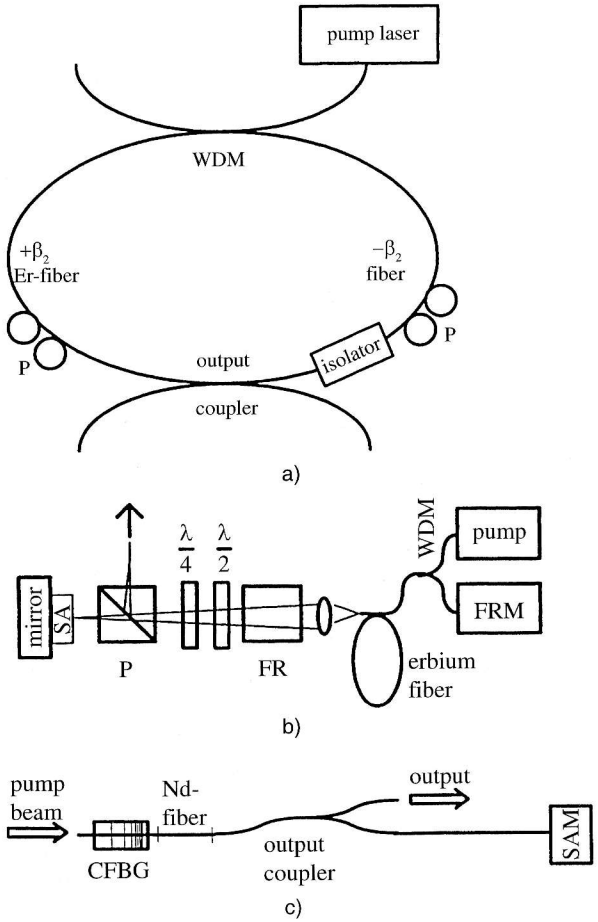

Fig. 6.35. (**a**) Basic principle of fiber ring laser with positive and negative dispersion parts of the fiber; (**b**) linear fiber laser (FR, Faraday rotator; FRM, Faraday rotator minor; SA, saturable absorber); (**c**) fully integrated passively mode-locked Nd-fiber laser (CFBG, chirped fiber Bragg grating for dispersion compensation; SAM, saturable absorber minor) [6.78]

serve the polarization state. Instead of ring fiber lasers, linear fiber lasers have also been realized, as shown in Fig. 6.35b. The saturable absorber in front of the end mirror allows passive mode locking and results in femtosecond operation. An example of a fully integrated fiber femtosecond laser is given in Fig. 6.35c, where the saturable absorber is butted directly to a fiber end, and a chirped fiber Bragg grating (CFBG) is used for dispersion compensation.

Output pulses with about 70-μJ pulse energy and pulse widths below 100 fs have been generated with such fiber lasers [6.79].

Soliton ring fiber lasers can be also realized with active mode locking by polarization modulation [6.80], or by additive-pulse mode locking (APM). In

the latter technique the pulse is split into the two arms of an interferometer and the coherent superposition of the self-phase modulated pulses results in pulse shortening [6.56].

The tuning range of an erbium soliton laser could be greatly enlarged by Raman shifting [6.84]. Such a system, which delivers 170 fs bandwidth-limited pulses with pulse energies of 24 pJ, could be tuned from 1000 nm to 1070 nm. After amplification in an erbium fiber amplifier, output pulses with 74 fs width and 8 nJ could be obtained. Frequency-doubling in a periodically poled lithium-niobate crystal shifts the infrared soliton laser wavelength into the visible range [6.85].

6.1.9 Wavelength-Tunable Ultrashort Pulses

Up to now we have only discussed femtosecond lasers that can deliver short pulses with a fixed wavelength. For time-resolved spectroscopy the tunability of the wavelength provides many advantages, and so much effort has been expended in the development of sources of ultrashort pulses with a wide tuning range. There are several ways to realize them.

Similar to cw lasers, active media with a broad spectral gain profile can be used for pulsed lasers. With wavelength-selective optical elements inside the laser resonator, the laser wavelength can be tuned across the whole gain profile. However, the drawback is the widening of the pulse length ΔT with decreasing spectral width $\Delta\nu$ due to the principal Fourier limit $\Delta T > 2\pi/\Delta\nu$.

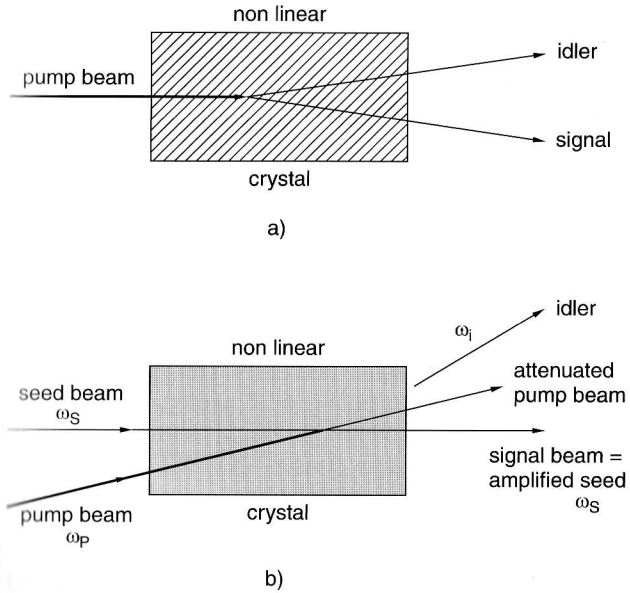

Fig. 6.36a,b. Schematic diagram of parametric oscillator (**a**) and (**b**) noncollinear optical parametric amplifier NOPA

Therefore, a new principle was developed for the generation of ultrashort tunable pulses which is based on parametric oscillators and amplifiers (see Vol. 1, Sect. 5.8.8).

In the parametric oscillator (Fig. 6.36a), a pump photon $\hbar\omega_p$ is split in a nonlinear optical crystal into a signal photon $\hbar\omega_s$ and an idler photon $\hbar\omega_i$, such that energy and momentum are conserved:

$$\omega_p = \omega_s + \omega_i \tag{6.25a}$$

$$\boldsymbol{k}_p = \boldsymbol{k}_s + \boldsymbol{k}_i \,. \tag{6.25b}$$

In the parametric amplifier two laser beams are focused into the nonlinear optical crystal: the seed laser beam with frequency ω_s and a strong pump beam with ω_p. Due to the parametric process in the nonlinear crystal, a new wave is generated with a difference frequency $\omega_i = \omega_p - \omega_s$ (Fig. 6.36b). Most of the pump photons split up into a signal and an idler photon where the signal photons superimpose the seed photons and amplify the weak seed beam.

There are important differences with the amplification in media with inverted populations, where the gain depends on the time interval in which the inversion can be maintained. For conventional laser pulse amplification, the width of the amplified pulse therefore depends on the width of the pump pulse (see Fig. 6.1), although the time profile of the amplified pulse does not necessarily follow that of the pump pulse. For parametric amplification, on the other hand, there is no population inversion in the gain medium. The amplification is due to the nonlinear interaction between pump and seed pulses, and the time profile of the amplified seed pulse is the convolution of the seed pulse and pump pulse profiles.

In order to ensure that this superposition is always in phase, the *phase velocities* of the interacting waves have to be matched. This corresponds exactly to the phase-matching condition for the frequency doubling in nonlinear crystals and is equivalent to momentum conservation (6.25b) for the interacting photons. This condition can be realized in birefringent crystals. However, there is an additional condition: if the three short pulses are to have maximum overlap during their passage through the crystal and therefore an optimum interaction, their *group velocities* must also be matched. This cannot generally be achieved for the collinear propagation of seed and pump beams in birefringent crystals. With a group velocity mismatch, the amplified signal pulse becomes broader and the amplification factor decreases from its optimum value. The noncollinear arrangement shown in Fig. 6.37, called NOPA (noncollinear optical parametric amplifier), solves this problem. With the angle ψ between the pump and seed beams, momentum conservation (6.25b) gives for the angle Ω between signal and idler beams the relation

$$\Omega = \psi(1 + \lambda_i/\lambda_s) \,. \tag{6.26}$$

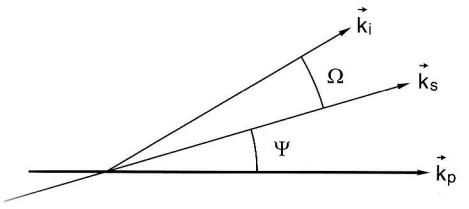

$$v_g^{\text{signal}} = \cos\Omega \cdot v_g^{\text{idler}}; \quad \Omega = \Psi\left(1 + \frac{\lambda_i}{\lambda_s}\right)$$

Fig. 6.37. Group-velocity matching in a noncollinear optical parametric amplifier (NOPA)

For a properly chosen value of ψ, the group velocities

$$v_g^{\text{idler}} = \cos\Omega \cdot v_g^{\text{signal}} = \cos(\psi + \psi\lambda_i/\lambda_s) v_g^{\text{signal}} \tag{6.27}$$

of idler and signal waves in the selected direction become equal. The phase-matching condition for the phase velocities can be fulfilled by choosing the proper angle with respect to the optical axis of the nonlinear crystal.

Wavelength tuning over a larger spectral range can be achieved in the following way (Fig. 6.38).

A small part of the pump beam at λ_p is focused into a CaF_2 plate, where it generates a spectral continuum in the focus. Most of the pump beam is frequency doubled in a nonlinear crystal. The continuum emission from this small bright spot in the CaF_2 plate is collected by a parabolic mirror and im-

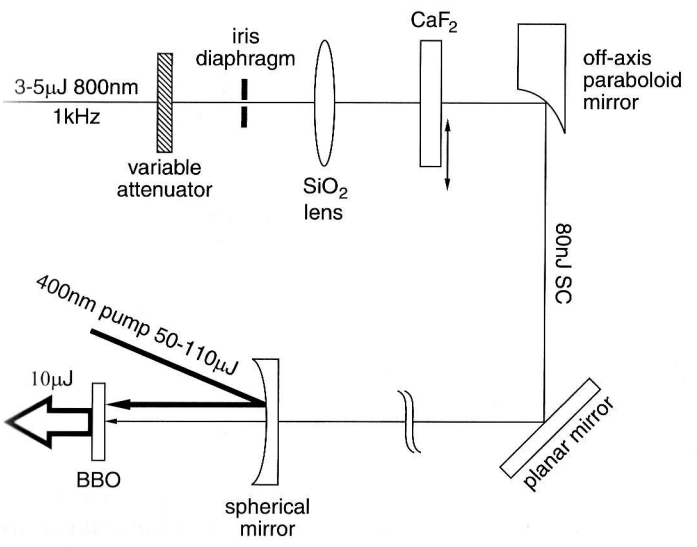

Fig. 6.38. Tunable optical parametric amplifier with a white light source and a blue pump laser [6.85]

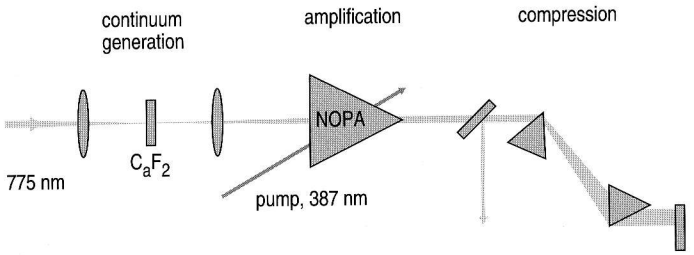

Fig. 6.39. Principle design of a NOPA [6.93]

aged into a nonlinear BBO crystal, where it represents the seed beam which overlaps with the frequency-doubled beam of the pump laser at $\lambda_p/2$. The angle between the optical axis and the seed beam allows phase-matching for sum or difference frequency generation only for a specific wavelength of the seed beam. For this orientation of the crystal, the phase and group velocities of the interacting waves must be equal. Changing this angle allows continuous tuning of the output wavelength [6.85]. For a pump wavelength $\lambda_p/2 = 387$ nm and a seed continuum between 500 nm and 800 nm, the output wavelength can be tuned across the whole visible range [6.87].

Such a widely tunable NOPA consists essentially of three parts (Fig. 6.39):

(a) The generation of a spectral continuum for the seed beam
(b) The parametric amplifier, which is the nonlinear optical crystal where pump beam and seed beam overlap and the amplified output beam is generated at the sum or difference frequency due to parametric interaction
(c) The pulse compressor, which may consist of a prism or grating arrangement (see the next section).

With such a system, pulses with widths of less than 20 fs could be generated with wavelengths that are continuously tunable in the visible between 470 nm and 750 nm and in the near infrared between 865 nm and 1600 nm [6.88].

The real experimental setup is somewhat more complicated, because of the many lenses, mirrors, beam-splitters and apertures that improve the quality of the beam. This is illustrated by Fig. 6.40, which shows a NOPA built in Freiburg [6.89].

For many spectroscopic experiments, more than one laser is necessary [6.90, 6.91]. Here a design which offers three independently tunable phase-coherent sources is very helpful [6.92]. Its principle is illustrated in Fig. 6.41.

A small fraction of the pump beam generates a broad spectral continuum in a sapphire plate. The larger fraction is frequency doubled and sent by beam splitters into three BBO crystals for parametric amplification. The seed beam collimated from the focal spot in the sapphire plate is also imaged into the three BBO crystals, where they are superimposed on the frequency-doubled pump beams. The three parametric amplifiers can be independently tuned by changing the orientations of the crystals. The total tuning range is only limited by the spectral bandwidth of the seed beam continuum.

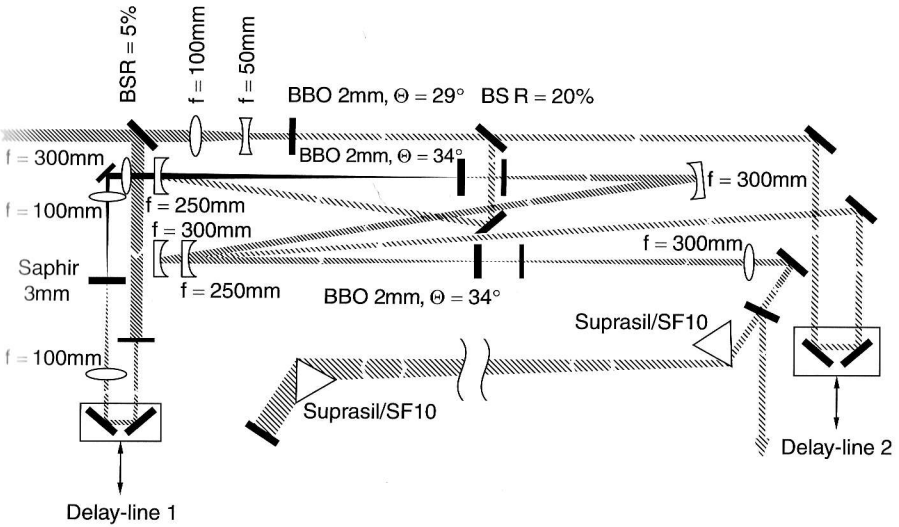

Fig. 6.40. More detailed drawing of a NOPA [6.89]

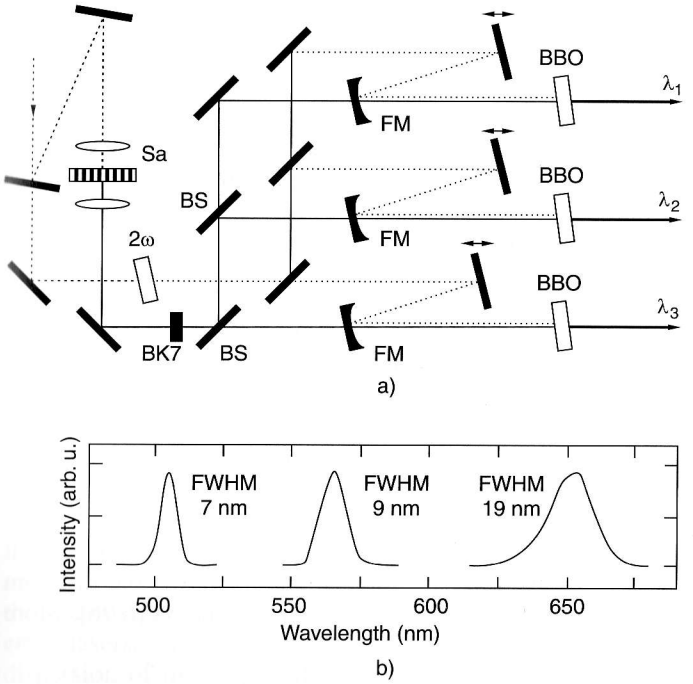

Fig. 6.41. (**a**) Three phase-locked NOPAs: *dashed*, 775 nm pump beam; *dotted*, 387 nm pump beam; *solid*, continuum; Sa, sapphire; BK7, glass substrate; BS, broadband beam [6.92]

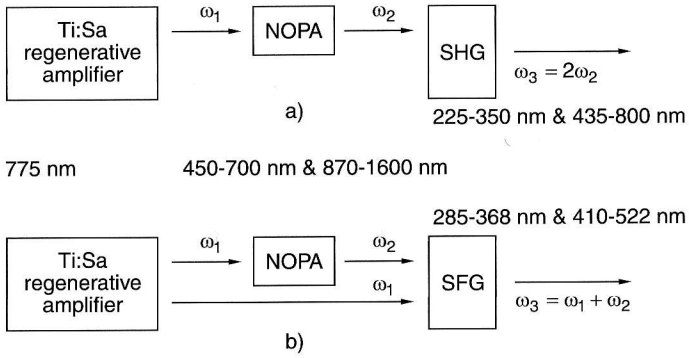

Fig. 6.42a,b. Wavelength-ranges available with NOPAs pumped by a Ti:sapphire regenerative amplifier based on second harmonic frequency generation SHG of the NOPA output (**a**) and sum-frequency generation SFG (**b**) [6.85]

The wavelength ranges available with the second harmonic and the sum-frequency generation based on parametric device schemes are illustrated by the schematic design in Fig. 6.42 [6.93].

6.1.10 Shaping of Ultrashort Light Pulses

For many applications a specific time profile of short laser pulses is desired. One example is the coherent control of chemical reactions (see Sect. 10.2) Recently, some techniques have been developed that allow such pulse shaping and that work as follows:

The output pulses of a femtosecond laser are reflected by an optical diffraction grating. Because of the large spectral bandwidth of the pulse, the different wavelengths are diffracted into different directions (Fig. 6.43). The divergent beam is made parallel by a lens and is sent through a liquid crystal display (LCD), which is formed by a two-dimensional thin array of liquid crystal pixels with transparent electrodes. The different wavelengths are now spatially separated. If a voltage is applied to a pixel, the liquid crystal changes its refractive index and with it the phase of the transmitted partial wave. Therefore the phase front of the transmitted pulse differs from that of the incident pulse, depending on the individual voltages applied to the different pixels. A second lens recombines the dispersed partial waves, and reflection by a second grating again overlaps the different wavelengths. This results in a light pulse with a time profile that depends on the phase differences between its spectral components, which in turn can be controlled by the LCD, driven by a special computer program (Fig. 6.44) [6.94, 6.95]. A self-learning algorithm can be incorporated into the closed loop, which compares the output pulse form with the wanted one and tries to vary the voltage at the different pixels in such a way that the wanted pulse form is approximated [6.96]. More details can be found in [6.97]

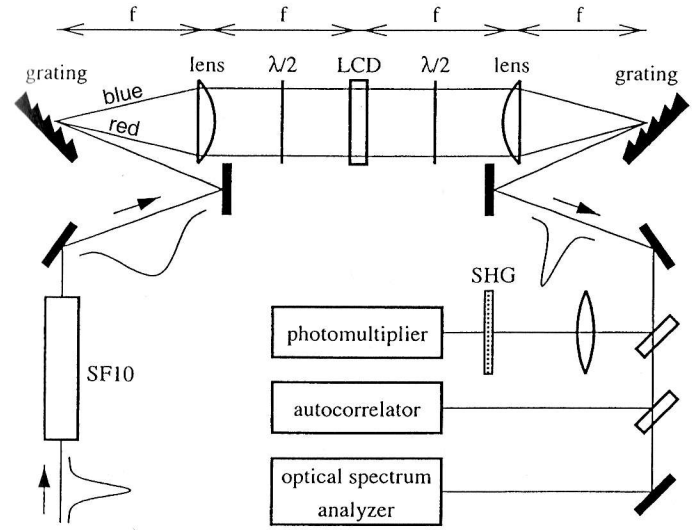

Fig. 6.43. Schematic experimental setup for pulse shaping of femtosecond pulses [6.96]

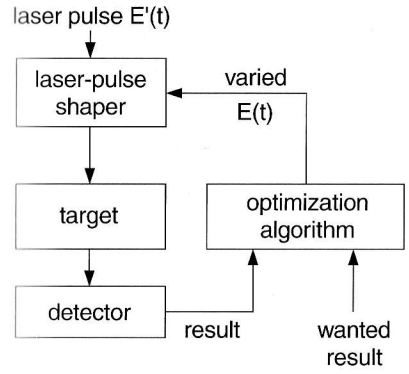

Fig. 6.44. Optimization control loop of laser pulse shaping by a learning algorithm with feedback [6.96]

6.1.11 Generation of High-Power Ultrashort Pulses

The peak powers of ultrashort light pulses, which are generated by the techniques discussed in the previous section, are for many applications not high enough. Examples where higher powers are required are nonlinear optics and the generation of VUV ultrashort pulses, multiphoton ionization and excitation of multiply charged ions, the generation of high-temperature plasmas for optical pumping of X-ray lasers, or industrial applications in short-time material processing. Therefore, methods must be developed that increase the energy and peak power of ultrashort pulses. One solution of this problem is the amplification of the pulses in dye cells that are pumped by pulsed, powerful lasers, such as excimer, Nd:YAG, or Nd:glass lasers (Fig. 6.45). The dispersion of the amplifying cells leads to a broadening of the pulse, which

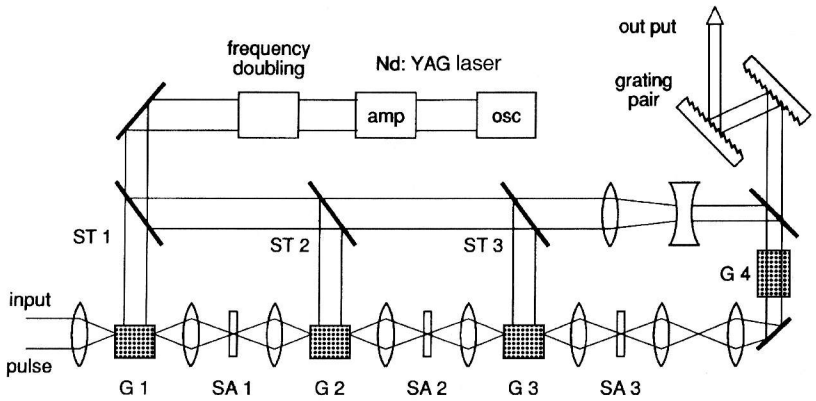

Fig. 6.45. Amplification of ultrashort light pulses through a chain of amplifier dye cells G1–G4, pumped by a frequency-doubled pulsed Nd:YAG laser. Saturable absorbers SA1–SA3 are placed between the amplifier cells in order to prevent feedback by reflection and to suppress amplified spontaneous emission

can, however, be compensated by pulse compression with a grating pair. In order to suppress optical feedback by reflection from cell windows and amplification of spontaneous emission, saturable absorber cells are placed between the amplifying states, which are saturated by the wanted high-power pulses but suppress the weaker fluorescence [6.98–6.102].

If a laser beam with intensity I_0 passes through an amplifier cell of length L and with a gain coefficient $-\alpha$ ($\alpha < 0$), the output intensity becomes

$$I_{\text{out}} = I_0 \mathrm{e}^{-\alpha L} . \tag{6.28}$$

With increasing intensity, saturation starts and the gain coefficient decreases to

$$\alpha(I) = \alpha_0/(1+S) = \alpha_0/(1+I/I_\text{s}) \tag{6.29}$$

where $\alpha_0 = \alpha(I=0)$ is the small signal gain for $I \to 0$ and I_s the saturation intensity for which $S=1$ (see Sect. 2.1). Equations (6.28) and (6.29) yield for the amplification

$$\mathrm{d}I/\mathrm{d}z = I(z)\alpha_0/(I(z)/I_\text{s}) . \tag{6.30}$$

Integration yields

$$\int (1/I + 1/I_\text{S})\, \mathrm{d}I = \alpha_0 \int \mathrm{d}z \tag{6.31}$$

$$\ln\left(\frac{I_\text{out}}{I_0}\right) + \frac{I_\text{out} - I_0}{I_\text{s}} = \alpha_0 L = \ln G_0 . \tag{6.32}$$

This gives with $I_0 = I_\text{in}$ for the amplification factor

$$G = G_0 \exp[-(I_\text{out} - I_\text{in}/I_\text{s})] \tag{6.33}$$

which results in the output intensity

$$I_\text{out} = I_0 + \ln(G_0/G) . \tag{6.34}$$

The amplified intensity therefore depends on the incident intensity I_in, the small signal gain G_0, the saturated gain G and the saturation intensity I_s. If the amplifying medium is completely saturated, the gain drops to $G=1$ and I_out is limited to the maximum value

$$I_\text{out}^\text{max} = I_\text{in} + I_\text{s} \ln G_0 \tag{6.35}$$

which can be reformed into

$$I_\text{out} = I_\text{in} \ln(G_0/G). \tag{6.36}$$

In order to achieve a larger amplification, several amplifier stages are necessary.

A serious limitation is the low repetition rate of most pump lasers used for the amplifier chain. Although the input pulse rate of the pico- or femtosecond pulses from mode-locked lasers may be many megahertz, most solid-state lasers used for pumping only allow repetition rates below 1 kHz. Copper-vapor lasers can be operated up to 20 kHz. Recently, a multi-kilohertz Ti:Al_2O_3 amplifier for high-power femtosecond pulses at $\lambda = 764$ nm has been reported [6.103].

Over the past ten years new concepts have been developed that have increased the peak power of short pulses by more than four orders of magnitude, reaching the terawatt (10^{12} W) or even the petawatt (10^{15} W) regime

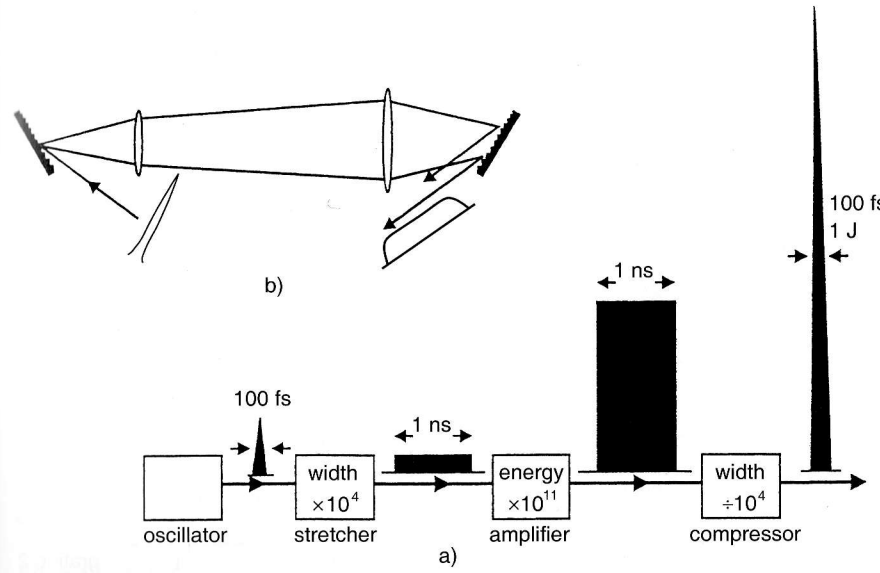

Fig. 6.46. Schematic diagram of chirped pulse amplification (CPA) [6.114]

[6.102, 6.103–6.114]. One of these methods is based on chirped pulse amplification, which works as follows (Fig. 6.46):

The femtosecond output pulse from the laser oscillator is stretched in time by a large factor, for example, 10^4. This means that a 100-fs pulse becomes 1-ns long and its peak power decreases by the same factor. This long pulse is now amplified by a factor up to 10^{10}, which increases its energy, but, because of the pulse stretching, the peak power is far smaller than for the case where the initial short pulse had been amplified accordingly. This prevents destruction of the optics by peak powers that exceed the damage threshold. Finally, the amplified pulse is again compressed before it is sent to the target.

We will now discuss the different components of this process in more detail. The oscillator consists of one of the femtosecond devices discussed previously. They deliver chirped pulses where the frequency of the light wave varies during the pulse width Δt. Such a chirped pulse can be stretched by a grating pair, where the two gratings, however, are not parallel as for pulse compression, but are tilted against each other (Fig. 6.47). This increases the path difference between the blue and the red components in the pulse and stretches the pulse length. Another design of an aberration-free pulse stretcher with two curved mirrors and a grating is described in [6.102] and is depicted in Fig. 6.48.

The amplification is performed in a multipass amplifier system. Here the stretched laser pulse is sent many times through a gain medium, which is pumped by a nanosecond pump pulse from a Nd:YAG laser (regenerative amplifier, Fig. 6.48). For amplification of Ti:sapphire pulses a highly doped Ti:sapphire crystal serves as the gain medium. After each transit of the stretched pulse through the gain medium, which depletes the inversion, the pump pulse regenerates it again. Often the system is designed in such a way that the different transits pass at slightly different locations through the amplifying medium. The number of transits depends on the geometrical mirror arrangement and is limited by the duration of the pump pulse.

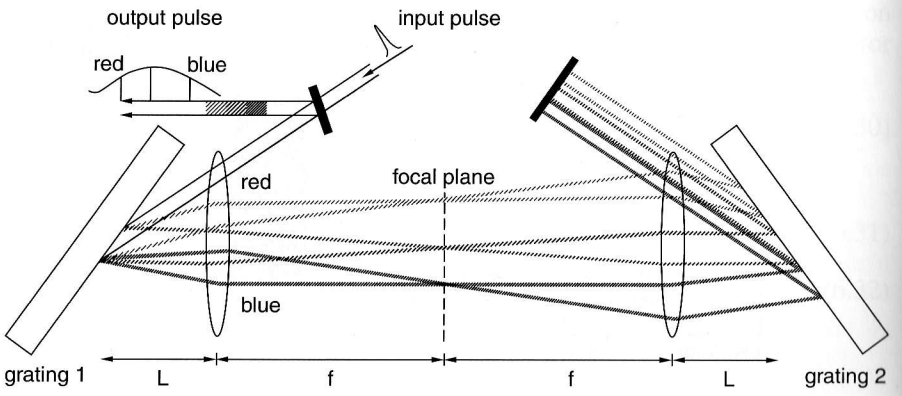

Fig. 6.47. Design for stretching femtosecond pulses and generation of a frequency chirp

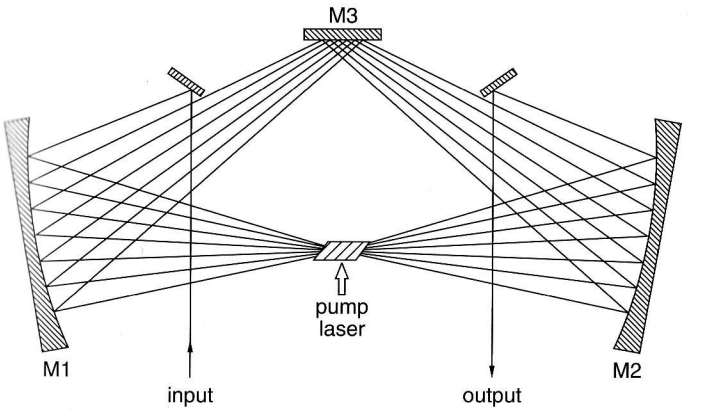

Fig. 6.48. Regenerative amplifier for short light pulses

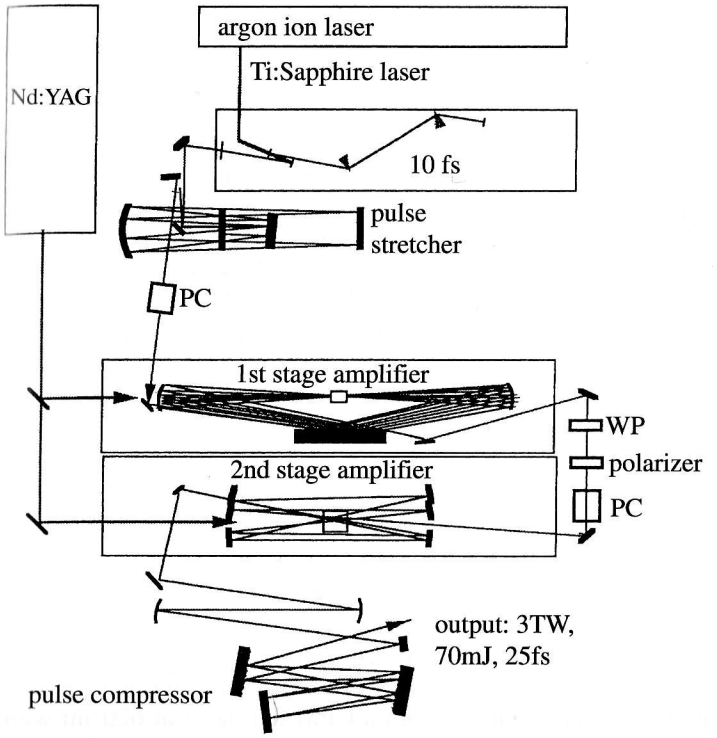

Fig. 6.49. Schematic diagram of the oscillator–amplifier system of a 3-TW 10-Hz Ti:sapphire CPA laser [6.102]

A second amplifier stage can be used for higher amplification. The different stages are separated by an optical diode, which prevents back reflections into the previous stage. A Pockels cell (PC) selects the amplified pulses with a repetition rate of a few kilohertz (limited by the pump laser) from the many more nonamplified pulses of the oscillator (at a repetition rate of about 80 MHz). The upper pulse energy that can be extracted from the amplifying medium is given by the saturation fluence, which depends on the emission cross section of the medium. For Ti:sapphire, for example, the highest achievable intensity is about $100\,\mathrm{TW/cm^2}$. Figure 6.49 shows the total setup for pulse stretching, amplification and compression.

During the multipass transits the spatial mode quality of the pulse might be deteriorated, which means that the pulse cannot be tightly focused into the target. If the multipass design forms a true resonant cavity and the incoming pulses of the pump laser and the oscillator are both carefully mode-matched to the fundamental Gaussian mode of this cavity, the resonator will only support the TEM_{00} modes and the system acts as a spatial filter, because all other transverse modes will not be amplified. Such a regenerative amplifier preserves the spatial Gaussian pulse profile, which allows one to achieve diffraction-limited tight focusing and correspondingly high intensities in the focal plane. After amplification the pulse with energy W is compressed again, thus producing pulses with a duration $\tau = 20-100\,\mathrm{fs}$ and very high peak powers $P = W/\tau$ up to several terawatts.

Example 6.4.

Assume the laser oscillator emits pulses with $\Delta t = 20\,\mathrm{fs}$ and a pulse energy of 1 nJ. The peak power of these pulses is then 50 kW. At a repetition rate of 100 MHz the average power is 0.1 W. Stretching the pulse width by a factor of 10^4 increases the pulse width to 200 ps and reduces the peak power to 5 W. For a mirror separation of 10 cm in the regenerative amplifier, the round trip time for the pulses is $T = 0.7\,\mathrm{ns}$. If the width of the pump pulse is 7 ns, 10 roundtrips can be amplified; i.e., the amplified pulse makes 20 transits through the amplifying medium during the pump pulse. With an amplification factor of 10^4, the peak power of the amplified pulses becomes 50 kW. In a second amplification stage with $G = 10^3$, the peak power increases to 50 MW and the pulse energy to 10 mJ. Compressing the pulse again by a factor of 10^4 gives a pulse peak power of $5 \times 10^{11}\,\mathrm{W} = 0.5$ terawatts.

Most of the experiments on femtosecond pulses performed up to now have used dye lasers, Ti:sapphire lasers, or color-center lasers. The spectral ranges were restricted to the regions of optimum gain of the active medium. New spectral ranges can be covered by optical mixing techniques (Sect. 5.8). One example is the generation of 400-fs pulses in the mid-infrared around $\lambda = 5\,\mu\mathrm{m}$ by mixing the output pulses from a CPM dye laser at 620 nm with pulses of 700 nm in a $LiIO_3$ crystal [6.106]. The pulses from the CPM laser are amplified in a six-pass dye amplifier pumped at a repetition rate of 8 kHz

by a copper-vapor laser. Part of the amplified beam is focused into a traveling-wave dye cell [6.107], where an intense femtosecond pulse at $\lambda = 700\,\mathrm{nm}$ is generated. Both laser beams are then focused into the nonlinear $LiIO_3$ mixing crystal, which delivers output pulses with 10-mJ energy and 400-fs pulsewidth.

A second method is based on parametric amplification. Instead of a gain medium with population inversion, here the parametric interaction between a pump wave and a signal wave in a nonlinear optical crystal is used to amplify optical pulses (see Sect. 6.1.9). The advantage of using this technique is the higher gain that results. It is possible to reach a higher amplification after just a single amplifier stage than achieved in a regenerative amplifier, where the gain is limited by saturation effects.

The nonlinear medium, however, cannot store energy as is done in the usual gain media with an inverted population. The pump, signal and idler waves must obey the phase-matching condition, but they also should overlap in time during their passage through the interaction zone in the nonlinear medium. Therefore they should have the same pulse width. A picosecond pump laser can be used for the amplification of femtosecond pulses. The femtosecond signal pulse is stretched before the parametric amplification in order to match the width of the pump pulse (Fig. 6.50), and it is then compressed after the amplification stage [6.108].

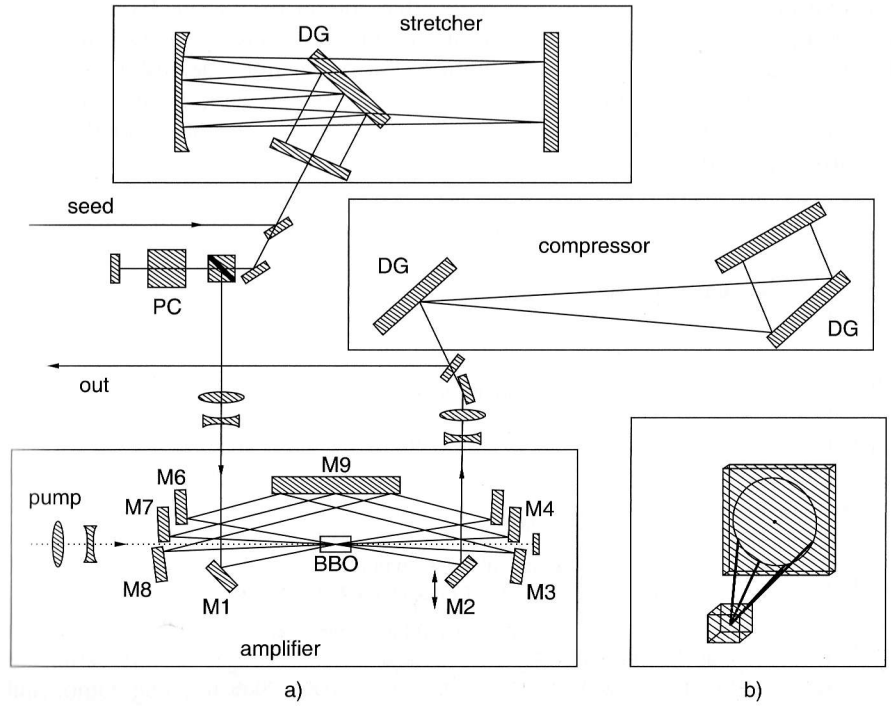

Fig. 6.50. Experimental setup for parametric amplification of ultrashort pulses, including a pulse stretcher before and a pulse compressor after amplification [6.108]

Another method uses nanosecond pump pulses. The femtosecond signal pulse is again stretched into the subnanosecond range and sent through several amplification stages. The pump pulses for these stages are delayed for each stage by a specific time interval to achieve optimum overlap with the signal pulse [6.109]. Instead of several nonlinear crystals, the signal pulses can be sent through the same crystal several times in an arrangement similar to that of a regenerative amplifier. However, the difference here is that parametric interaction is used instead of the gain medium with population inversion. Since the amplification is higher, fewer amplification stages are required, and it was shown that just a single stage of such a "regenerative parametric stage" can yield peak powers in the terawatt range [6.110].

6.1.12 Reaching the Attosecond Range

There are a lot of processes in nature that occur at timescales below 1 fs. Examples include the movement of electrons in atoms or molecules, the excitation of electrons from inner shells of atoms, and the subsequent decay of electrons from higher energy states into this hole in the core which results in X-ray emission or Auger processes. This decay may proceed within 10^{-16} s. Many more electronic processes proceed on an attosecond timescale, such as the rearrangement of the electron shell after optical excitation. Even shorter decay times can be found for excited atomic nuclei. If such processes need to be investigated with high time resolution, the probe must be faster than the investigated process [6.111]. Therefore, new techniques have been developed over the past few years that allow time resolutions in the attosecond range (1 attosecond= 10^{-18} s) [6.112, 6.113].

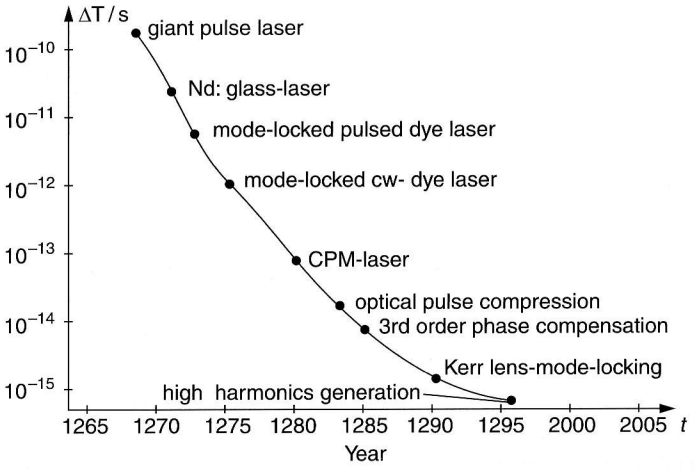

Fig. 6.51. Historical development of the progress in generating ultrashort pulses

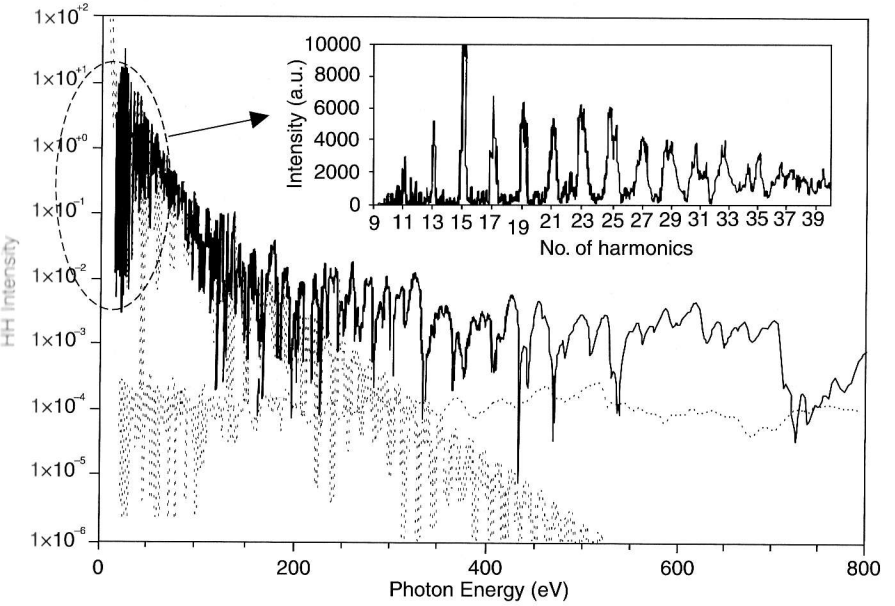

Fig. 6.52. Spectral intensity distribution of the higher harmonics produced by focussing a femtosecond terrawatt laser at $\lambda = 720$ nm into a neon jet [6.118]

One of these techniques is based on the generation of high harmonics of a powerful femtosecond laser pulse [6.115].

If the output pulse of a powerful femtosecond laser is focused into a gas jet of noble gas atoms, high harmonics of the fundamental laser wavelength are generated due to the nonlinear interaction of the laser field with the electrons of the atoms. The strong laser field, which can surpass the Coulomb field within the atom by several orders of magnitude, leads to extreme enharmonic movement of the electrons, which are accelerated back and forth with the optical frequency of the laser field. Since accelerated charges radiate, the periodically changing acceleration of the electron results in emission at frequencies $\omega_n = n\omega$ where the integer n can have values of up to 350!! For a fundamental wavelength $\lambda = 700$ nm, the harmonic $n\omega$ with $n = 350$ has a wavelength $\lambda = 2$ nm in the X-ray region. This corresponds to a photon energy of 500 eV. The intensity distribution of the higher harmonics, as generated by a 5 fs pulse at $\lambda = 720$ nm with an output peak power of 0.2 terawatt, is shown in Fig. 6.52 on a logarithmic scale. One can see that the harmonic intensity at $n\omega$ decreases with increasing n up to $n = 80$ (225 eV), while for higher harmonics it stays approximately constant. Because the power of the n-th harmonic at $\omega_n = n\omega$ is proportional to $I(\omega)^n$, the pulse width of the harmonic is much narrower than that of the pulse at ω. Only the central part of the pulse $I(\omega)$ around the peak intensity essentially contributes to the higher harmonics generation.

Another way of producing attosecond pulses with high-energy photons is based on plasma generation when a high-intensity laser beam is focused onto

the surface of a solid material. If a 5 fs pulse at $\lambda = 780\,\text{nm}$ with an intensity $I = 10^{21}\,\text{W/cm}^2$ is focused onto a solid target, the free electrons in the resulting plasma emit attosecond pulses with photon energies of 20–70 eV [6.116].

To illustrate atomic dynamics, which require subfemtosecond resolution, Fig. 6.53 shows the time-resolved field ionization of neon atoms in the optical field of a 5-fs laser pulse which consists of only three optical cycles within the pulse half width [6.119]. The whole process proceeds within about 6 fs, but one can clearly see peaks in the ionization probability at times of maxima in the optical field, which means that the time resolution is below 1 fs.

Such femto- to attosecond X-ray pulses can be used for the generation of Laue diagrams of vibrational or electronical excited molecules. The exposure time must be short compared to the vibration period in order to elucidate the structures of molecules in specific excited states excited by optical or UV femtosecond pulses. If the time delay between the two pulses is varied, structural

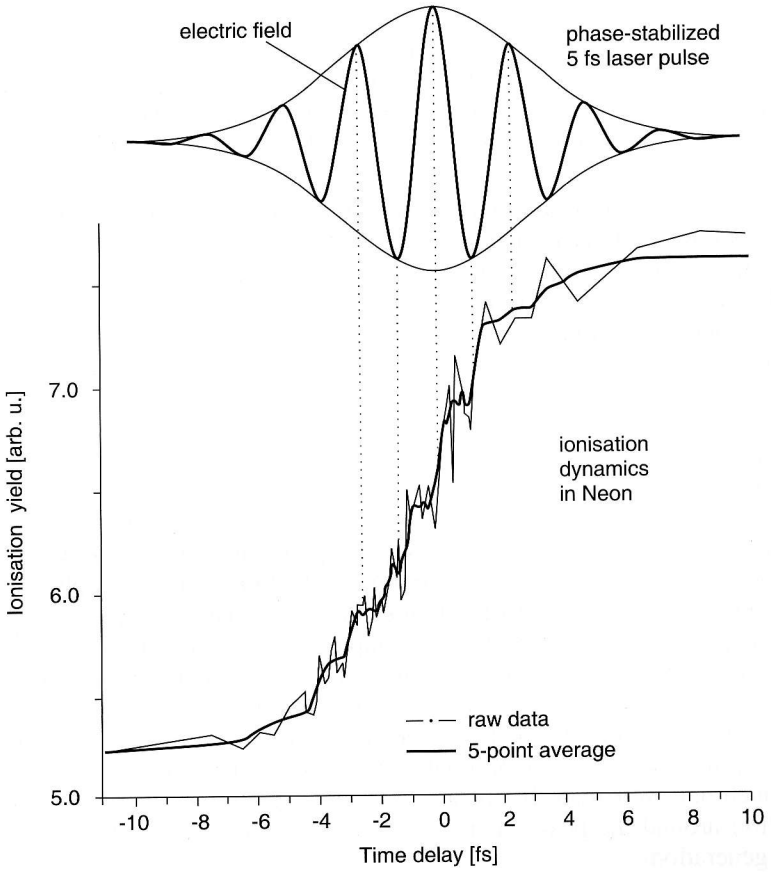

Fig. 6.53. Real-time observation of the optical field ionization of neon atoms with attosecond time resolution [6.117]

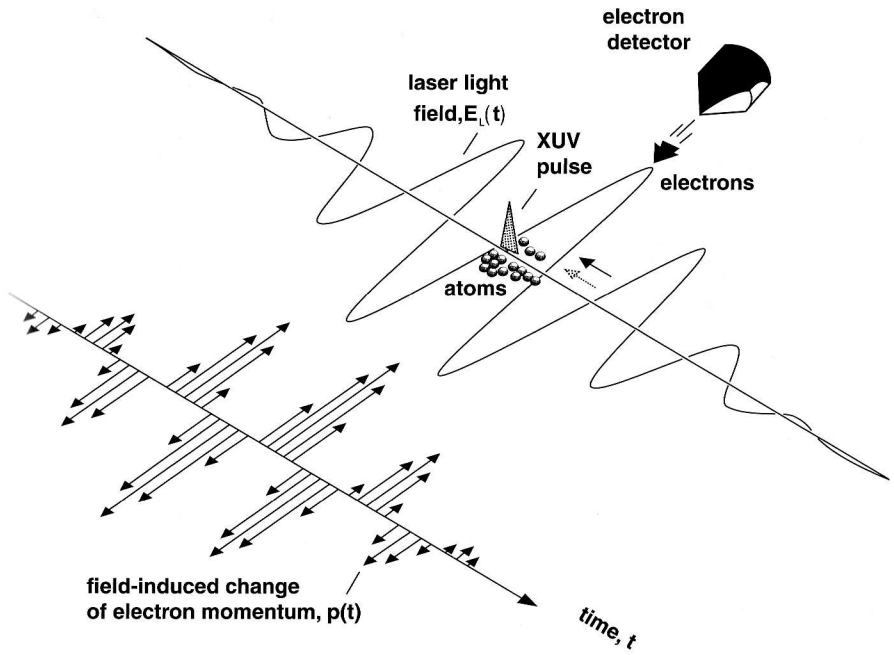

Fig. 6.54. Measuring the absolute phase of an optical field by photoelectron spectroscopy [6.118]

changes in the excited molecule during its vibrations or after the rearrangement of its electron shell following excitation can be tracked.

An interesting application is shown in Fig. 6.54, where the absolute phase of an optical field can be measured. The few-cycle optical pulses produce photoelectrons by ionizing atoms in a collimated atomic beam (see [6.113] and [6.118]). The photoelectrons are detected on both sides of the atomic beam perpendicular to the laser and atomic beams in the direction of the alternating electric field vector of the optical wave. Since the photoelectrons are generated by multiphoton absorption (for $h\nu = 1.8\,\text{eV}$, ten photons must be absorbed to ionize the neon atoms) and the number of photoelectrons depends strongly on the electric field strength. Therefore, nearly all photoelectrons are generated close to the maximum of the periodically changing field $\boldsymbol{E}(t)$. In a few-cycle pulse, $E(t)$ depends on the phase of the optical field relative to the envelope of the pulse. The largest value of $E(t)$ is achieved if the maximum of E coincides with the maximum of the pulse envelope.

There are many more applications of attosecond pulses; these can be found, for example, in the publications of the groups of P. Corkum at the NRC in Ottawa [6.121] and F. Krausz at the MPI for Quantum Optics in Garching, who have pioneered this field [6.122].

For more experimental details and special experimental setups for the generation of femtosecond and attosecond pulses, the reader is referred to the literature [6.118–6.123].

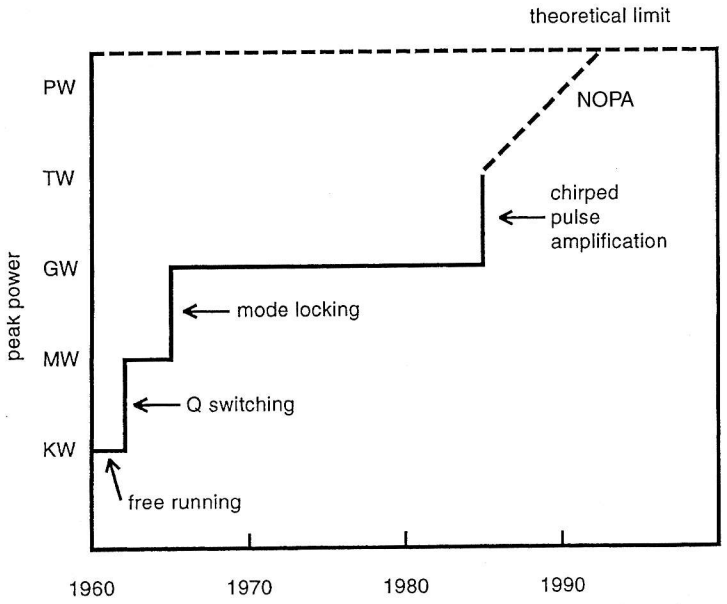

Fig. 6.55. The progress in achievable peak powers with the invention of different techniques for laser pulse generation [6.114]

6.1.13 Summary of Short Pulse Generation

There are several ways of generating short pulses. One is based on mode-locking lasers which have gain media with a broad spectral range. While the first experiments relied on dye lasers or Nd:YAG-lasers, the Ti:Sapphire laser has now become the most attractive choice. Some of the most commonly used materials are listed in Table 6.1 and [6.124]. Laser pulses down to 4 fs have been demonstrated using Kerr lens mode-locking and chirped mirrors.

Another method uses optical pulse compression in optical fibers, where the intensity-dependent part of the refractive index causes a frequency chirp and increases the spectral profile and the time duration of the pulse. Subsequent pulse compression, achieved with a pair of optical gratings or by using prisms, leads to a drastic shortening of the pulse.

A third way of generating short pulses is based on the parametric interaction of a signal pulse with a short pump pulse in a nonlinear crystal. This method allows the generation of short pulses with a wide tuning range of their center wavelength if the signal pulse comes from a point-like white light source which is generated by focusing a high-power laser pulse into a glass or CaF_2^- disk.

The path to the shorter and shorter pulses and higher peak powers achieved over the last few decades is illustrated on a logarithmic scale in Figs. 6.51 and 6.55.

Note: the extrapolation into the future may be erroneous [6.120].

6.2 Measurement of Ultrashort Pulses

During recent years the development of fast photodetectors has made impressive progress. For example, PIN photodiodes (Sect. 4.5) are available with a rise time of 20 ps [6.128]. The easiest and cheapest way to achieve measurements of pulses with $\Delta T > 10^{-10}$ s is through detection by photodiodes, CCD detectors or photomultipliers, as discussed in Sect. 4.5. However, until now the only detector that reaches a time resolution slightly below 1 ps is the streak camera [6.129]. Femtosecond pulses can be measured with optical correlation techniques, even if the detector itself is much slower. Since such correlation methods represent the standard technique for measuring of ultrashort pulses, we will discuss them in more detail.

6.2.1 Streak Camera

The basic principle of a streak camera is schematically depicted in Fig. 6.56. The optical pulse with the time profile $I(t)$ is focused onto a photocathode, where it produces a pulse of photoelectrons $N_{PE}(t) \propto I(t)$. The photoelectrons are extracted into the z-direction by a plane grid at the high voltage U. They are further accelerated and imaged onto a luminescent screen at $z = z_s$. A pair of deflection plates can deflect the electrons into the y-direction. If a linear voltage ramp $U_y(t) = U_0 \cdot (t - t_0)$ is applied to the deflection plates, the focal point of the electron pulse $(y_s(t), z_s)$ at the screen in the plane $z = z_s$ depends on the time t when the electrons enter the deflecting electric field. The spatial distribution $N_{PE}(y_s)$ therefore reflects the time profile $I(t)$ of the incident light pulse (Fig. 6.56b).

When the incident light is imaged onto a slit parallel to the x-direction the electron optics transfer the slit image to the luminescent screen S. This allows the visualization of an intensity–time profile $I(x, t)$, which might depend on the x-direction. For example, if the optical pulse is at first sent through a spectrograph with a dispersion $d\lambda/dx$, the intensity profile $I(x, t)$ reflects for different values of x the time profiles $I(\lambda, t)$ of the different spectral components of the pulse. The distribution $N_{PE}(x_s, y_s)$ on the screen S then yields the time profiles $I(\lambda, t)$ of the spectral components (Fig. 6.56c). The screen S is generally a luminescent screen (like the oscilloscope screen), which can be viewed by a video camera either directly or after amplification through an image intensifier. Often microchannel plates are used instead of the screen.

The start time t_0 for the voltage ramp $U_y = (t - t_0)U_0$ is triggered by the optical pulse. Since the electronic device that generates the ramp has a finite start and rise time, the optical pulse must be delayed before it reaches the cathode of the streak camera. This assures that the photoelectrons pass the deflecting field during the linear part of the voltage ramp. The optical delay can be realized by an extra optical path length such as a spectrograph (Sect. 6.4.1).

In commercial streak cameras the deflection speed can be selected between 1 cm/100 ps to 1 cm/10 ns. With a spatial resolution of 0.1 nm, a time

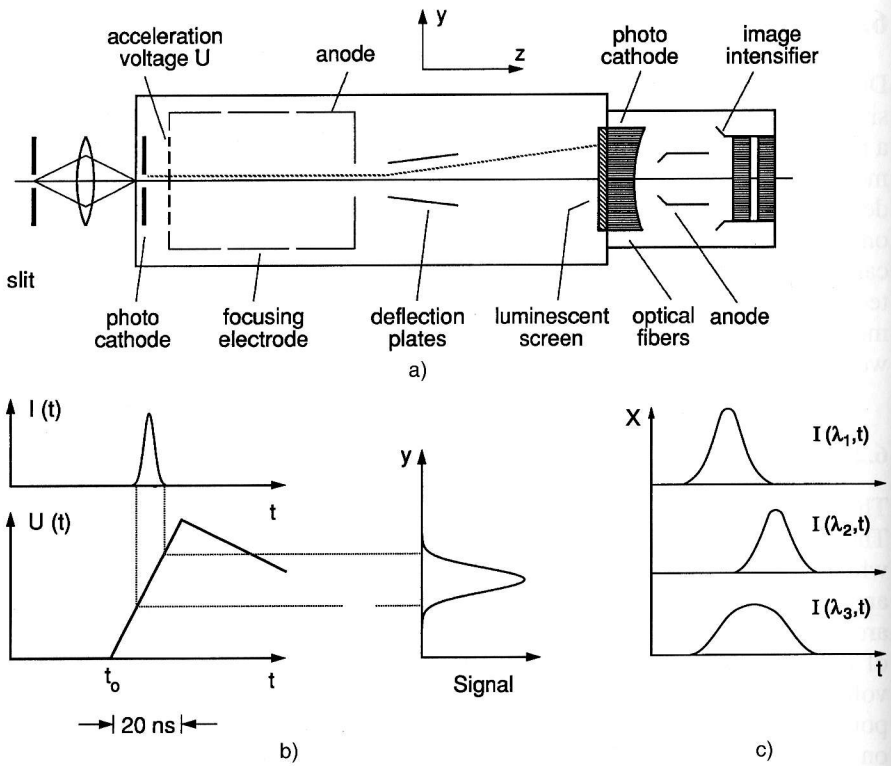

Fig. 6.56a–c. Streak camera. (**a**) Design and (**b**) schematic diagram of the relation between the time profile $I(t)$ and the spatial distribution $S(y)$ at the output plane; (**c**) spectrally resolved time profiles $I(\lambda, t)$

resolution of 1 ps is achieved. A femtosecond streak camera has been developed [6.129] that has a time resolution selectable between 400 fs to 8 ps over a spectral range 200–850 nm. Figure 6.57 illustrates this impressive resolution by showing the streak camera screen picture of two femtosecond pulses which are separated by 4 ps. More details can be found in [6.128–6.131].

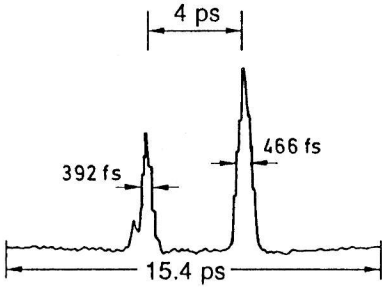

Fig. 6.57. Streak image of two subpicosecond pulses separately by 4 ps, measured with the femtosecond streak camera [6.129]

6.2.2 Optical Correlator for Measuring Ultrashort Pulses

For measurements of optical pulse widths below 1 ps the best choice is a correlation technique that is based on the following principle: the optical pulse with the intensity profile $I(t) = c\epsilon_0|E(t)|^2$ and the halfwidth ΔT is split into two pulses $I_1(t)$ and $I_2(t)$, which travel different path lengths s_1 and s_2 before they are again superimposed (Fig. 6.58). For a path difference $\Delta s = s_1 - s_2$ the pulses are separated by the time interval $\tau = \Delta s/c$ and the coherent superposition of their amplitudes $E_i(t)$ yields the total intensity at the measuring time t

$$I(t,\tau) = c\epsilon_0[E_1(t) + E_2(t-\tau)]^2 \qquad (6.37)$$
$$= I_1(t) + I_2(t-\tau) + 2c\epsilon_0 E_1(t)\cdot E_2(t-\tau)\,.$$

A *linear* detector has the output signal $S_L(t) = aI(t)$. If the time constant T of the detector is large compared to the pulse length ΔT, the output signal is

$$S_L(\tau) = a\langle I(t,\tau)\rangle = \frac{a}{T}\int_{-T/2}^{+T/2} I(t,\tau)\,dt\,. \qquad (6.38)$$

For strictly monochromatic cw light ($E_0(t) = \text{const}$) and $E_1 = E_2 = E_0\cos\omega\omega t$, the integration yields

$$S_L(\tau) = 2a\left\{\langle I_0\rangle + \frac{c\epsilon_0}{T}\int_{-T/2}^{+T/2} E_0^2\cos\omega t\,\cos\omega(t-\tau)\,dt\right\} \qquad (6.39)$$

and the signal becomes for $T\to\infty$

$$S_L(\tau) = 2aI_0(1+\cos\omega\tau) \qquad (6.40)$$

which represents on oscillatory function of the delay time τ with the oscillation period $\Delta\tau = \pi/\omega = \lambda/2c$ (two-beam interference, see Vol. 1, Sect. 4.2).

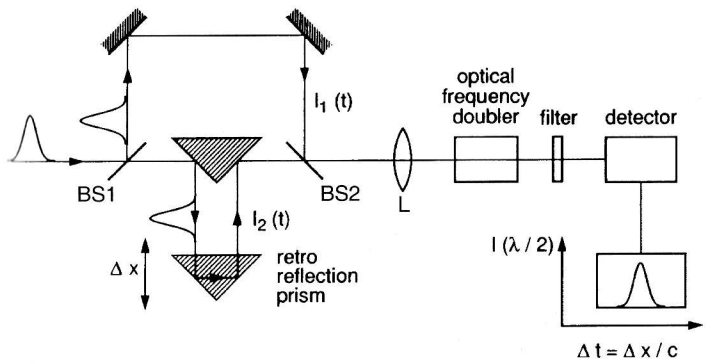

Fig. 6.58. Optical correlator with translation-retroreflecting prism and second-harmonic generation

Mode-locked pulses of duration ΔT and spectral width $\Delta\omega \approx 1/\Delta T$ are composed of many modes with different frequencies ω. The oscillations of these modes have different periods $\Delta\tau(\omega) = \pi/\omega \ll \Delta T$, and after a time $t \geq \tau_c$ their phases differ by more than π and their amplitudes cancel. In other words, the coherence time is $\tau_c \leq \Delta T$ and interference structure can only be observed for delay times $\tau \leq \Delta T$.

The signal output of the linear detector is now

$$S_L = 2a \left\{ \langle I_0 \rangle + \frac{c\epsilon_0}{\Delta\omega\, T} \int_{\omega_0-\Delta\omega/2}^{\omega_0+\Delta\omega/2} \int_{-T/2}^{+T/2} E^2(t)\, \cos\omega t\, \cos\omega(t-\tau)\, \mathrm{d}t\, \mathrm{d}\omega \right\} . \tag{6.41}$$

For $T > \Delta T = 1/\Delta\omega$ the integral vanishes and the signal does not depend on τ.

A linear detector with a time constant $T \gg \tau$ would therefore give an output signal that is independent of τ and that yields no information on the time profile $I(t)$! This is obvious, because the detector measures only the integral over $I_1(t) + I_2(t+\tau)$; that is, the sum of the energies of the two pulses, which is independent of the delay time τ as long as $T > \tau$. Therefore *linear detectors* with time resolution T cannot be used for the measurement of time profiles of ultrashort pulses with $\Delta T < T$.

If, however, the two noncollinear pulses are focused into a nonlinear optical crystal which doubles the optical frequency, the intensity of the second harmonic $I(2\omega) \propto (I_1 + I_2)^2$ is proportional to the *square* of the incident intensity (Sect. 5.7), and the measured averaged signal $S(2\omega, \tau) \propto I(2\omega, \tau)$ becomes

$$\langle S_{NL}(2\omega, \tau) \rangle \propto \frac{1}{T} \int_{-T/2}^{+T/2} \left| [E_1(t) + E_2(t-\tau)]^2 \right|^2 \mathrm{d}t\, . \tag{6.42}$$

With

$$E_1 = E(t)\, \mathrm{e}^{\mathrm{i}[\omega t + \phi(t)]}\, ;\; E_2 = E(t-\tau)\, \mathrm{e}^{\mathrm{i}[\omega(t-\tau)+\phi(t-\tau)]}$$

where $E(t)$ is the slowly varying (compared to the inverse optical frequency) envelope of the pulse, ω is its center frequency and $\phi(t)$ is the slowly varying phase (e.g., for a chirped pulse), we obtain for the detector signal after the frequency doubling crystal

$$\begin{aligned} &S_{NL}(2\omega, \tau) \\ &= C \cdot \int \left| \left\{ E(t)\, \mathrm{e}^{\mathrm{i}[\omega t + \phi(t)]} + E(t-\tau)\, \mathrm{e}^{\mathrm{i}[\omega(t-\tau)+\phi(t-\tau)]} \right\}^2 \right|^2 \mathrm{d}t \\ &= C \cdot \left[A_1 + 4A_2(\tau) + 4A_3(\tau)\, \mathrm{Re}\left\{ \mathrm{e}^{\mathrm{i}(\omega\tau+\Delta\phi)} \right\} + 2A_4(\tau)\, \mathrm{Re}\left\{ \mathrm{e}^{2\mathrm{i}(\omega\tau+\Delta\phi)} \right\} \right] \\ &=\sim A_1 + 4A_2 + 4A_3 \cos\Delta\phi\, \cos\omega\tau + 2A_4 \cos(2\Delta\phi)\, \cos(2\omega\tau)\, . \end{aligned} \tag{6.43}$$

With $\Delta\phi = \phi(t+\tau) - \phi(t)$ and

$$A_1 = \int_{-\infty}^{+\infty} \left[E^4(t) + E^4(t-\tau) \right] \mathrm{d}t \quad \text{(constant background)}$$

$$A_2(\tau) = \int_{-\infty}^{+\infty} E^2(t) \cdot E^2(t-\tau)\, \mathrm{d}t \quad \text{(pulse envelope)}$$

$$A_3(\tau) = \int_{-\infty}^{+\infty} E(t) \cdot E(t-\tau) \cdot \left[E^2(t) + E^2(t-\tau) \right] \mathrm{d}t \quad \text{Interference term at } \omega$$

$$A_4(\tau) = \int_{-\infty}^{+\infty} E^2(t) \cdot E^2(t-\tau)\, \mathrm{d}t \quad \text{Interference term at } 2\omega\, .$$

If the detector only monitors the intensity, not the phases, and if its time constant T is large compared to the pulse width ΔT ($T \gg \Delta T$), the terms $4A_3 \cos\Delta\phi \cdot \cos\omega\tau$ and $2A_4 \cos(2\Delta\phi) \cdot \cos(2\omega\tau)$ in (6.43) average to zero and (6.43) reduces to

$$S_{NL}(2\omega, \tau) \approx 2 \int I^2(t)\, \mathrm{d}t + 4 \int I(t) \cdot I(t-\tau)\, \mathrm{d}t\, . \tag{6.44}$$

The first integral is independent of τ and gives a constant background when the delay time τ is varied. The second integral, however, does depend on τ. It gives information on the intensity profile $I(t)$ of the pulse because it represents the convolution of the intensity profile $I(t)$ with the time-delayed profile $I(t+\tau)$ of the same pulse (intensity autocorrelation).

Note the difference between linear detection (6.38) and nonlinear detection (6.44). With linear detection the *sum* $I_1(t) + I_2(t-\tau)$ is measured, which is independent of τ as long as $\tau < T$. The nonlinear detector measures the signal $S(2\omega, \tau)$ that contains the *product* $I_1(t) I_2(t-\tau)$, which does depend on τ as long as τ is smaller than the maximum width of the pulses.

Note: Shifting the time from t to $t+\tau$ changes the product $I(t) \cdot I(t-\tau)$ into $I(t+\tau) \cdot I(t) = I(t) \cdot I(t+\tau)$.

All these devices, which are called *optical correlators*, measure the correlation between the field amplitude $E(t)$ or the intensity $I(t)$ at the time t and its values $E(t+\tau)$ or $I(t+\tau)$ at a later time. These correlations are mathematically expressed by normalized correlation functions of order k. The normalized first order correlation function

$$G^{(1)}(\tau) = \frac{\int_{-\infty}^{+\infty} E(t) \cdot E(t+\tau)\, \mathrm{d}t}{\int_{-\infty}^{+\infty} E^2(t)\, \mathrm{d}t} = \frac{\langle E(t) \cdot E(t+\tau) \rangle}{\langle E^2(t) \rangle}\, , \tag{6.45}$$

describes the correlation between the field amplitudes at times t and $t+\tau$. From (6.45) we obtain $G^{(1)}(0)=1$, and for pulses with a finite pulse duration ΔT (6.45) yields $G^{(1)}(\infty)=0$.

The normalized second-order correlation function

$$G^{(2)}(\tau)=\frac{\int I(t)\cdot I(t+\tau)\,\mathrm{d}t}{\int I^2(t)\cdot \mathrm{d}t}=\frac{\langle I(t)\cdot I(t+\tau)\rangle}{\langle I^2(t)\rangle}\,, \tag{6.46}$$

describes the *intensity* correlation, where again $G^{(2)}(0)=1$. The correlation signal (6.42) after the optical frequency doubler can be written in normalized form in terms of $G^{(2)}(\tau)$ for $I_1=I_2=I$ as

$$S_{\mathrm{NL}}(2\omega,\tau)\propto 2A[G^{(2)}(0)+2G^{(2)}(\tau)]=[1+2G^{(2)}(\tau)]\,. \tag{6.47}$$

Note: $S_{\mathrm{NL}}(2\omega,\tau)$ is symmetric, i.e., $S(\tau)=S(-\tau)$. This implies that a possible asymmetry of the pulse time profile does not show up in the signal S_{NL}.

There are two different techniques that are used to measure the time profiles and optical oscillations of ultrashort pulses: noncollinear intensity correlation and interferometric autocorrelation. While the former measures the envelope of the pulse, the latter can even measure the optical oscillations within the pulse envelope. Combined with the spectral resolution, the time profiles of the different spectral components within the optical pulse spectrum can be simultaneously measured by the **FROG** technique. The relative phases of these spectral components are observable using the **SPIDER** technique.

a) Noncollinear Intensity Correlation

The intensity profile $I(t)$ of the pulses is measured using the intensity correlation method. For a collinear geometry, the intensity correlation (6.47) yields the normalized signal $S(2\omega,\tau=0)=3$ for completely overlapping pulses ($\tau=0$) and the background signal $S(2\omega,\tau=\infty)=1$ for completely separated pulses ($\tau\gg\Delta T$). The signal-to-background ratio is therefore 3:1.

The τ-independent background in (6.42) can be suppressed when the two beams are focused into the doubling crystal under different angles $\pm\beta/2$ against the z-direction (Fig. 6.59) where the signal $S(2\omega)$ is detected. If the phase-matching conditions for the doubling crystal (Sect. 5.7) are chosen in such a way that for two photons out of the same beam no phase matching occurs, but only for one photon out of each beam, such that the term A_1 in (6.43) does not contribute to the signal (background-free detection) [6.132, 6.133]. In another method of background-free pulse measurement the polarization plane of one of the two beams in Fig. 6.59 is turned in such a way that a properly oriented doubling crystal (generally, a KDP crystal) fulfills the phase-matching condition only if the two photons each come from a different beam [6.134]. In this noncollinear scheme no interference occurs (A_3 and $A_4=0$) and the measured signal equals the envelope of the pulse profile in

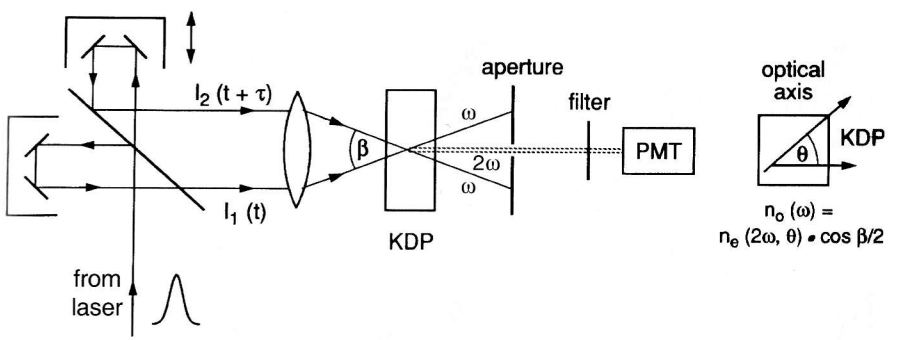

Fig. 6.59. Background-free measurement of the second-order correlation function $G^{(2)}(\tau)$ by choosing the phase-matching condition properly (SF, spectral filter neglecting scattered light of the fundamental wave at ω; KDP, potassium-dihydrogen-phosphate crystal for frequency doubling)

Fig. 6.64. For methods with background suppression no signal is obtained for $\tau\gg\Delta T$.

In the methods discussed above, one of the retroreflectors is mounted on a translational stage moved via micrometer screws by a step motor while the signal $S(2\omega,\tau)$ is recorded. Since τ must be larger than ΔT, the translational move should be at least $\Delta S=\frac{1}{2}c\tau\geq\frac{1}{2}c\Delta T$. For pulses of 10 ps this means $\Delta S\geq 1.5$ mm. With a rotating correlator (Fig. 6.60) the signal $S(2\omega,\tau)$ can be directly viewed on a scope, which is very useful when optimizing the pulse width. Two retroreflecting prisms are mounted on a rotating disc. During a certain fraction ΔT_{rot} of the rotation period T_{rot} the reflected beams reach the mirrors M1 and M2 and are focused into the KDP crystal. The viewing oscilloscope is triggered by a pulse obtained by reflecting the light of a LED onto the photodetector PD. A compact autocorrelator for measuring

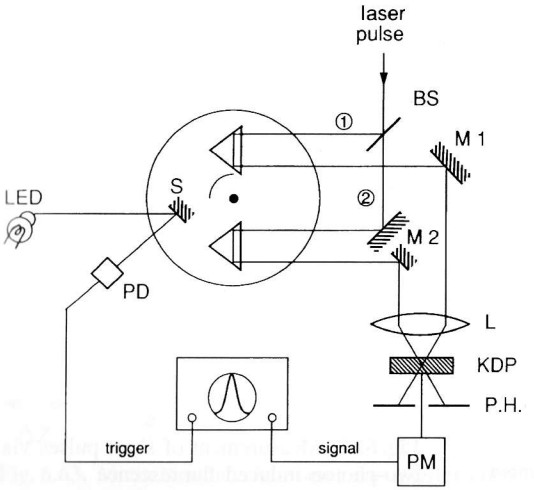

Fig. 6.60. Rotating autocorrelator allowing direct observations of the correlation signal $S(2\omega,\tau)$ on a scope that is triggered by the output signal of the photodiode PD

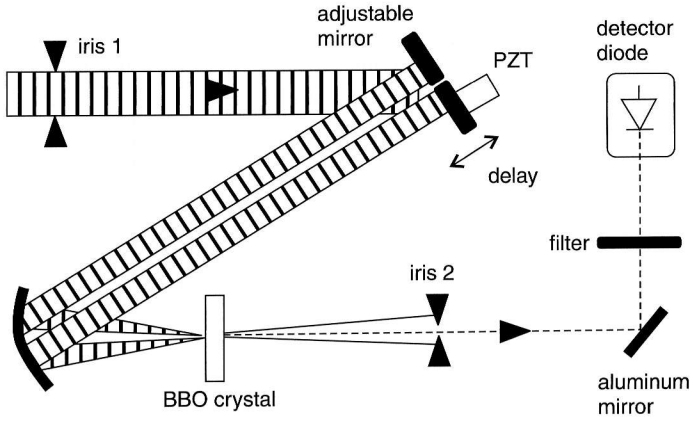

Fig. 6.61. Compact autocorrelator for measuring femtosecond pulses [6.136]

the intensity profile of femtosecond pulses from tunable sources is shown in Fig. 6.61. This device allows online measurements of pulses with 100 Hz to 10 kHz repetition rates in the wavelength range 420–1460 nm. The time delay is controlled by a piezo translator [6.136].

Instead of using optical frequency doubling other nonlinear effects can also be used, such as two-photon absorption in liquids or solids, which can be monitored by the emitted fluorescence. If the optical pulse is again split into two pulses traveling in the opposite $\pm z$-directions through the sample cell (Fig. 6.62), the spatial intensity profile $I_{FL}(z) \propto I^2(\omega, \tau)$ can be imaged by magnifying optics onto a vidicon or an image intensifier. Since a pulse width $\Delta T = 1$ ps corresponds to a path length of 0.3 mm, this technique, which is

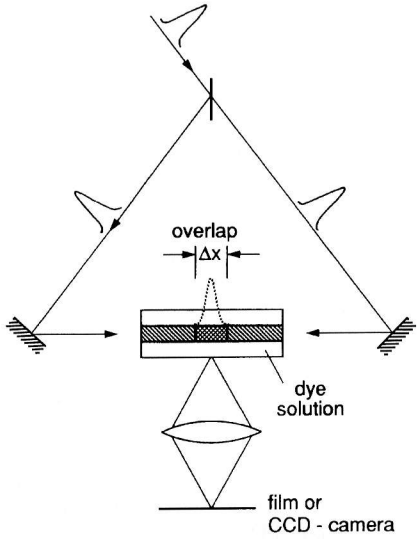

Fig. 6.62. Measurement of short pulses via two-photon induced fluorescence

based on the spatial resolution of the fluorescence intensity, is limited to pulse widths $\Delta T \geq 0.3$ ps. For shorter pulses the delay time τ between the pulses has to be varied and the total fluorescence

$$I_{FL}(\tau) = \int I(z, \tau)\, dz\,, \tag{6.48}$$

has to be measured as a function of τ [6.135, 6.137].

b) Interferometric Autocorrelation

In interferometric autocorrelation the coherent superposition of the two collinear partial beams is realized. The basic principle is shown in Fig. 6.58. The incoming laser pulse is split by the beamsplitter BS1 into two parts, which travel through two different pathlengths and are then collinearly superimposed at BS2. When they are focused by the lens L into a nonlinear optical crystal, the output signal (6.42) is generated at 2ω. Instead of the delay line arrangement in Fig. 6.58 a Michelson interferometer in Fig. 6.63 can also be used. The second harmonics are detected by a photomultiplier, while the fundamental wavelength is rejected by a filter.

The nonlinear crystal can be omitted, if the detector itself has a nonlinear response. This is, for instance, the case for a semiconductor detector with a band gap $\Delta E > h\nu$, where only two-photon absorption contributes to the signal.

In interferometric autocorrelation, averaging is not complete (unlike in intensity correlation), and the phases of the electric fields have to be taken into account. Here all of the terms A_1–A_4 in (6.43) can contribute to the signal. If a filter which rejects the fundamental frequency ω and transmits only the doubled frequency 2ω is inserted behind the frequency-doubling crystal, the third term in (6.43) with A_3 is suppressed.

A typical signal as a function of the delay time τ is shown in Fig. 6.64.

The upper envelope of this interference pattern is obtained if the phase $\omega_0\tau$ is replaced by the constant phase 2π, the lower envelope for $\omega_0\tau = \pi$. The maximum signal is, according to (6.43), $S_N^{max}(2\omega, \tau) = 8$, while the background $S(2\omega, \infty) = 1$. The signal-to-background ratio of 8:1 is therefore larger than that for intensity correlation. For $\omega_0\tau = \pi$, the minimum value is $S_N^{min}(2\omega, \tau) = 0$ (Fig. 6.64).

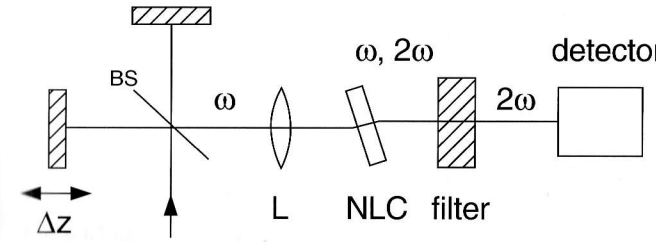

Fig. 6.63. Michelson interferometer for interferometric autocorrelation

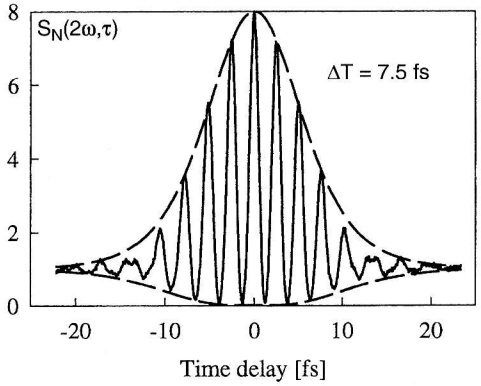

Fig. 6.64. Interferometric autocorrelation trace of a 7.5-fs pulse with upper and lower envelopes [6.127]

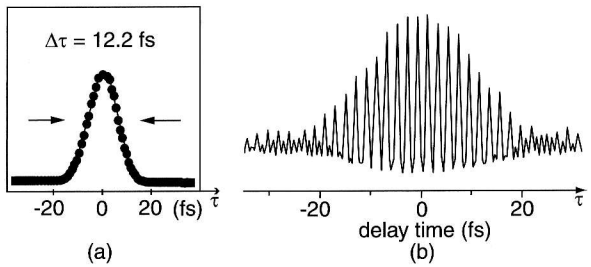

Fig. 6.65a,b. A femtosecond pulse with time duration $\Delta T = 12.2$ fs: (**a**) measured with intensity correlation; (**b**) measured with interferometric autocorrelation [6.138]

For illustration, Fig. 6.65 shows a 12-fs pulse measured with intensity correlation (**a**) and interferometric autocorrelation (**b**).

It is important to note that the profile $S(\tau)$ of the correlation signal depends on the time profile $I(t)$ of the light pulse. It gives the correct pulse width ΔT only if an assumption is made about the pulse profile. For illustration, Fig. 6.66a depicts the signal $S(2\omega, \tau)$ of Fourier-limited pulses with the Gaussian profile $I(t) = I_0 \exp(-t^2/0.36\Delta T^2)$ with and without background suppression. From the halfwidth $\Delta\tau$ of the signal the halfwidth ΔT of the pulses can only be derived if the pulse profile $I(t)$ is known. In Table 6.2 the ratio $\Delta\tau/\Delta T$ and the products $\Delta T \cdot \Delta\nu$ are compiled for different pulse profiles $I(t)$, while Fig. 6.66a–c illustrates the corresponding profiles and contrasts of $G^{(2)}(\tau)$. Even noise pulses and continuous random noise result in a maximum of the correlation function $G^{(2)}(\tau)$ at $\tau = 0$ (Fig. 6.66d), and the contrast becomes $G^{(2)}(0)/G^{(1)}(\infty) = 2$ [6.132, 6.140]. For the determination of the real pulse profile one has to measure the function $G^{(2)}(\tau)$ over a wider range of delay times τ. Generally, a model profile is assumed and the calculated functions $G^{(2)}(\tau)$ and even $G^{(3)}(\tau)$ are compared with the measured ones [6.141].

Table 6.2. Ratios $\Delta\tau/\Delta T$ of the width $\Delta\tau$ of the autocorrelation profile and ΔT of the pulse $I(t)$, and products $\Delta\nu \cdot \Delta T$ of spectral width $\Delta\nu$ and duration ΔT of pulses with different profiles $I(t)$

Pulse profile	Mathematical expression for $I(t)$	$\Delta\tau/\Delta T$	$\Delta\nu \cdot \Delta T$
Rectangular	$\begin{cases} I_0 \text{ for } 0 \le t \le \Delta T\,, \\ 0 \text{ elsewhere} \end{cases}$	1	0.886
Gaussian	$I_0 \exp[-t^2/(0.36\Delta T^2)]$	$\sqrt{2}$	0.441
Sech^2	$\text{sech}^2(t/0.57\Delta T)$	1.55	0.315
Lorentzian	$[1+(2t/\Delta T)^2]^{-1}$	2	0.221

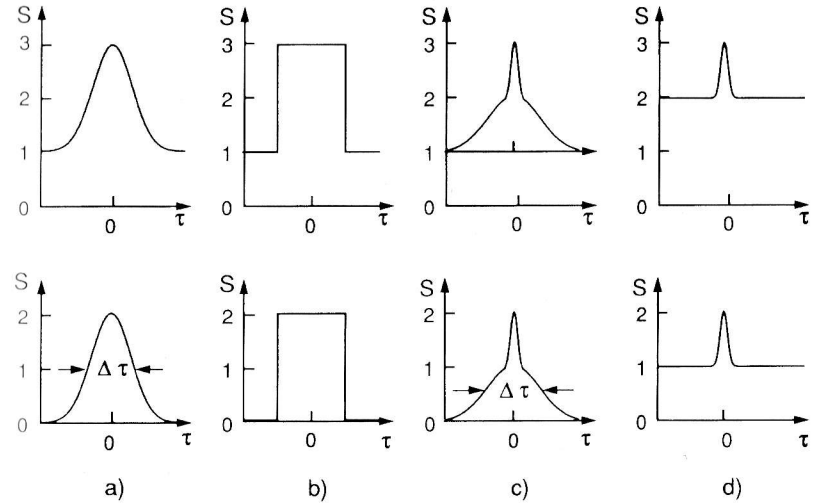

Fig. 6.66a–d. Autocorrelation signal $S \propto G^{(2)}(\tau)$ for different pulse profiles without background suppression (*upper part*) and with background suppression (*lower part*): (**a**) Fourier-limited Gaussian pulse; (**b**) rectangular pulse; (**c**) single noise pulse; and (**d**) continuous noise

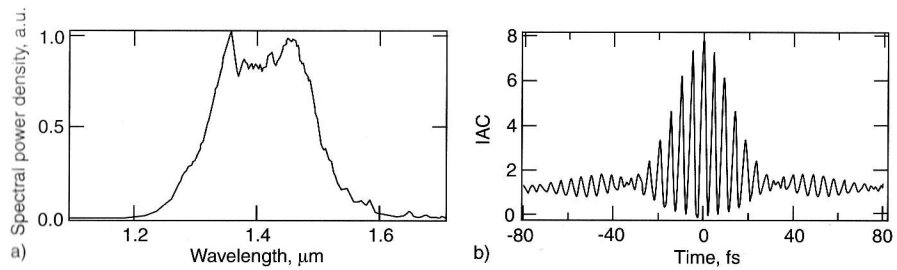

Fig. 6.67a,b. Femtosecond laser pulse. (**a**) Optical power spectrum; (**b**) interferometric autocorrelation of the same pulse [6.183]

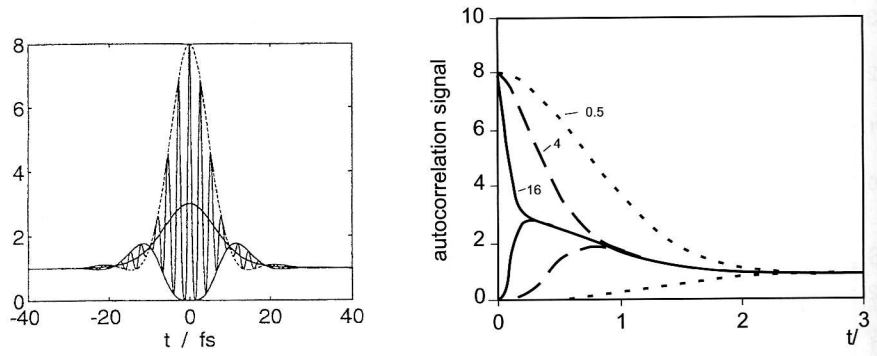

Fig. 6.68. (**a**) Interferometric autocorrelation of a pulse with $\Delta T = 10\,\text{fs}$ and a chirp of $a = 2$ (*dashed line*). The *solid line* shows the pulse profile obtained by intensity correlation. (**b**) Upper and lower envelopes of a chirped Gaussian pulse [6.50] for various chirp parameters a [6.142]

In Fig. 6.67 the power density spectrum and the interferometric autocorrelation signal of a femtosecond laser pulse is compared.

In Fig. 6.68 a chirped hyperbolic secant pulse

$$E(t) = [\text{sech}(t/\Delta T)]^{(1-\text{i}a)} = \left(\frac{2}{\text{e}^{t/\Delta T} + \text{e}^{-t/\Delta T}}\right)^{(1-\text{i}a)} , \tag{6.49}$$

is shown for $a = 2$ and $\Delta T = 10\,\text{fs}$. Chirped pulses result in a more complex autocorrelation signal.

With interferometric autocorrelation the chirp of a pulse and the resulting change in its time profile can be determined. This is illustrated by the example of a chirped pulse with a Gaussian profile

$$E(t = E_0 \exp\left[-(1+\text{i}a)(t/\Delta T)^2\right] \tag{6.50}$$

where ΔT is the width of the unchirped pulse ($a = 0$). The interferometric autocorrelation gives for such a pulse:

$$G_2(\tau) = 1 + 2\text{e}^{-(\tau/\Delta T)^2} + 4\text{e}^{-\left[\frac{3+a^2}{4}(\tau/\Delta T)^2\right]} \cdot \cos\frac{a}{2}\left(\frac{\tau}{\Delta T}\right)^2 \cdot \cos\omega\tau + 2\text{e}^{-(1+a^2)(\tau/\Delta T)^2} \cdot \cos 2\omega\tau \, . \tag{6.51}$$

In Fig. 6.68b, the upper and lower envelopes of the autocorrelation signal are plotted as a function of the normalized delay time $\tau/\Delta T$ for different values of the chirp parameter a in (6.50) [6.142].

The drawback of the techniques discussed so far is their lack of phase measurements for the different spectral components within the pulse spectral

profile. This can be overcome by the *frequency-resolved optical gating* technique (FROG) [6.143].

6.2.3 FROG Technique

We have seen that the second-order autocorrelations are symmetric and therefore do not provide any information on possible pulse asymmetries. Here the FROG technique is useful, since it allows measurements of the third-order autocorrelation. Its basic features are depicted in Fig. 6.69: as in the other autocorrelation techniques the incoming pulse is split by a polarizing beamsplitter into two partial beams with amplitudes E_1 and E_2. The probe pulse with amplitude $E_1(t)$ passes through a shutter (Kerr cell), which is opened by the delayed fraction $E_2(t-\tau)$ of the same pulse. The signal transmitted by the Kerr gate is then

$$\boldsymbol{E}_s(t, \tau) \propto \boldsymbol{E}(t) \cdot g(t-\tau) \, , \tag{6.52}$$

where g is the gate function $g(t-\tau) \propto I_2(t-\tau) \propto E_2^2(t-\tau)$.

If the transmitted pulse is sent through a spectrometer, where it is spectrally dispersed, a CCD camera will record the time dependence of the spectral components, which gives the two-dimensional function

$$I_t(\Omega, \tau) = \left| \int_{-\infty}^{+\infty} \boldsymbol{E}(t) \cdot g(t-\tau)\, \text{e}^{\text{i}\Omega t} \right| . \tag{6.53}$$

In Fig. 6.70 this two-dimensional function is illustrated for a Gaussian pulse profile without frequency chirp and for a chirped pulse.

The integration of (6.52) over the delay time, which can be experimentally achieved by opening the gate for a time larger than all relevant delay times, yields the time profile of the pulse

$$\boldsymbol{E}(t) = \int_{-\infty}^{+\infty} \boldsymbol{E}_s(t, \tau)\, \text{d}\tau \, . \tag{6.54}$$

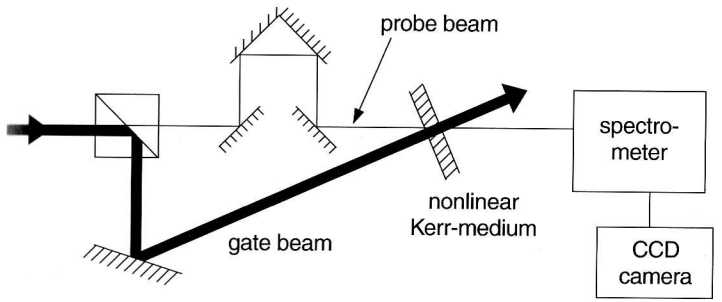

Fig. 6.69. Schematic experimental setup for FROG

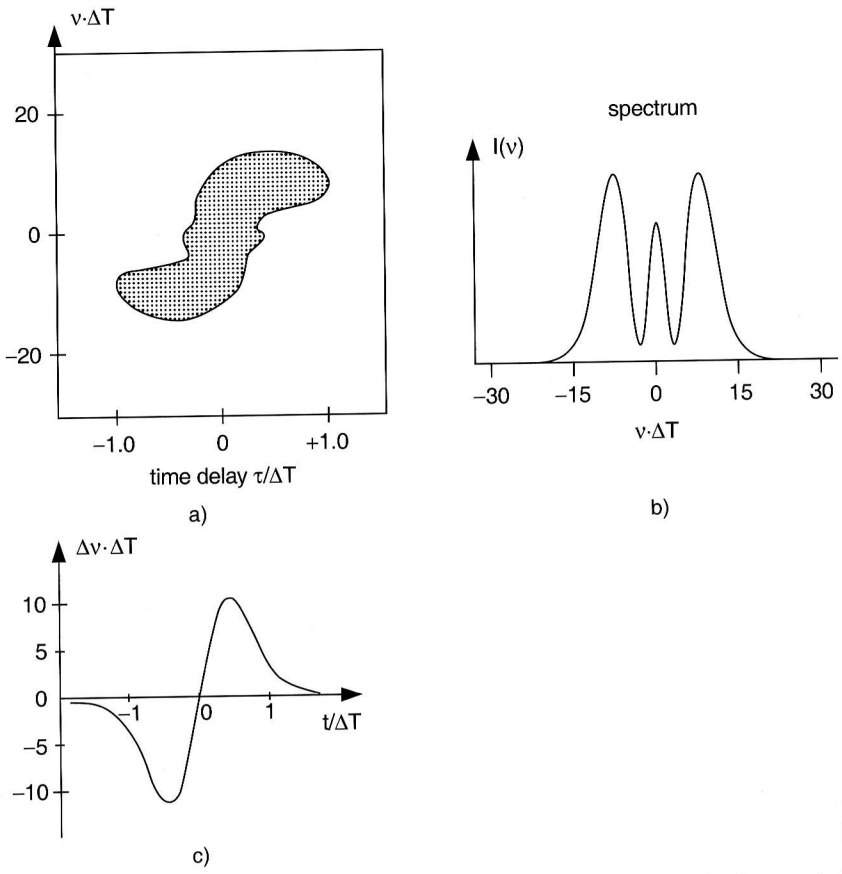

Fig. 6.70a–c. Information drawn from FROG: (**a**) plot of measured light frequencies versus delay time τ in units of pulse length ΔT; (**b**) frequency spectrum of (a); (**c**) frequency chirp [6.144]

The two functions $E_s(t, \Omega)$ and $E_s(t, \tau)$ form a Fourier pair, related to each other by

$$\boldsymbol{E}_s(t, \Omega_\tau) = \frac{1}{2\pi} \int_{-\infty}^{+\infty} \boldsymbol{E}_s(t, \tau)\, \mathrm{e}^{-\mathrm{i}\Omega_\tau \cdot \tau}\, \mathrm{d}\tau \,. \tag{6.55}$$

The measured spectrogram $S_E(\Omega, \tau)$ can be expressed by

$$I_E(\Omega, \tau) = \left| \int_{-\infty}^{+\infty} \int_{-\infty}^{+\infty} \boldsymbol{E}_s(t, \Omega_\tau)\, \mathrm{e}^{-\mathrm{i}\Omega t + \mathrm{i}\Omega_\tau \cdot \tau}\, \mathrm{d}\Omega_\tau\, \mathrm{d}t \right|^2 . \tag{6.56}$$

The unknown signal $E(t, \Omega)$ can be extracted by a two-dimensional (the two dimensions are t and τ) phase retrieval. The reconstruction of the pulse $E(t, \Omega)$ yields the instantaneous frequency as a function of time and the pulse spectrum, shown in Fig. 6.70b [6.145].

For more information on the FROG technique and the recent literature on this subject, see [6.145].

6.2.4 SPIDER Technique

The FROG method provides information on the time-dependent frequency spectrum of a short pulse but cannot measure the phases of these spectral components. A newly developed technique is helpful in this case; this method is called SPIDER (**S**pectral **P**hase **I**nterferometry for **D**irect **F**ield **R**econstruction). It uses the interference structure generated when two spatially separated pulses are superimposed [6.146]. Similar to the autocorrelation method, the two pulses are generated from the input pulse that is to be measured, using a beam splitter and a delay line which changes the time delay between the two pulses. The second pulse is therefore a copy of the first pulse with a time delay τ. The electric field amplitude

$$E(x) = \sqrt{I(x)}\, \mathrm{e}^{\mathrm{i}\phi(x)}$$

of the first pulse interferes with the field

$$E(x + \Delta x) = \sqrt{I(x + \Delta x)}\, \mathrm{e}^{\mathrm{i}\phi(x+\Delta x)}$$

of the second pulse. The detector measures the square of the total amplitude and delivers the signal

$$S(x, \Delta x) = I(x) + I(x + \Delta x) + 2\sqrt{I(x)}\,\sqrt{I(x + \Delta x)}\, \cos\{\phi(x) - \phi(x + \Delta x)\} \,.$$

The intensity measurement at the location x is therefore related to the phase difference $\Delta\phi = \phi(x) - \phi(x + \Delta x)$ between the phases of the wavefront at the locations x and $x + \Delta x$.

These two pulses are superimposed in a nonlinear crystal with a third pulse with a large frequency chirp where the sum frequencies $\omega_1 + \omega_3$ and $\omega_2 + \omega_3$ are generated (Fig. 6.71). This third pulse, which is generated from the input pulse by beam-splitting, is sent through a dispersive medium where a frequency chirp is produced which makes the pulse much broader than the two other pulses. Because of the chirp, the superposition of the third pulse with the first pulse gives another sum frequency $\omega_1 + \omega_3$, and than $\omega_2 + \omega_3$ with the second delayed pulse. When the frequency ω_3 of the chirped pulse changes during the delay time Δt by $\Delta\omega = \Omega$, the detector receives the signal

$$\begin{aligned} S(\omega) = {} & I(\omega + \omega_3) + I(\omega + \omega_3 + \Omega) \\ & + 2\sqrt{I(\omega + \omega_3)}\,\sqrt{I(\omega + \omega_3 + \Omega)}\, \cos\{\phi(\omega + \omega_3) - \phi(\omega + \omega_3 + \Omega)\} \,. \end{aligned}$$

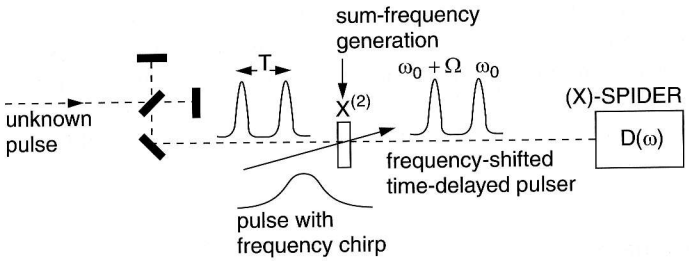

Fig. 6.71. Schematic representation of the SPIDER technique [6.147]

This signal is measured behind a spectrograph as a function of the delay Δt between pulses 1 and 2. The measured frequency shift $\Omega = \phi \Delta t$ of the sum frequency gives the phase $\phi(t)$ of the unknown input pulse and its time profile $I(t)$. Figure 6.72 illustrates the principle of the SPIDER technique using a schematic diagram.

One drawback of the FROG and SPIDER techniques is the fact that the pulse measurement does not take place at the location of the sample where the short pulse is used to investigate time-dependent processes in atoms or molecules. This is where the pulse profile and its phases actually need to be determined. In order to remove this drawback, E. Riedle and his group [6.147] extended the SPIDER technique into the ZAP-SPIDER method (**Z**ero **A**dditional **P**hase **SPIDER**), which is illustrated in Fig. 6.73. Here the unknown pulse is sent directly into the nonlinear crystal, where it is superimposed by two chirped pulses from slightly different directions and which have a delay Δt. The pulses at the sum frequency generated in the nonlinear crystal have different frequencies ω_s and $\omega_s + \Omega$, and are emitted in different directions because of the phase-matching condition for sum frequency generation. One of these sum frequency pulses is sent through a variable delay line and is then superimposed onto the other pulse. This gives rise to an interference pattern, which depends on the relative phase between the two pulses and contains all of the information on the time profiles and phases of the unknown pulse. The spectrum of the two pulses can be measured using a spectrograph. The experimental setup is shown in Fig. 6.74: the chirp is produced by sending part of the pulse from a femtosecond laser through a dispersive SF57 glass block which also stretches the pulsewidth to 2 ps. The pulse delay can be controlled with a retroreflector on a translational stage. This pulse is again split by the beam splitter BS into two pulses which can be separately delayed and are then sent into the BBO nonlinear crystal, where they are superimposed onto the unknown pulse and the sum frequency is generated.

6.3 Lifetime Measurement with Lasers

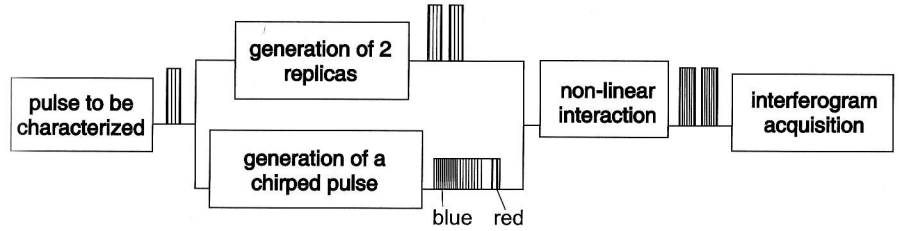

a)

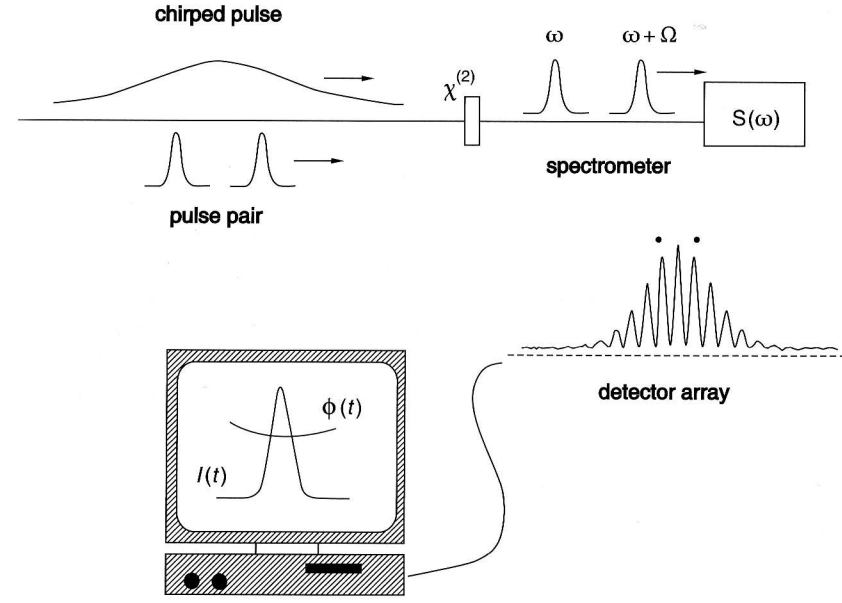

$$S(\omega) = I(\omega) + I(\omega + \Omega) + 2\sqrt{I(\omega) I(\omega + \Omega)}$$
$$\times \cos\{\phi(\omega + \Omega) - \phi(\omega) + \omega\tau\}$$

b)

Fig. 6.72. (**a**) Principle of SPIDER; (**b**) pulse sequence, profiles and measured signal [6.139]

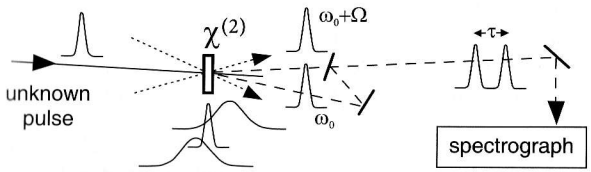

Fig. 6.73. Schematic principle of ZAP-SPIDER [6.147]

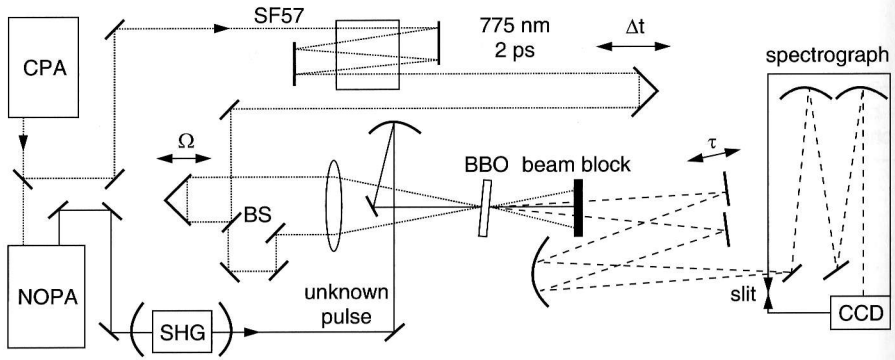

Fig. 6.74. Experimental setup for the ZAP-SPIDER technique [6.147]

Measurements of lifetimes of excited atomic or molecular levels are of great interest for many problems in atomic, molecular, or astrophysics, as can be seen from the following three examples:

(i) From the measured lifetimes $\tau_k = 1/A_k$ of levels $|k\rangle$, which may decay by fluorescence into the lower levels $|m\rangle$, the absolute transition probability $A_k = \sum_m A_{km}$ can be determined (Sect. 2.7). Knowing the lifetime of level $|k\rangle$ the relative intensities I_{km} of transitions $|k\rangle \rightarrow |m\rangle$ allow the determination of the absolute transition probabilities A_{km}. This yields the transition dipole matrix elements $\langle k|\boldsymbol{r}|m\rangle$ (Sect. 2.7.4). The values of these matrix elements are sensitively dependent on the wave functions of the upper and lower states. Lifetime measurements therefore represent crucial tests for the quality of computed wave functions and can be used to optimize models of the electron distribution in complex atoms or molecules.

(ii) The intensity decrease $I(\omega, z) = I_0 \mathrm{e}^{-\alpha(\omega)z}$ of light passing through absorbing samples depends on the product $\alpha(\omega)z = N_i \sigma_{ik}(\omega)z$ of the absorber density N_i and the absorption cross section σ_{ik}. Since σ_{ik} is proportional to the transition probability A_{ik} (2.22, 2.44), it can be determined from lifetime measurements (see item (i)). Together with measurements of the absorption coefficient $\alpha(\omega)$ the density N_i of the absorbers can be determined. This problem is very important for testing of models of stellar atmospheres [6.148]. A well-known example is the measurement of absorption profiles of Fraunhofer lines in the solar spectrum. They yield density and temperature profiles and the abundance of the elements in the sun's atmosphere (photosphere and chromosphere). The knowledge of transition probabilities allows absolute values of these quantities to be determined.

(iii) Lifetime measurements are not only important to gain information on the dynamics of excited states but also for the determination of absolute cross sections for quenching collisions. The probability R_{kn} per second for the

collision-induced transition $|k\rangle \rightarrow |n\rangle$ in an excited atom or molecule A

$$R_{kn} = \frac{1}{\overline{v}} \int_0^\infty N_\mathrm{B}(v)\sigma_{kn}(v)v\,\mathrm{d}v = N_\mathrm{B}\langle\sigma_{kn}^\mathrm{coll} \cdot v\rangle \approx N_\mathrm{B}\langle\sigma_{kn}^\mathrm{coll}\rangle \cdot \overline{v}\,, \tag{6.57}$$

depends on the density N_B of the collision partners B, the collision cross section $\sigma_{kn}^\mathrm{coll}$, and the mean relative velocity $\overline{v}$. The total deactivation probability P_k of an excited level $|k\rangle$ is the sum of radiative probability $A_k = \sum_m A_{km} = 1/\tau^\mathrm{rad}$ and the collisional deactivation probability R_k. Since the measured effective lifetime is $\tau_k^\mathrm{eff} = 1/P_k$, we obtain the equation

$$\frac{1}{\tau_k^\mathrm{eff}} = \frac{1}{\tau_k^\mathrm{rad}} + R_k\,, \quad \text{with} \quad R_k = \sum_n R_{kn}\,. \tag{6.58}$$

where the summation extends over all levels $|n\rangle$ that can be populated by collisional transitions $|k\rangle \rightarrow |n\rangle$.

In a gas cell at the temperature T the mean relative velocity between collision partners A and B with masses M_A, M_B is

$$\overline{v} = \sqrt{8kT/\pi\mu}\,, \quad \text{with} \quad \mu = \frac{M_\mathrm{A}M_\mathrm{B}}{M_\mathrm{A}+M_\mathrm{B}}\,. \tag{6.59}$$

Using the thermodynamic equation of state $p = N \cdot kT$, we can replace the density N_B in (6.57) by the pressure p and obtain the *Stern–Vollmer equation*:

$$\frac{1}{\tau_k^\mathrm{eff}} = \frac{1}{\tau_k^\mathrm{rad}} + b\sigma_k p\,, \quad \text{with} \quad b = (8/\pi\mu kT)^{1/2}\,. \tag{6.60}$$

It represents a straight line when $1/\tau^\mathrm{eff}$ is plotted versus p (Fig. 6.75). The slope $\tan\alpha = b\sigma_k$ yields the total quenching cross section σ_k and the intersect with the axis $p = 0$ gives the radiative lifetime $\tau_k^\mathrm{rad} = \tau_k^\mathrm{eff}(p = 0)$.

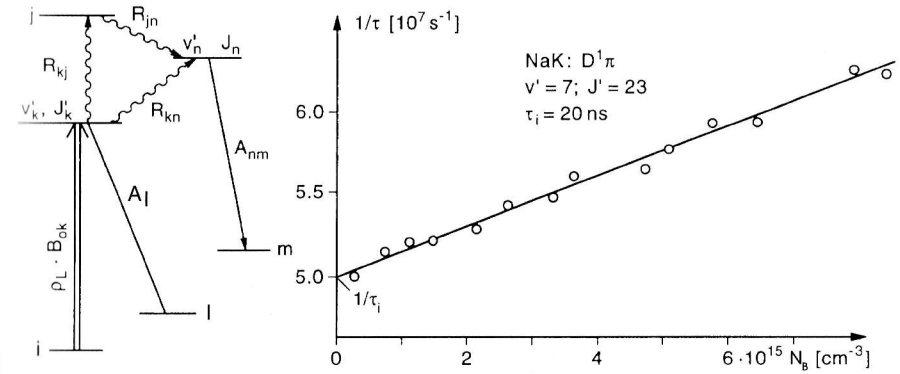

Fig. 6.75. Collisional depopulation of the excited level (v'_k, J'_k) of a molecule and example of a Stern–Vollmer plot for the NaK level $D^1\Pi_u$ $(v' = 7,\ J' = 13)$ depopulated by collisions with argon atoms at the density N_B

In the following subsections we will discuss some experimental methods of lifetime measurements [6.149, 6.150]. Nowadays lasers are generally used for the selective population of excited levels. In this case, the induced emission, which contributes to the depletion of the excited level, has to be taken into account if the exciting laser is not switched off during the fluorescence detection. The rate equation for the time-dependent population density of the level $|k\rangle$, which gives the effective lifetime τ_k^{eff}, is then

$$\frac{dN_k}{dt} = +N_i B_{ik}\rho_L - N_k(A_k + R_k + B_{ki}\rho_L) , \tag{6.61}$$

where ρ_L is the spectral energy density of the exciting laser, which is tuned to the transition $|i\rangle \rightarrow |k\rangle$. The solution $N_k(t) \propto I_{Fl}(t)$ of (6.61) depends on the time profile $I_L(t) = c\rho_L(t)$ of the excitation laser.

6.3.1 Phase-Shift Method

If the laser is tuned to the center frequency ω_{ik} of an absorbing transition $|i\rangle \rightarrow |k\rangle$, the detected fluorescence intensity I_{FL} monitored on the transition $|k\rangle \rightarrow |m\rangle$ is proportional to the laser intensity I_L as long as saturation can be neglected. In the *phase-shift method* the laser intensity is modulated at the frequency $f = \Omega/2\pi$ (Fig. 6.76a) according to

$$I_L(t) = \frac{1}{2} I_0(1 + a\sin\Omega t)\cos^2\omega_{ik}t \quad \text{with} \quad |a| \leq 1 . \tag{6.62}$$

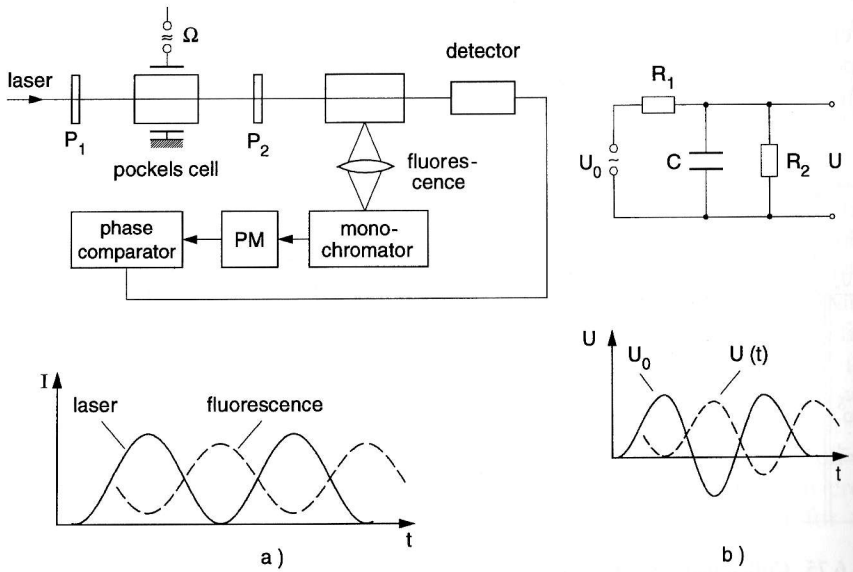

Fig. 6.76a,b. Phase-shift method for the measurement of excited-state lifetimes: (**a**) experimental arrangement; and (**b**) equivalent electric network

Inserting (6.62) with $I_L(t) = c\rho_L(t)$ into (6.61) yields the time-dependent population density $N_k(t)$ of the upper level, and therefore also the fluorescence power $P_{FL}(t) = N_k(t)A_{km}$ emitted on the transition $|k\rangle \rightarrow |m\rangle$. The result is

$$P_{FL}(t) = b\left[1 + \frac{a\sin(\Omega t + \phi)}{[1 + (\Omega\tau_{\text{eff}})^2]^{1/2}}\right]\cos^2\omega_{km}t , \tag{6.63}$$

where the constant $b \propto N_i\sigma_{ik}I_L V$ depends on the density N_i of the absorbing molecules, the absorption cross section σ_{ik}, the laser intensity I_L, and the excitation volume V seen by the fluorescence detector. Since the detector averages over the optical oscillations ω_{km} we obtain $\langle\cos^2\omega_{km}\rangle = 1/2$, and (6.63) gives similarly to (6.62) a sinewave-modulated function with a reduced amplitude and the phase shift ϕ against the exciting intensity $I_L(t)$. This phase shift depends on the modulation frequency Ω and the effective lifetime τ_{eff}. The evaluation yields

$$\tan\phi = \Omega\tau_{\text{eff}} . \tag{6.64}$$

According to (6.58–6.61) the effective lifetime is determined by the inverse sum of all deactivation processes of the excited level $|k\rangle$. In order to obtain the spontaneous lifetime $\tau_{\text{spont}} = 1/A_k$ one has to measure $\tau_{\text{eff}}(p, I_L)$ at different pressures p and different laser intensities I_L, and extrapolate the results towards $p \rightarrow 0$ and $I_L \rightarrow 0$. The influence of induced emission is a definite drawback of the phase-shift method. It can be eliminated if ϕ is measured at different intensities I_L with the extrapolation $\phi(I_L \rightarrow 0)$.

Note: This problem of exciting atoms with sine wave-modulated light and determining the mean lifetime of their exponential decay from measurements of the phase shift ϕ is mathematically completely equivalent to the well-known problem of charging a capacitor C from an ac source with the voltage $U_0(t) = U_1\sin\Omega t$ through the resistor R_1 with simultaneous discharging through a resistor R_2 (Fig. 6.76b). The equation corresponding to (6.61) is here

$$C\frac{dU}{dt} = \frac{U_0 - U}{R_1} - \frac{U}{R_2} , \tag{6.65}$$

which has the solution

$$U = U_2\sin(\Omega t - \phi) , \quad \text{with} \quad \tan\phi = \Omega\frac{R_1R_2C}{R_1 + R_2} , \tag{6.66}$$

where

$$U_2 = U_0\frac{R_2}{[(R_1 + R_2)^2 + (\Omega C R_1 R_2)^2]^{1/2}} .$$

A comparison with (6.63) shows that the mean lifetime τ corresponds to the time constant $\tau = RC$ with $R = R_1R_2/(R_1 + R_2)$ and the laser intensity to the charging current $I(t) = (U_0 - U)/R_1$.

Equation (6.64) anticipates a pure exponential decay. This is justified if a single upper level $|k\rangle$ is selectively populated. If several levels are simultaneously excited the fluorescence power $P_{FL}(t)$ represents a superposition of decay functions with different decay times τ_k. In such cases the phase shifts $\phi(\Omega)$ and the amplitudes $a/(1+\Omega^2\tau^2)^{1/2}$ have to be measured for different modulation frequencies Ω. The mathematical analysis of the results allows one to separate the contributions of the simultaneously excited levels to the decay curve and to determine the different lifetimes of these levels [6.151]. A better solution is, however, if the fluorescence is dispersed by a monochromator and the detector selectively monitors a single transition from each of the different excited levels $|k_n\rangle$ separately.

6.3.2 Single-Pulse Excitation

The molecules are excited by a short laser pulse. The trailing edge of this pulse should be short compared with the decay time of the excited level, which is directly monitored after the end of the excitation pulse (Fig. 6.77). Either the time-resolved LIF on transitions $|k\rangle \rightarrow |m\rangle$ to lower levels $|m\rangle$ is detected or the time-dependent absorption of a second laser, which is tuned to the transition $|k\rangle \rightarrow |j\rangle$, to higher levels $|j\rangle$.

The time-dependent fluorescence can be viewed either with an oscilloscope or may be recorded by a transient recorder. Another method is based on a boxcar integrator, which transmits the signal through a gate that opens only during a selected time interval Δt (Sect. 4.5.6). After each successive excitation pulse the delay ΔT of the gate is increased by T/m. After m excitation cycles the whole time window T has been covered (Fig. 6.78). The direct observation of the decay curve on an oscilloscope has the advantage that nonexponential decays can be recognized immediately. For sufficiently intense fluorescence one needs only a single excitation pulse, although generally averaging over many excitation cycles will improve the signal-to noise ratio.

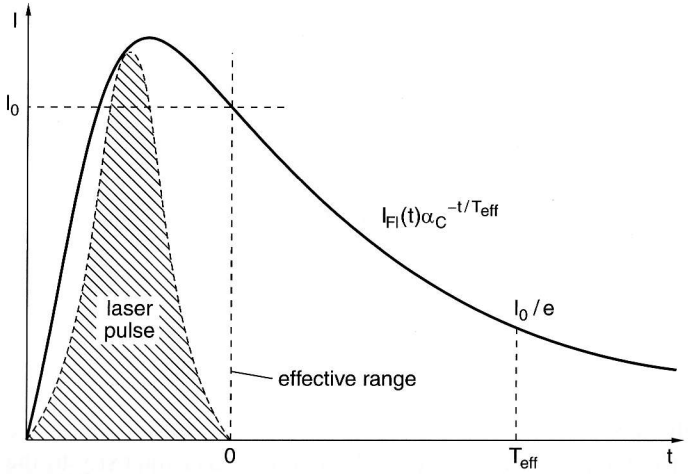

Fig. 6.77. Lifetime measurement after pulse excitation

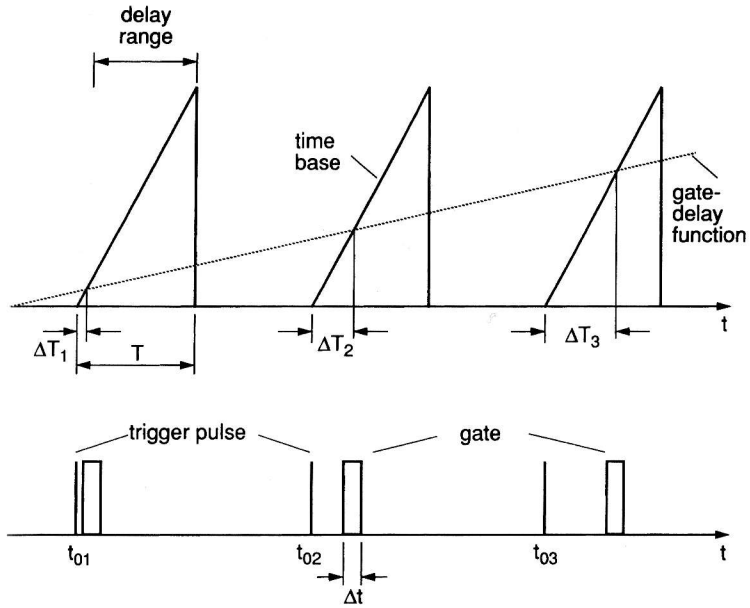

Fig. 6.78. Lifetime measurements with a gated boxcar system with successively increasing gate delay time

This technique of single-pulse excitation is useful for low repetition rates. Examples are the excitation with pulsed dye lasers pumped by Nd:YAG or excimer lasers [6.149, 6.152].

6.3.3 Delayed-Coincidence Technique

As in the previous method the delayed-coincidence technique also uses short laser pulses for the excitation of selected levels. However, here the pulse energy is kept so low that the detection probability P_D of a fluorescence photon per laser excitation pulse remains small ($P_D \leq 0.1$). If $P_D(t)\,dt$ is the probability of detecting a fluorescence photon in the time interval t to $t+dt$ after the excitation then the mean number $n_{Fl}(t)$ of fluorescence photons detected within this time interval for N excitation cycles ($N \gg 1$) is

$$n_{Fl}(t)\,dt = NP_D(t)\,dt\,. \tag{6.67}$$

The experimental realization is shown schematically in Fig. 6.79. Part of the laser pulse is send to a fast photodiode. The output pulse of this diode at $t = t_0$ starts a time-amplitude converter (TAC), which generates a fast-rising voltage ramp $U(t) = (t - t_0)U_0$. A photomultiplier with a large amplification

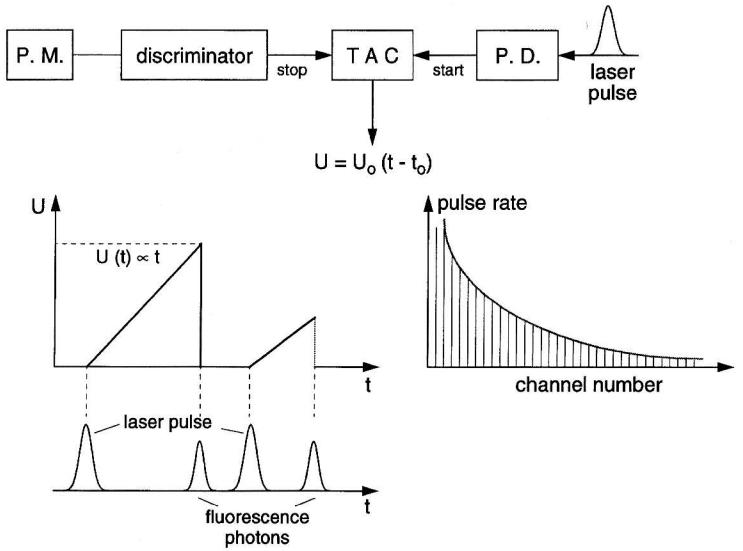

Fig. 6.79. Basic principle of lifetime measurements with the delayed-coincidence single-photon counting technique

factor generates for each detected fluorescence photon an output pulse that triggers a fast discriminator. The normalized output pulse of the discriminator stops the TAC at time t. The amplitude $U(t)$ of the TAC output pulse is proportional to the delay time $t - t_0$ between the excitation pulse and the fluorescence photon emission. These pulses are stored in a multichannel analyzer. The number of events per channel gives the number of fluorescence photons emitted at the corresponding delay time.

The repetition rate f of the excitation pulses is chosen as high as possible since the measuring time for a given signal-to-noise-ratio is proportional to $1/f$. An upper limit for f is determined by the fact that the time $T = 1/f$ between two successive laser pulses should be at least three times the lifetime τ_k of the measured level $|k\rangle$. This technique is therefore ideally suited for excitation with mode-locked or cavity-dumped lasers. There is, however, an electronic bottleneck: the input pulse rate of a TAC is limited by its dead time τ_D and should be smaller than $1/\tau_D$. It is therefore advantageous to invert the functions of the start and stop pulses. The fluorescence pulses (which have a much smaller rate than the excitation pulses) now act as start pulses and the next laser pulse stops the TAC. This means that the time $(T - t)$ is measured instead of t. Since the time T between successive pulses of a mode-locked laser is very stable and can be accurately determined from the mode-locking frequency $f = 1/T$, the time interval between successive pulses can be used for time calibration of the detection system [6.32]. In Fig. 6.80 the whole detection system is shown together with a decay curve of an excited level of the Na_2 molecule, measured over a period of 10 min. More information about the delayed-coincidence method can be found in [6.153].

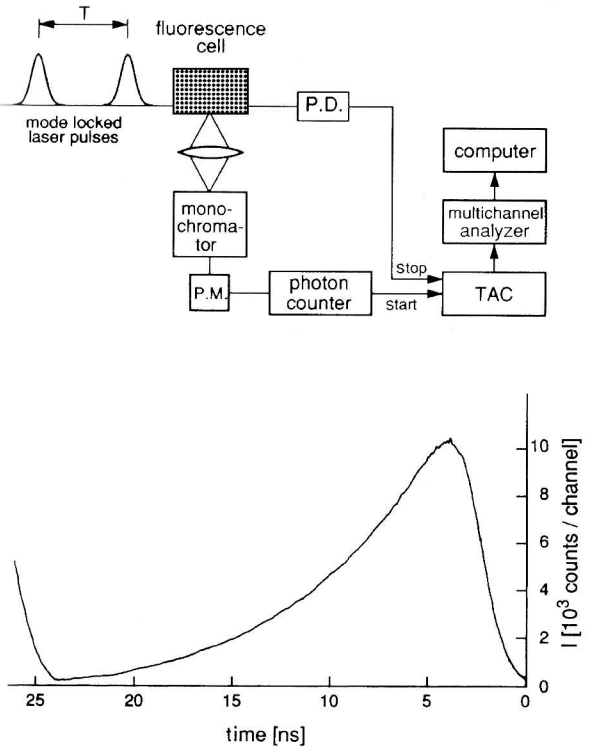

Fig. 6.80. Experimental arrangement for lifetime measurements with the delayed-coincidence single-photon counting technique and decay curve of the Na_2 ($B^1\Pi_u$ $v' = 6$, $J' = 27$) level [6.32]

6.3.4 Lifetime Measurements in Fast Beams

The most accurate method for lifetime measurements in the range of 10^{-7}–10^{-9} s is based on a modern version of an old technique that was used by W. Wien 70 years ago [6.154]. Here a time measurement is reduced to measurements of a pathlength and a velocity.

The atomic or molecular ions produced in an ion source are accelerated by the voltage U and focused to form an ion beam. The different masses are separated by a magnet (Fig. 6.81) and the wanted ions are excited at the position $x = 0$ by a cw laser beam. The LIF is monitored as a function of the variable distance x between the excitation region and the position of a special photon detector mounted on a precision translational drive. Since the velocity $v = (2eU/m)^{1/2}$ is known from the measured acceleration voltage U, the time $t = x/v$ is determined from the measured positions x.

The excitation intensity can be increased if the excitation region is placed inside the resonator of a cw dye laser that is tuned to the selected transition. Before they reach the laser beam, the ions can be preexcited into highly excited long-living levels by gas collisions in a differentially pumped gas cell

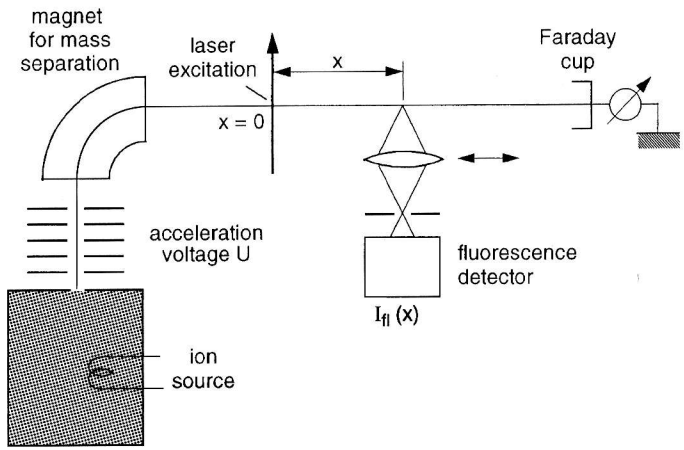

Fig. 6.81. Lifetime measurements of highly excited levels of ions or neutral atoms and molecules in a fast beam

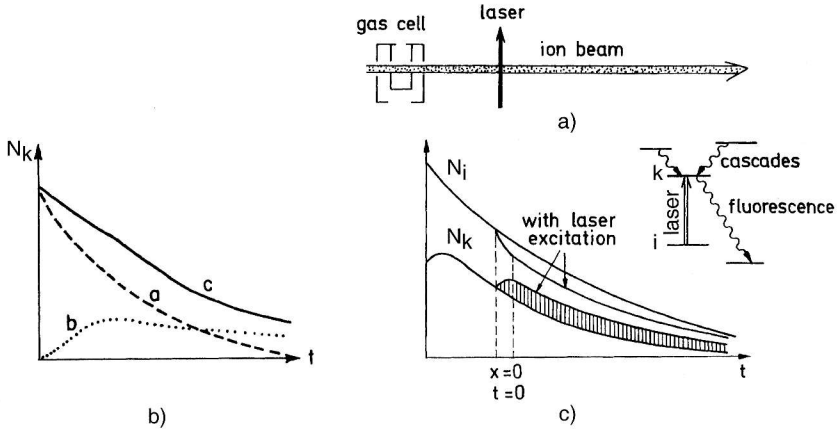

Fig. 6.82a–c. Cascade-free lifetime measurements despite the simultaneous excitation of many levels: (**a**) preexcitation by collisions in a gas cell with subsequent laser excitation; (**b**) decay of level $|k\rangle$ without cascading (*curve a*), its feeding by cascades (*curve b*), and resulting population $N_k(t)$ with cascading and decaying (*curve c*). (**c**) The fluorescence $I(x, \lambda)$ is measured alternately with and without selective laser excitation

(Fig. 6.82a). This opens new transitions for the laser excitation and allows lifetime measurements of high-lying ionic states even with visible lasers [6.155].

The ions can be neutralized by charge-exchange collisions in differentially pumped alkali-vapor cells. Since charge exchange occurs with large collision cross sections at large impact parameters (grazing collisions), the momentum transfer is very small and the velocity of the neutrals is nearly the same as that of the ions. With this technique lifetimes of highly excited neutral atoms or molecules can be measured with high accuracy.

Collisional preexcitation has the drawback that several levels are simultaneously excited, which may feed by cascading fluorescence transitions the level $|k\rangle$ whose lifetime is to be measured. These cascades alter the time profile $I_{FL}(t)$ of the level $|k\rangle$ and falsify the real lifetime τ_k (Fig. 6.82b). This problem can be solved by a special measurement cycle: for each position x the fluorescence is measured alternately with and without laser excitation (Fig. 6.82c). The difference of both counting rates yields the LIF without cascade contributions. In order to eliminate fluctuations of the laser intensity or the ion beam intensity a second detector is installed at the fixed position x_0 (Fig. 6.83). The normalized ratios $S(x)/S(x_0)$, which are independent of these fluctuations, are then fed into a computer that fits them to a theoretical decay curve [6.156].

The time resolution Δt of the detectors is determined by their spatial resolution Δx and the velocity v of the ions or neutrals. In order to reach a good time resolution, which is *independent* of the position x of the detector, one has to take care that the detector collects the fluorescence only from a small path interval Δx, but still sees the whole cross section of the slightly divergent ion beam. This can be realized by specially designed bundles of optical fibers, which are arranged in a conical circle around the beam axis (Fig. 6.83), while the outcoupling end of the fiber bundle has a rectangular form which is matched to the entrance slit of a spectrograph.

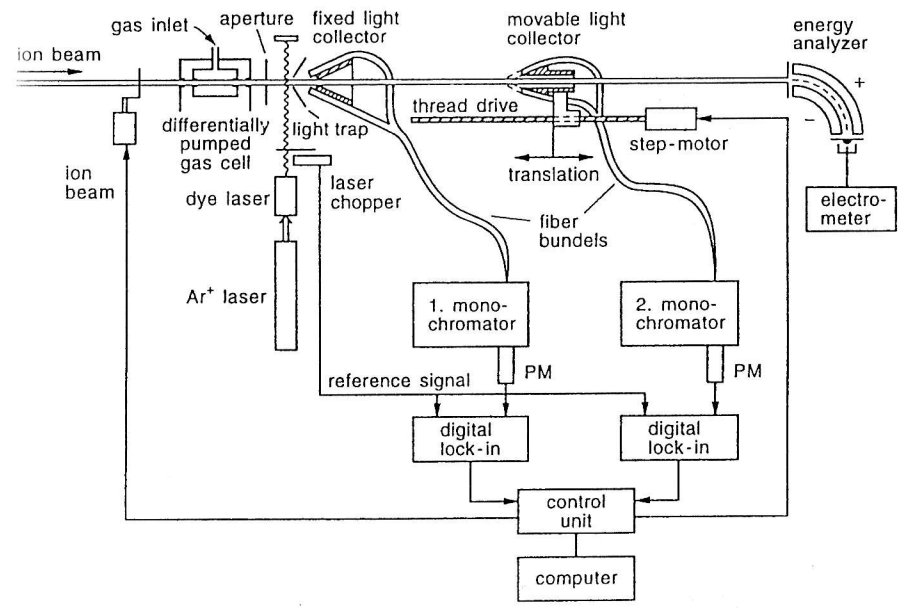

Fig. 6.83. Experimental arrangement for cascade-free lifetime measurements in fast beams of ions or neutrals with fluorescence collection by conically shaped optical-fiber bundles

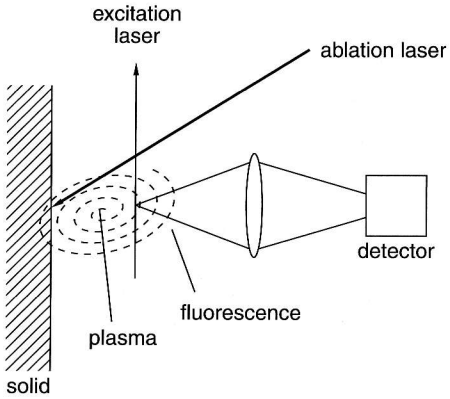

Fig. 6.84. Laser ablation from surfaces and laser excitation of the plasma plume with fluorescence detection

Lifetimes of atoms and ions have been measured very accurately with this technique. More experimental details and different versions of this laser beam method can be found in the extensive literature [6.155–6.159].

Example 6.5.

Ne ions (23 atomic mass units, AMU) accelerated by $U = 150\,\mathrm{kV}$ have a velocity $v = 10^6\,\mathrm{m/s}$. In order to reach a time resolution of 1 ns the spatial resolution of the detector must be $\Delta x = 1\,\mathrm{mm}$.

High-lying excited states of atoms and ions, which are of interest in astrophysics, can be produced by laser ablation from surfaces. The expanding plasma cloud, which consists of hot atoms and ions, is irradiated by a second laser, and the time-resolved fluorescence of the excited states is monitored. Since many of these states can only be reached by VUV lasers, the excitation must be performed in a vacuum chamber and VUV-sensitive detectors (for instance solar blind multipliers) must be used [6.160]. A typical experimental setup is shown in Fig. 6.84. The excitation laser can be time-delayed with respect to the ablation laser by a electronic delay unit which allows delay times of $\Delta\tau > 1\,\mathrm{ns}$.

6.4 Spectroscopy in the Pico-to-Attosecond Range

For measurements of very fast relaxation processes that demand a time resolution below $10^{-10}\,\mathrm{s}$ most detectors (except the streak camera) are not fast enough. Here the pump-and-probe technique is the best choice. It is based on the following principle shown in Fig. 6.85.

The molecules under investigation are excited by a fast laser pulse on the transition $|0\rangle \rightarrow |1\rangle$. A probe pulse with a variable time delay τ against the pump pulse probes the time evolution of the population density $N_1(t)$. The time resolution is only limited by the pulse width ΔT of the two pulses, but not by the time constants of the detectors!

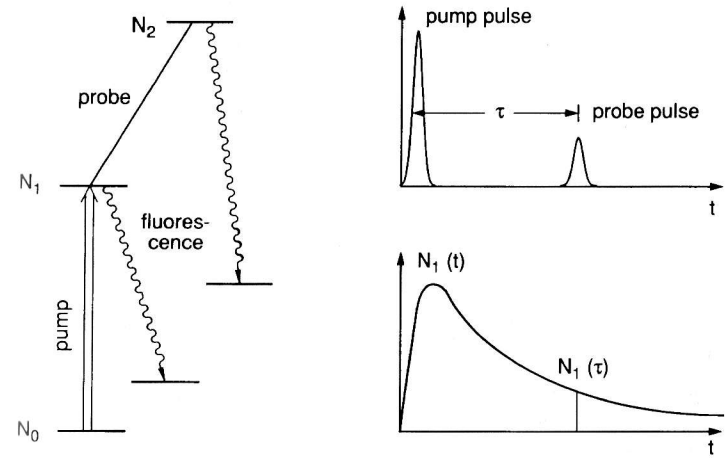

Fig. 6.85. Pump-and-probe technique

In early experiments of this kind a fixed-frequency mode-locked Nd:glass or Nd:YAG laser was used. Both pulses came from the same laser and fortuitious coincidences of molecular transitions with the laser wavelength were utilized [6.161]. The time delay of the probe pulse is realized, as shown in Fig. 6.86, by beam splitting and a variable path-length difference. Since the pump and probe pulses coincide with the same transition $|i\rangle \rightarrow |k\rangle$, the absorption of the probe pulse measured as a function of the delay time τ, in fact, monitors the time evolution of the population difference $[N_k(t) - N_i(t)]$. A larger variety of molecular transitions becomes accessible if the Nd:YAG laser wavelength is Raman shifted (Sect. 5.9) into spectral regions of interest [6.162].

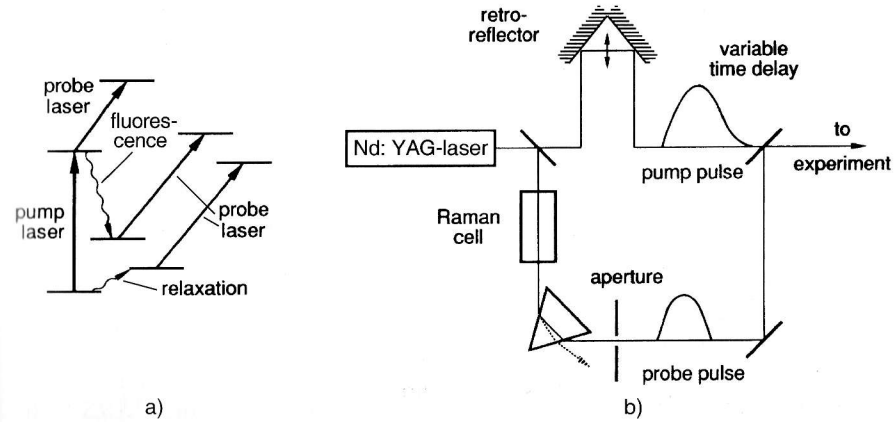

Fig. 6.86. Pump-and-probe technique for the measurements of ultrafast relaxation processes

A broader application range is opened by a system of two independently tunable mode-locked dye lasers, which have to be pumped by the same pump laser in order to synchronize the pump and probe pulses [6.163]. For studies of vibrational levels in the electronic ground states of molecules the difference frequency generation of these two dye lasers can be used as a tunable infrared source for direct excitation of selected levels on infrared-active transitions. Raman-active vibrations can be excited by spontaneous or stimulated Raman transitions (Chap. 3). Another useful short-pulse source for these experiments is a three-wavelength Ti:sapphire laser, where two of the wavelengths can be indepently tuned [6.166].

In addition, short-pulse tunable optical parametric oscillators have been realized, where the pump wavelength and the signal or idler waves can be used for pump-and-probe experiments [6.164]. The wide tuning range allows more detailled investigations compared to the restricted use of fixed frequency lasers [6.165]. Here the different femtosecond NOPAs (see Sect. 6.1.9) in combination with frequency doubling or sum-frequency generation provide the spectroscopist with widely tunable ultrafast intense radiation sources which can be tuned across the infrared and visible to the UV region. These open the door to studies of fast dynamical processes in chemistry and biology (see Sect. 10.3).

Recently it has become possible to phase-lock two different femtosecond lasers. This opens many possibilities for spectroscopic applications. One example is the use of an infrared femtosecond pulse to excite nuclear vibrations of molecules and a second UV femtosecond pulse for electronic excitation. This allows one to study the influence of fast changes of the electron cloud on the nuclear oscillation period [6.167].

These developments widen the range of applications considerably. We will now give some examples of applications of the pump-and-probe technique.

6.4.1 Pump-and-Probe Spectroscopy of Collisional Relaxation in Liquids

Because of the high molecular density in liquids, the average time τ_c between two successive collisions of a selectively excited molecule A with other molecules A of the same kind or with different molecules B is very short (10^{-12}–10^{-11} s). If A has been excited by absorption of a laser photon its excitation energy may be rapidly redistributed among other levels of A by collisions, or it may be transferred into internal energy of B or into translational energy of A and B (temperature rise of the sample). With the pump-and-probe technique this energy transfer can be studied by measurements of the time-dependent population densities $N_m(t)$ of the relevant levels of A or B. The collisions not only change the population densities but also the phases of the wave functions of the coherently excited levels (Sect. 2.9). These phase relaxation times are generally shorter than the population relaxation times.

Besides excitation and probing with infrared laser pulses, the CARS technique (Sect. 3.5) is a promising technique to study these relaxation processes. An example is the measurement of the dephasing process of the OD stretching vibration in heavy water D_2O by CARS [6.168]. The pump at $\omega = \omega_L$ is provided by an amplified 80-fs dye laser pulse from a CPM ring dye laser. The Stokes pulse at ω_s is generated by a synchronized tunable picosecond dye laser. The CARS signal at $\omega_{as} = 2\omega_L - \omega_s$ is detected as a function of the time delay between the pump and probe pulses.

Another example is the deactivation of high vibrational levels in the S_0 and S_1 singlet states of dye molecules in organic liquids pumped by a pulsed laser (Fig. 6.87). The laser populates many vibrational levels in the excited S_1 singlet state, which are accessible by optical pumping on transitions starting from thermally populated levels in the electronic ground state S_0. These excited levels $|v'\rangle$ rapidly relax by inelastic collisions into the lowest vibrational level $|v' = 0\rangle$ of S_1, which represents the upper level of the dye laser transition. This relaxation process can be followed up by measuring the time-dependent absorption of a weak probe laser pulse on transitions from these levels into higher excited singlet states.

Fluorescence and stimulated emission on transitions ($v' = 0 \rightarrow v'' > 0$) lead to a fast rise of the population densities $N(v'')$ of high vibrational levels in the S_0 state. This would result in a self-termination of the laser oscillation if these levels were not depopulated quickly enough by collisions. The relaxation of $N(v'')$ toward the thermal equilibrium population $N_0(v'')$ can again be probed by a weak visible probe laser. Polarization spectroscopy (Sect. 2.4) with femtosecond pulses allows one to separately determine the decay times τ_{vib} of population redistribution and the dephasing times [6.169].

Of particular importance for dye laser physics is the intersystem crossing of dye molecules from the excited S_1 state into levels of the triplet state T_1. Because the population of these long-living triplet levels represents a severe loss for the dye laser radiation because of absorption on electronic transitions to higher triplet states, the time-dependent triplet concentration and possible quenching processes by triplet-quenching additives have been investigated in detail [6.170]. Furthermore, spin-exchange and transitions by collisions between excited S_1 dye molecules and triplet O_2 molecules or between T_1 dye molecules and excited O_2 ($^1\Delta$) molecules play a crucial role in photodynamical processes in cancer cells (Sect. 10.5).

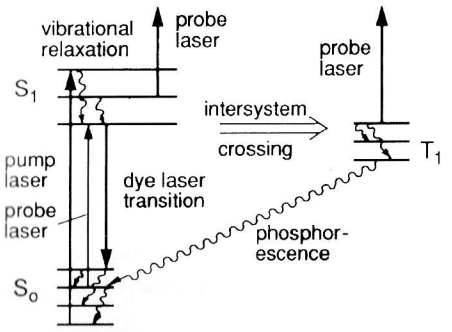

Fig. 6.87. Measurements of fast relaxation processes in excited and ground states

6.4.2 Electronic Relaxation in Semiconductors

A very interesting problem is concerned with the physical limitations of the ultimate speed of electronic computers. Since any *bit* corresponds to a transition from a nonconducting to a conducting state of a semiconductor, or vice versa, the relaxation time of electrons in the conduction band and the recombination time certainly impose a lower limit for the minimum switching time. This electronic relaxation can be measured with the pump-and-probe technique. The electrons are excited by a femtosecond laser pulse from the upper edge of the valence band into levels with energies $E = \hbar\omega - \Delta E$ (ΔE: band gap) in the conduction band, from where they relax into the lower edge of the conduction band before they recombine with holes in the valence band. Since the optical reflectivity of the semiconductor sample depends on the energy distribution $N(E)$ of the free conduction electrons, the reflection of a weak probe laser pulse can be used to monitor the distribution $N(E)$ [6.171]. Because of their fast relaxaton semiconductors can be used as saturable absorbers for passive mode locking in femtosecond lasers [6.67]. In this case, a thin semiconductor sheet is placed in front of a resonator mirror (see Sect. 6.1.11. The characteristic time scales for interband and intraband electron relaxation are again measured with the pump-and probe technique [6.172]. Of particular interest for the magnetic storage of information is the timescale of magnetization or demagnetization of thin magnetic films. It turns out that femtosecond laser pulses focused onto the film can demagnetize a small local area within about 100 fs [6.173].

6.4.3 Femtosecond Transition State Dynamics

The pump-and-probe technique has proved to be very well suited for studying short-lived transient states of molecular systems that had been excited by a short laser pulse before they dissociate:

$$AB + h\nu \longrightarrow [AB]^* \longrightarrow A^* + B\,.$$

An illustrative example is the photodissociation of excited NaI molecules, which has been studied in detail by Zewail et al. [6.174].

The adiabatic potential diagram of NaI (Fig. 6.88) is characterized by an avoided crossing between the repulsive potential of the two interacting neutral atoms Na + I and the Coulomb potential of the ions $Na^+ + I^-$, which is mainly responsible for the strong binding of NaI at small internuclear distances R. If NaI is excited into the repulsive state by a short laser pulse at the wavelength λ_1, the excited molecules start to move toward larger values of R with a velocity $v(R) = [(2/\mu)(E - E_{pot}(R)]^{1/2}$.

Example 6.6.

For $E - E_{pot} = 1000\,cm^{-1}$ and $\mu = m_1 m_2/(m_1 + m_2) = 19.5$ AMU $\rightarrow v \approx 10^3$ m/s. The time $\Delta T = \Delta R/v$ of passing through an interval of $\Delta R = 0.1$ nm is then $\Delta T = 10^{-13}$ s $= 100$ fs.

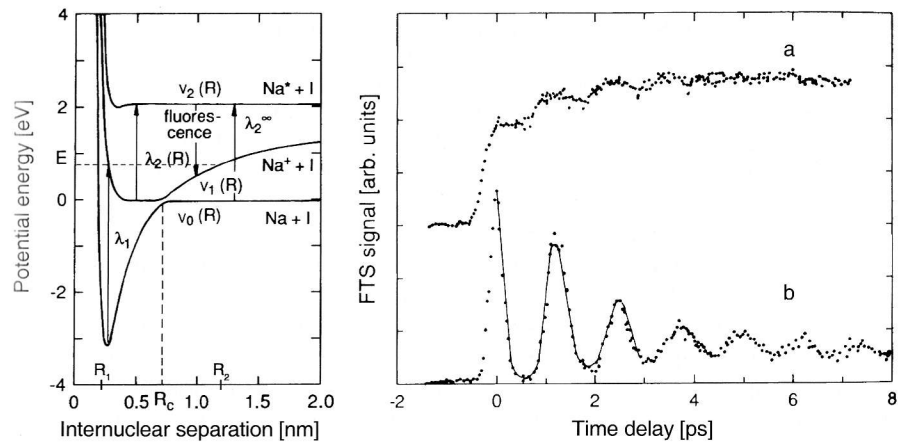

Fig. 6.88. (**a**) Potential diagram of NaI with the pump transition at λ_1 and the tunable probe pulse at $\lambda_2(R)$. (**b**) Fluorescence intensity $I_{Fl}(\Delta t)$ as a function of the delay time Δt between pump and probe pulses: (*curve a*) with λ_2 tuned to the atomic Na* transition and (*curve b*) λ_2 tuned to $\lambda_2(R)$ with $R < R_c$ [6.174]

When the excited system [NaI]* reaches the avoided crossing at $R = R_c$ it may either stay on the potential $V_1(R)$ and oscillate back and forth between R_1 and R_2, or it may tunnel to the potential curve $V_0(R)$, where it separates into Na + I.

The time behavior of the system can be probed by a probe pulse with the wavelength λ_2 tuned to the transition from $V_1(R)$ into the excited state $V_2(R)$ that dissociates into Na* + I. At the fixed wavelength $\lambda_2 = 2\pi c/\omega_2$ the dissociating system absorbs the probe pulse only at that distance R where $V_1(R) - V_2(R) = \hbar\omega_2$. If λ_2 is tuned to the sodium resonance line $3s \rightarrow 3p$, absorption occurs for $R = \infty$.

Since the dissociation time is very short compared to the lifetime of the excited sodium atom Na*($3p$), the dissociating (NaI)* emits nearly exclusively at the atomic resonance fluorescence. The atomic fluorescence intensity $I_{Fl}(Na^*, \Delta t)$, monitored in dependence on the delay time Δt between the pump-and-probe pulse, gives the probability for finding the excited system [NaI]* at a certain internuclear separation R, where $V_1(R) - V_2(R) = \hbar\omega_2$ (Fig. 6.88b).

The experimental results [6.175] shown in Fig. 6.88b reflect the oscillatory movement of Na*I(R) on the potential $V_1(R)$ between R_1 and R_2, which had been excited at the inner turning point R_1 by the pump pulse at $t = 0$. This corresponds to a periodic change between the covalent and ionic potential. The damping is due to the leakage into the lower-state potential around the avoided crossing at $R = R_c$. If λ_2 is tuned to the atomic resonance line, the accumulation of Na*($3p$) atoms can be measured when the delay between the pump-and-probe pulse is increased.

6.4.4 Real-Time Observations of Molecular Vibrations

The time scale of molecular vibrations is on the order of 10^{-13}–10^{-15} s. The vibrational frequency of the H_2 molecule, for example, is $\nu_{vib} = 1.3 \times 10^{14}\,s^{-1} \rightarrow T_{vib} = 7.6 \times 10^{-15}$ s, that of the Na_2 molecule is $\nu_{vib} = 4.5 \times 10^{12}\,s^{-1} \rightarrow T_{vib} = 2 \times 10^{-13}$ s, and even the heavy I_2 molecule still has $T_{vib} = 5 \times 10^{-13}$ s. With conventional techniques one always measures a time average over many vibrational periods.

With femtosecond pump-and-probe experiments "fast motion pictures" of a vibrating molecule may be obtained, and the time behavior of the wave packets of coherently excited and superimposed molecular vibrations can be mapped. This is illustrated by the following examples dealing with the dynamics of molecular multiphoton ionization and fragmentation of Na_2, and its dependence on the phase of the vibrational wave packet in the inter-

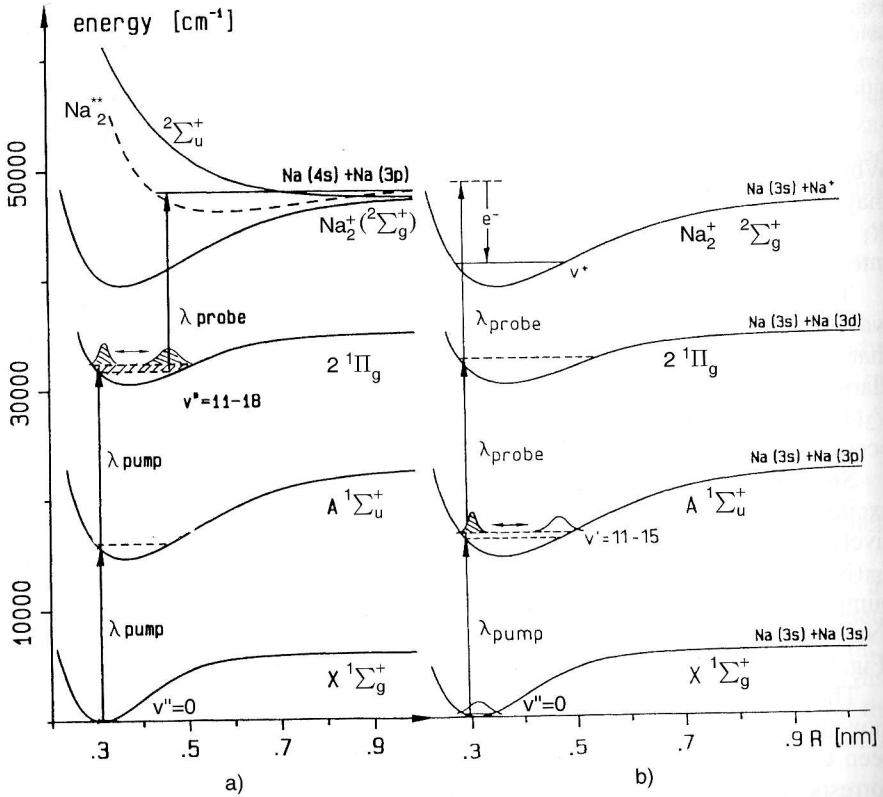

Fig. 6.89a,b. Femtosecond spectroscopy of Na_2: (**a**) potential curve diagram illustrating the preparation of a vibrational wave packet in the $2^1\Pi_g$ state of Na_2 due to coherent simultaneous two-photon excitation of vibrational levels ($v' = 11$–18). Further excitation by a third photon results in production of $Na_2^{**} \rightarrow Na^+ + Na^*$ from the outer turning point of the wave packet. (**b**) One-photon excitation of a vibrational wave packet in the $A^1\Sigma_u$ state with subsequent two-photon ionization from the *inner* turning point [6.177]

mediate state [6.176]. There are two pathways for photoionization of cold Na_2 molecules in a supersonic beam (Fig. 6.89):

(i) One-photon absorption of a femtosecond pulse ($\lambda = 672$ nm, $\Delta T = 50$ fs, $I = 50\,GW/cm^2$) leads to simultaneous coherent excitation of vibrational levels $v' = 11$–15 in the $A^1\Sigma_u$ state of Na_2 at the inner part of the potential $V_1(R)$. This generates a vibrational wave packet, which oscillates at a frequency of $3 \times 10^{12}\,s^{-1}$ back and forth between the inner and outer turning point. Resonant enhanced two-photon ionization of the excited molecules by the probe pulse has a larger probability at the inner turning point than at the outer turning point, because of favorable Franck–Condon factors for transitions from the $A^1\Sigma_u$ state to the near-resonant intermediate state $2^1\Pi_g$, which enhances ionizing two-photon transitions at small values of the internuclear distance R (Fig. 6.89b). The ionization rate $N(Na_2^+, \Delta t)$ monitored as a function of the delay time Δt between the weak pump pulse and the stronger probe pulse, yields the upper oscillatory function of Fig. 6.90 with a period that matches the vibrational wave-packet period in the $A^1\Sigma_u$ state.

(ii) The second possible competing process is the two-photon excitation of wavepackets of the $v' = 11$–18 vibrational levels in the $2^1\Pi_g$ state of Na_2 by the pump pulse, with subsequent one-photon excitation into a doubly excited state of Na_2^{**}, which autoionizes according to

$$Na_2^{**} \longrightarrow Na_2^+ + e^- \longrightarrow Na^+ + Na^* + e^- ,$$

and results in the generation of Na^+ ions. The number $N(Na^+, \Delta t)$ of atomic ions Na^+, measured as a function of the delay time Δt between pump and probe pulses, shows again an oscillatory structure (Fig. 6.90, lower trace), but with a time shift of half a vibrational period against the upper trace. In this case, the ionization starts from the *outer* turning point of the $2^1\Pi_g$ levels and

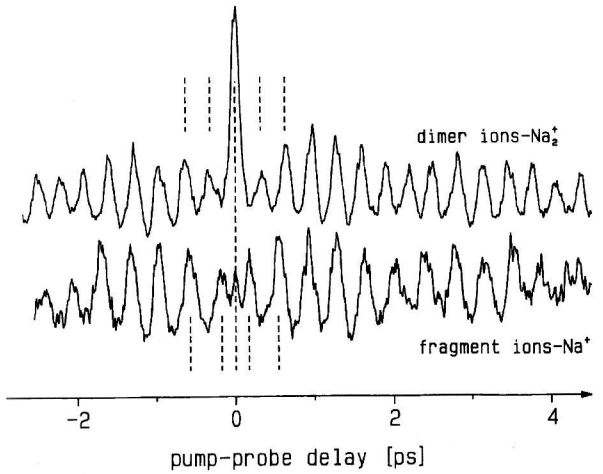

Fig. 6.90. Observed ion rates $N(Na_2^+)$ (*upper trace*) and $N(Na^+)$ (*lower trace*) as a function of the delay time Δt between the pump and probe pulses [6.177]

the oscillatory structure shows a 180° shift and slightly different oscillation period, which corresponds to the vibrational period in the $2^1\Pi_g$ state.

The photoelectrons and ions and their kinetic energies can be measured with two time-of-flight mass spectrometers arranged into opposite directions perpendicular to the molecular and the laser beams [6.178, 6.179].

6.4.5 Attosecond Spectroscopy of Atomic Inner Shell Processes

For inner-shell spectroscopy, where the energy separation of atomic states ranges from several hundred eV up to keV, the higher harmonics generated by high-intensity femtosecond pulses can be used [6.180]. Unfortunately these high harmonic pulses with pulse widths in the attosecond range appear as pulse trains with a repetition frequency twice that of the optical frequency of the generating pulse, i.e., a time separation of about 2.3 fs. The interpretation of results from time-resolved spectroscopy obtained through atomic excitation by such pulse trains is not unambiguous. Therefore, it is desirable to generate single pulses instead of pulse trains. This is possible if a pulse of less than 5 fs is used for the generation of higher harmonics. Using phase control of such a pulse, one maximum of the field amplitude $E(t)$ can be shifted into the maximum of the pulse envelope. The initial and the following maximum then have a lower amplitude (Fig. 6.91). Since the intensity of the n-th harmonic scales with the $2n$-th power $E^{2n}(t)$ of the optical electric field in the

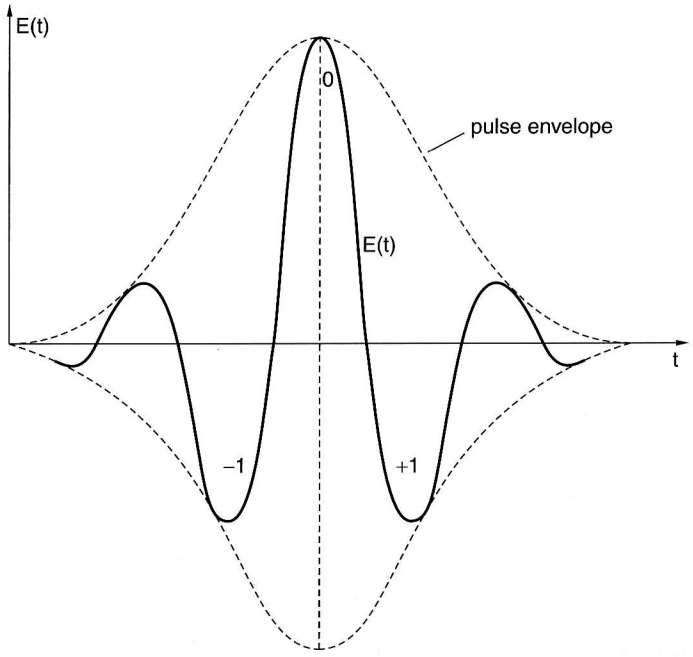

Fig. 6.91. Electric field amplitude in a few-cycle femtosecond pulse

femtosecond pulse, only this largest field maximum E_0 essentially contributes to the generation of higher harmonics. With $n = 15$, for example, the generation of XUV by the adjacent field extrema E_{-1} and E_{+1} in Fig. 6.91, which reach only 60% of the central maximum, has a probability of 10^{-7} compared to that for the central maximum.

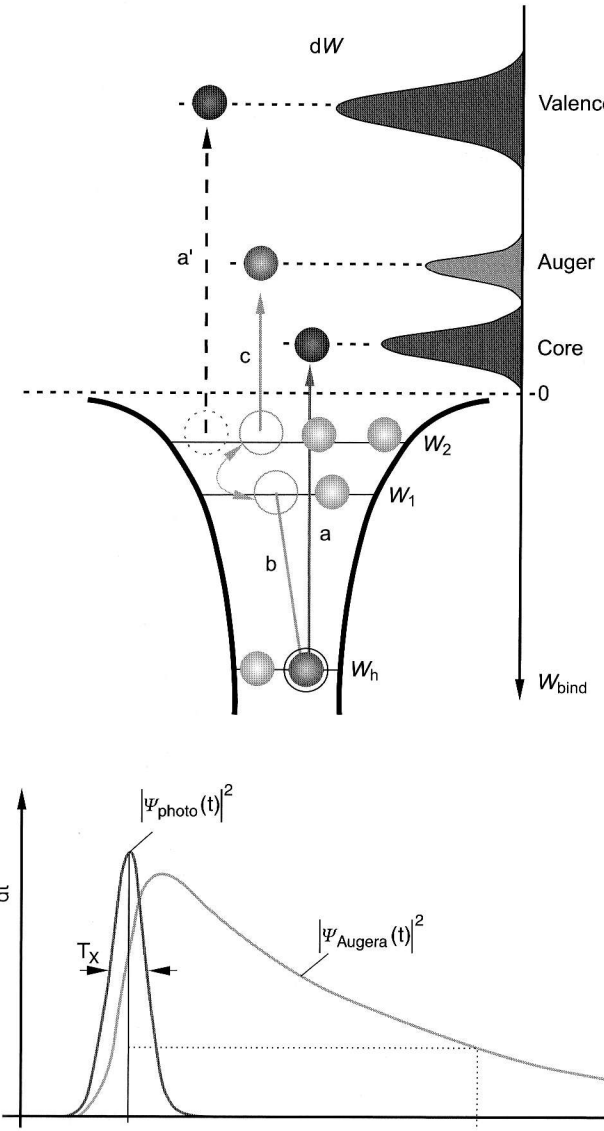

Fig. 6.92. Schematic illustration of inner shell excitation by a VUV pulse (a) and relaxation (b) into the vacancy, resulting in the emission of an Auger electron (c) or the excitation into a higher state (a′) [6.181]

Using such short attosecond XUV pulses, the temporal evolution of the Auger process after inner shell excitation can be followed with the pump-and-probe technique.

An XUV pulse excites an electron from the inner shell E_i of an atom (Fig. 6.92), producing an inner shell vacancy which is rapidly filled by an electron from a higher shell with energy E_k. The energy difference $\Delta E = E_k - E_i$ is either carried away by an XUV photon or it is transferred to another electron in an outer shell E_m with $\mathrm{IP} - E_m < \Delta E$ (Auger electron). The delay time of this Auger electron with respect to the excitation pulse corresponds exactly to the lifetime of the inner shell vacancy. The emitted Auger electron leaves a vacancy in the outer shell which can be detected by the corresponding decrease in the photoionization with visible light. The delay time can be measured with attosecond time resolution by using a fraction of the visible femtosecond pulse with variable delay with respect to the excitation pulse, in the same approach as used for photoionization with femtosecond pulses, as discussed in Sect. 6.1.12 [6.181].

6.4.6 Transient Grating Techniques

If two light pulses of different propagation directions overlap in an absorbing sample, they produce an interference pattern because of the intensity-dependent saturation of the population density (Fig. 6.93). When a probe pulse is sent through the overlap region in the sample, this interference pattern shows up as periodic change of the sample transmission and therefore acts as a grating that produces diffraction orders of the probe beam. The grating vector is $k_G = k_2 - k_1$, and the grating period depends on the angle Θ between the two pump beams. The grating amplitude can be inferred from the relative intensity of the different diffraction orders. This gives information on the saturation intensities. The grating will fade away if the delay times τ_1 and τ_2 are larger than the relaxation time of the sample molecules. Therefore this technique of transient gratings gives information on the dynamics of the sample [6.182].

Most experiments have been performed in solid or liquid samples where the relaxation times are in the range of femto- to picoseconds [6.179].

There are numerous other examples where pico- and femtosecond spectroscopy have been applied to problems in atomic and molecular physics. Some of them are discussed in Sects. 7.6 and 10.2.

In particular the high peak powers now available by the invention of new techniques (Fig. 6.55) allow a new class of experiments in nonlinear physics. Examples are the generation of high harmonics up to the 60th overtone, which generates XUV frequencies with $\lambda = 13\,\mathrm{nm}$ from the fundamental wave with $\lambda = 800\,\mathrm{nm}$, or multiphoton ionization to produce highly charged ions from neutral atoms. The electric fields of such high power laser pulses exceed the inner-atomic field strength resulting in field ionization. The behavior of atoms and molecules in such strong electric ac fields have brought some surprises

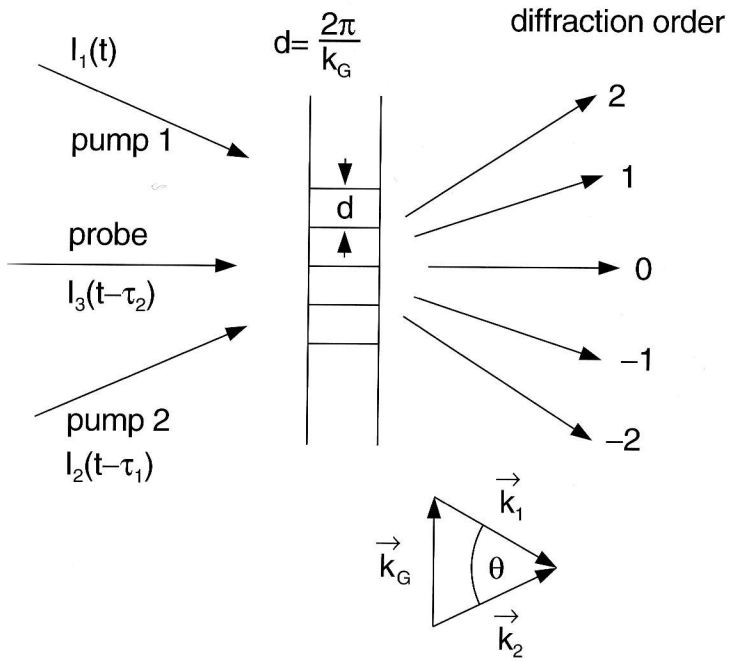

Fig. 6.93. Schematic diagram of a transient grating experiment

and many theoreticians are working on adequate models to describe such extreme situations.

For more information on femtosecond lasers and spectroscopy see [6.2, 6.183].

Problems

6.1 A Pockels cell inside a laser resonator is used as a Q-switch. It has a maximum transmission of 95% for the applied voltage $U = 0$. What voltage U is required to prevent lasing before the gain $G_\alpha = \exp(\alpha L)$ of the active medium exceeds the value $G_\alpha = 10$, when the "half-wave voltage" of the Pockels cell is 2 kV? What is the effective amplification factor G_{eff} immediately after the opening of the Pockels cell if the total cavity losses are 30° per round trip?

6.2 What is the actual time profile of mode-locked pulses from a cw argon laser if the gain profile is Gaussian with a halfwidth of 8 GHz (FWHM)?

6.3 An optical pulse with the Gaussian intensity profile $I(t)$, center wavelength $\lambda_0 = 600\,\mathrm{nm}$, and initial halfwidth $\tau = 500\,\mathrm{fs}$ propagates through an optical fiber with refractive index $n = 1.5$.

(a) How large is its initial spatial extension?
(b) How long is the propagation length z_1 after which the spatial width of the pulse has increased by a factor of 2 from linear dispersion with $dn/d\lambda = 10^3$ per cm?
(c) How large is its spectral broadening at z_1 if its peak intensity is $I_p = 10^{13}\,W/m^2$ and the nonlinear part of the refractive index is $n_2 = 10^{-20}\,m^2/W$?

6.4 Calculate the separation D of a grating pair that just compensates a spatial dispersion $dS/d\lambda = 10^5$ for a center wavelength of 600 nm, a groove spacing of $d = 1\,\mu m$ and angle of incidence $\alpha = 30°$.

6.5 Calculate the pressure p of the argon buffer gas at $T = 500\,K$ that decreases the radiative lifetime $\tau = 16\,ns$ of an excited Na_2 level to 8 ns, if the total quenching cross section is $\sigma = 10^{-14}\,cm^2$.